Critical behaviour of interacting iron-oxide-based nanoparticle systems

by

Alberto Acosta Martínez

A Thesis submitted to the Faculty of Graduate and Postdoctoral Studies
of the University of Manitoba
in partial fulfillment of the requirements of the degree of

MASTER OF SCIENCE

Department of Physics and Astronomy
University of Manitoba
Winnipeg

Abstract

The study of disordered magnetic systems is a core topic in condensed matter physics. Specifically, spin-glasses represent a real challenge for theory, because their description combines all the difficulties of the theories of magnetic phase transitions and disordered systems. The recent progress in spin-glass theory has already led to considerable advances in statistical physics, and methods developed initially to study spin-glasses have facilitated research in other fields, for example polymer chemistry, protein folding, optimization problems and neural networks. However, an open question still remains: what is the nature of the transition that takes place in spin-glasses? The non-equilibrium dynamics present in spin-glasses and their dependency on the experimental observation times lead to some authors to dismiss spin-glass as a new thermodynamic phase, but just a dynamic crossover to a frozen non-equilibrium state. On the contrary, the susceptibility cusp observed in the susceptibility, the divergence of the non-linear susceptibility and the existence of a non-zero order parameter are taken as evidence for a static phase transition into the spin-glass phase. Moreover, additional controversy appears in spin-glass-like nanoparticle systems, where the effects of the interplay between intra and interparticle magnetism on the collective behavior is not well understood.

In this work, these questions are addressed by testing the validity of different dynamic and static scaling laws of spin-glass theories to interacting nanoparticle systems. In order to discern the effects of the particles' internal magnetic structure from those caused by size distribution and interactions, a theory that incorporates concepts of superparamagnetism in conventional spin-glass scaling theories was used.

To achieve our objective, AC and DC susceptometry and magnetometry data were collected for cobalt-doped iron-oxide nanoparticle systems. Firstly, highly monodisperse cobalt-doped magnetoferritin nanoparticles were studied and the effects of anisotropy on the collective behavior was examined. Next, the effects of size distribution on magnetite (Fe_3O_4) nanosphere powders were investigated. Lastly, 7 nm Fe_3O_4 nanospheres dispersed into non-magnetic media at different concentrations were analyzed. Noticeable changes in the glass temperature were found among the samples that were linked to changes in anisotropy, size and interparticle spacing. This study yielded critical exponents that were in the range of disordered Heisenberg and Ising antiferromagnets. Moreover, a crossover from collective to single particle freezing was inferred for the dispersed nanoparticle systems.

Acknowledgements

I would like to thank my advisor Dr. Johan van Lierop for his support and constructive feedback during all stages of this research. His patient guidance throughout the scientific process enhanced my understanding of nanomagnetism and how to get things done. I am especially grateful to the members of the Nanomagnetism Research Group who have always been helpful and supportive. Specially to Cherylea Kristalovich and Gurleen Uppal who took care of the transmission electron microscopy and Mösbauer spectroscopy measurements and, equally importantly, guided me through the chemistry of nanoparticle synthesis and taught me how to operate the MPMS and other characterization equipment. I would also like to thank Peiqing Wang for his support with lab equipment and liquid helium.

Finally, I would like to acknowledge the office staff Susan Beshta and Aymsley Bishop-Mahon for their dedicated efforts to support the students in the department.

Contents

List of Figures

List of Tables

Chapter 1

Introduction

Magnetic nanoparticles, and specifically iron oxide nanoparticles, are widely used in medical science, data storage, tissue engineering, and magnetic imaging. Those applications require precise ways to control the magnetic properties of the nanoparticle systems. Enormous theoretical and experimental progress has been made in the last seven decades on understanding and controlling the intrinsic and extrinsic magnetic properties of non-interacting nanoparticle systems [3]. However, when strong interparticle interactions are present in those systems, emergent collective phenomena appear. Understanding the magnetic properties resulting from the interactions, due to its complex behaviour, is an open research topic.

Single-domain magnetic nanoparticles consist of a single uniformly magnetized domain that can flip its magnetization under appropriate conditions. The first theoretical model that explains the magnetization reversal process of single-domain nanoparticles was developed by Stoner and Wohlfarth [4]. This requires the system to overcome an energy barrier called anisotropy energy that depends on the internal composition of the nanoparticle, its volume and morphology [3]. At high temperatures, the thermal energy overcomes the anisotropy energy and the magnetization of the nanoparticles becomes unstable and flips sign spontaneously with a characteristic time that is well described by the Néel-Brown relaxation theory [5, 6]. Two extrinsic properties derive from the anisotropy: the coercivity that measures how much opposing magnetic field the particle can resist without flipping its magnetization, and the relaxation time that measures the average time it takes for the magnetization to flip directions spontaneously due to thermal energy. Being able to control the coercivity of magnetic nanomaterials has led to a number of significant technological applications. Particularly, in the field of information storage, small magnetic particles are promising candidates for increasing the density of magnetic storage devices [7]. Similarly, the ability to tune the relaxation time of nanoparticles has made possible medical treatments, like magnetic hyperthermia, and diagnosis techniques, such as magnetic particle imaging [8]. These applications and related studies often require a way to control the aggregation state of the particles via dispersion in a non-magnetic carrier or coating the nanoparticles with a non-magnetic layer to avoid the effects of interparticle interactions.

At sufficiently concentrated magnetic nanoparticle systems, dipolar interactions become significant. The dipolar energy arising from the interactions modifies the energy barrier generated by the anisotropy contributions of each particle, and hence the spin dynamical properties of the particle system. As a consequence, interactions between randomly distributed nanoparticles can cause a spin-glass-like collective state below a critical temperature, where the magnetic moments of the particles freeze into locally correlated configurations that are characterized by randomness and lack of long-range order. This state is called super-spin-glass since it shares most of the phenomenology attributed to spin-glasses [9].

Spin-glasses are magnetic substances characterized by a random distribution of bonds between neighboring spins that lead to frustration. In contrast to ferromagnets, spin-glasses do not have a well-defined ground state but a complex energy landscape that leads to the emergence of glass-like phenomena. Namely, spin-glasses exhibit non-stationary dynamics that lead to slow relaxation of the magnetization (aging), as well as properties that depend on the temperature history of the material (rejuvenation and memory). Understanding the laws that govern these processes may lead to important theoretical advances in thermodynamics, complex systems and chaos. Some models have been proposed for spin-glasses. Among them, the fractal-cluster model [10] describes many of the fundamental features of the relaxation in real spin-glasses, like the behaviour of the susceptibility near the transition point [10] and the logarithmic time relaxation rate of the magnetization [11]. The cluster model is also used as an argument in favor of the existence of a phase transition since it provides a theoretical framework that validates the critical exponents extracted from scaling analysis of dynamic and static magnetic data [10, 12]. We aim to study the complex interplay between the particle's internal magnetic structure, size distribution, and interparticle interactions that govern the magnetization in nanoparticle systems. Our main objective is to use a model that accounts for both internal and interparticle magnetism to test the validity of the cluster model to describe the superspin-glass transition.

This first chapter provides a theoretical introduction to all relevant topics, such as the magnetic interactions, ordering, phase transitions, spin-glasses and nanoparticle's magnetism. Chapter 2 describes the experimental techniques that were used to characterize nanoparticle properties, including structural and magnetic, which together enable a description of the internal magnetic structure of the nanoparticles. Chapters 3, 4, and 5 present the results and describe the magnetism of the nanoparticle systems. Chapter 3 focuses on the effects of the change in anisotropy by analyzing cobalt-doped magnetoferritin nanoparticles at different dopant concentrations. Chapter 4 studies the effects of the nanoparticle size on strongly interacting systems by analyzing magnetite (Fe_3O_4) nanoparticle powders with different size distributions. In Chapter 5, the effects of interparticle interactions were explored in dispersions of Fe_3O_4 particle systems with different interparticle distances. A summary of the results for all systems that provides a discussion of the effects of anisotropy, size, and concentration in the superspin-glass transition is provided in Chapter 6. Conclusions and suggestions for future work are provided in Chapter 7.

1.1 Bulk magnetism

The magnetism in solids is characterized by the magnetization ($\vec{M}$) defined as the sum of all magnetic moments within its body per unit of volume. The magnetization is a macroscopic quantity resulting from the average of microscopic moments that arise from the spin and orbital angular momentum of bounded electrons in atoms and the motion of electrons in the conduction band. The spatial orientation of the microscopic moments is influenced by thermal motion, inter-atomic interactions, and external magnetic fields ($\vec{H}$). In most solids, the application of an external field induces a net magnetization whose value and direction can be characterized by the magnetic susceptibility (χ), which is defined as

$$\vec{M} = \overleftrightarrow{\chi} \cdot \vec{H}. \tag{1.1}$$

For isotropic materials $\vec{M}$ aligns with $\vec{H}$ and χ is a dimensionless scalar. For $\chi > 0$ it's called paramagnetism; if $\chi < 0$ diamagnetism. Substances that exhibit magnetization in the absence of an external field (Spontaneous Magnetization) are classified in ferromagnetic, antiferromagnetic or ferrimagnetic depending on their magnetic structure.

1.1.1 Paramagnetism

When a paramagnetic material is exposed to an external magnetic field, a magnetization that points in the same direction as the field is induced. Experiments at low fields show that this induced magnetization is directly proportional to the field and inversely proportional to the temperature. The susceptibility is given by the Curie law

$$\chi = \frac{M}{H} = \frac{C}{T}. \tag{1.2}$$

This dependency can be explained by using a simple model consisting of magnetic atoms that tend to align with the magnetic field, but their alignment gets disrupted by their thermal energy. Let's consider a material with isolated or non-interacting magnetic atoms. The atomic magnetic moment is proportional to its total electronic angular momentum $\hbar\vec{J}$

$$\vec{\mu} \; = \; g\mu_B\vec{J}, \tag{1.3}$$

where $\mu_B = e\hbar/2m_e$ is the Bohr magneton and g is the Landé g-factor that characterizes the ratio of magnetic moment to angular momentum for electrons in an atom. For s-orbital electrons, $g \approx 2$.

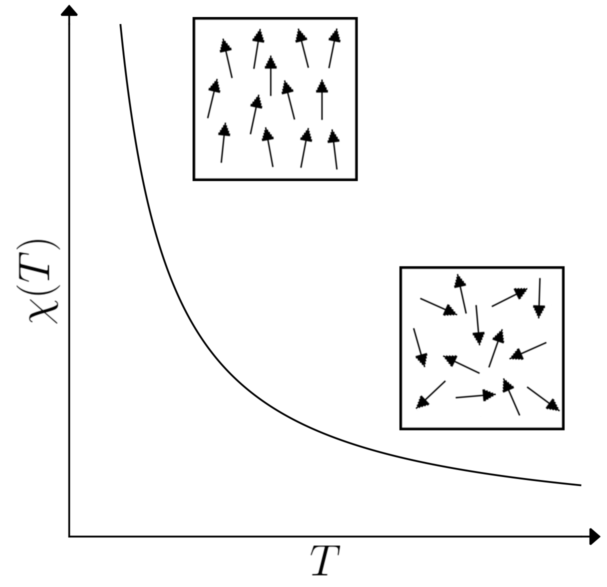

Figure 1.1: Diagram of the Curie law for a paramagnetic material. Thermal energy randomizes the orientation of the magnetic moments.

When the atom is placed in an external field $\vec{B} = B_z e_z$, its energy becomes

$$\vec{\mu} \ = \ g\mu_B B_z J_z. \tag{1.4}$$

According to quantum mechanics the angular momentum is quantized: $\mid \vec{J} \mid = \ J\left(J+1\right)$ and $J_z = m$ where m is an integer or half an integer that takes values from $-J$ to J. The possible magnetic energies of the atom become

$$\varepsilon_m \ = \ -g\mu_B B_z m. \tag{1.5}$$

The probability for the atom to be in the state m is given by the Boltzmann distribution

$$P_m \ \propto \ \exp\left(-\beta\varepsilon_m\right) = \exp\left(\beta g\mu_B B_z m\right), \tag{1.6}$$

where $\beta = 1/K_BT$. The mean $\vec{\mu}$ component on the direction of the applied field μ_z is given by

$$\langle \mu_z \rangle = \frac{\sum_{m=-J}^{J} \exp\left(\beta g \mu_B B_z m\right) g\mu_B m}{\sum_{m=-J}^{J} \exp\left(\beta g \mu_B B_z m\right)} = \frac{1}{Z\beta}\frac{\partial Z}{\partial B_z} = \frac{1}{\beta}\frac{\partial \mathrm{ln} Z}{\partial B_z}, \tag{1.7}$$

where $Z = \sum_{m=-J}^{J} \exp\left(\beta g \mu_B B_z m\right)$ is the partition function of the atom. Using the substitution $x = \beta g \mu_B B_z$ the partition function can be easily calculated as a geometric series with initial term e^{-Jx}

$$Z = e^{-Jx} \sum_{m=0}^{2J} \exp\left(mx\right) = e^{-Jx} \left\{ \frac{1 - \exp\left((2J+1)x\right)}{1 - \exp\left(x\right)} \right\} = \frac{\sinh((J+1/2)x)}{\sinh(x/2)}. \tag{1.8}$$

Substituting (1.8) into (1.7), one obtains

$$\langle \mu_z \rangle = \beta g \mu_B J \mathcal{B}_J(Jx), \tag{1.9}$$

where

$$\mathcal{B}_J(y) = \frac{1}{J}\left\{ \left(J + \frac{1}{2}\right) \coth\left[\left(J + \frac{1}{2}\right) y\right] - \frac{1}{2}\coth\left(\frac{y}{2}\right) \right\} \tag{1.10}$$

is known as the Brillouin function. The magnetization (M) is then the average magnetic moment times the number of atoms per unit of volume (n)

$$M = n g \mu_B J \mathcal{B}_J\left(\frac{g \mu_B J B_z}{K_B T}\right) = M_S \mathcal{B}_J\left(\frac{M_S B}{n K_b T}\right), \tag{1.11}$$

where $M_S = n g \mu_B J$ is the saturation magnetization that could only be achieved if all atomic magnetic moments were aligned in the same direction and is the asymptotic behaviour of $M(H/T)$ for large H/T. Using the expansion

$$\mathcal{B}_J(y) = \frac{(J+1)y}{3J} + O(y^3), \tag{1.12}$$

one can find a simple expression of $M(H/T)$ for small values of field and high temperatures $H/T \to 0$

$$M(H/T) \approx \frac{(J+1)}{3J}\frac{Ms^2B}{nK_BT} = \frac{J(J+1)}{3}\frac{ng^2\mu_0\mu_B^2}{K_B}\frac{H}{T}. \tag{1.13}$$

The susceptibility for small fields and high temperatures then follow the experimentally obtained Curie law

$$\chi(T) = \frac{C}{T}, \qquad \text{where} \qquad C = \frac{J(J+1)ng^2\mu_0\mu_B^2}{3K_B} \tag{1.14}$$

Different values of J speak of different systems. If the atomic magnetic moment is allowed to have only two states $J = 1/2$, the Brillouin equation becomes $\mathcal{B}_{1/2}(x) \equiv \tanh(x)$. On the other hand, if the atomic magnetic moment can align in any spatial direction, as in the classical limit, $J = \infty$ and it reduces to the Langevin function $\mathcal{B}_\infty(x) \equiv \mathcal{L}(x)$. All these functions share similarities, i.e. they reduce to the Curie law for small fields and saturate for high fields. However, they give different values for C and differ in the way they approach saturation.

1.1.2 Magnetic order

For interacting atomic magnets, a spontaneous magnetization can appear at low temperatures. This requires the magnets to be arranged in an ordered manner in such

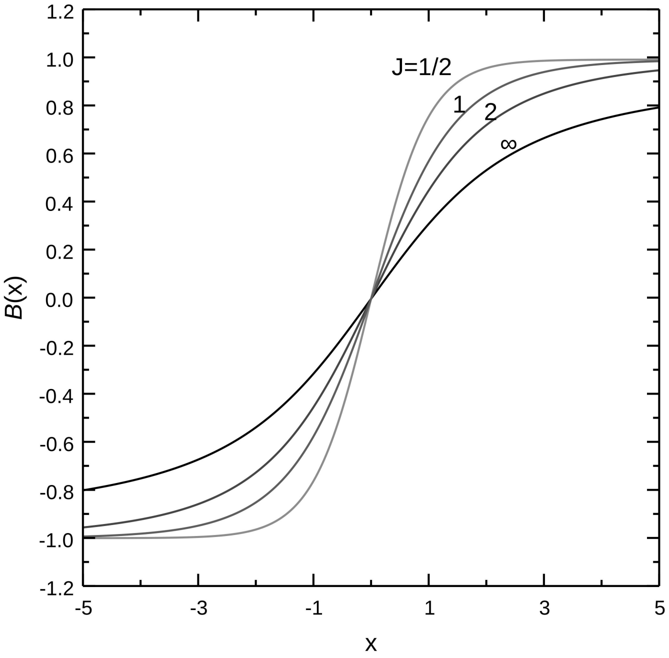

Figure 1.2: Brillouin function for different J parameter, ranging from $\mathcal{B}_{1/2}(y) \equiv \tanh(y)$ to $\mathcal{B}_{\infty}(y) \equiv \mathcal{L}(y)$

a way that the system is able to find an absolute energy minima that leads to magnetic order. The spontaneous magnetization takes place when the system's thermal energy reduces below a critical value given by the interaction energy. Based on the internal magnetic structure of the materials they can be classified as ferromagnets, antiferromagnets, and ferrimagnets, as shown in figure 1.3.

The ferromagnetic alignment can be described using the Hamiltonian

$$\mathcal{H} = -\sum_{ij} J_{ij} \vec{S}_i \cdot \vec{S}_j + g\mu_B \sum_j \vec{S}_j \cdot \vec{B}, \tag{1.15}$$

where J_{ij} are the positive coefficients of the exchange interaction between neighboring atoms and B is the applied magnetic field. In order to solve equation 1.15, the molecular Weiss model can be used. It simplifies the interaction part of the Hamiltonian

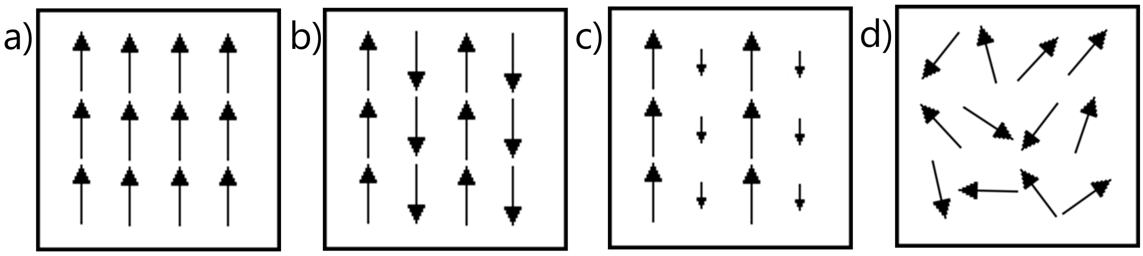

Figure 1.3: Diagram of the internal structure of magnetically ordered systems. a) In ferromagnets the interactions favor alignment. b) In antiferromagnets the energy is minimized when the moments are anti-aligned. c) In ferrimagnets the moments antialign, but a net moment prevails and tends to point along the field. d) The paramagnetic region at high temperatures is characterized by lack of order due to thermal fluctuations.

by switching its term with an internal mean magnetic field. At the site i, it is given by:

$$B_{mf} = -\frac{2}{g\mu_B}\sum_j J_{ij} \cdot \vec{S_j}. \tag{1.16}$$

Substituting in equation 1.15, one get

$$\mathcal{H} = -g\mu_B \sum_j \vec{S_j} \cdot \left(\vec{B} + \vec{B_{mf}}\right), \tag{1.17}$$

which is similar to the Hamiltonian for a paramagnet with field $\vec{B} + \vec{B_{mf}}$. Since B_{mf} is produced by the magnetic order of the system, one can assume that $\vec{B_{mf}} = \lambda M$. Therefore, one can calculate M self-consistently as the mean magnetization produced by this field.

$$\frac{M}{M_S} = \mathcal{B}_J\left(\frac{g\mu_B J\left(B + \lambda M\right)}{K_B T}\right). \tag{1.18}$$

Without the molecular field $\lambda = 0$, and it reduces to the paramagnetic case (equation 1.11). For high temperatures and small fields, the approximation to the

Brillouin function (equation 1.12) can be used, yielding:

$$M \approx \frac{C}{\mu_0}\left(\frac{B+\lambda M}{T}\right), \qquad \text{with} \qquad C = \frac{J(J+1)ng^2\mu_0\mu_B^2}{3K_B}. \tag{1.19}$$

Solving for M results in

$$M \approx \frac{C}{\mu_0}\left(\frac{B}{T-T_C}\right), \tag{1.20}$$

where $T_C = \dfrac{C\lambda}{\mu_0}$ is the Curie temperature. The low-field susceptibility then have the form

$$\chi = \frac{C}{T-T_C} \propto (T-T_C)^{-1}, \tag{1.21}$$

only valid for $T > T_C$. For temperatures below T_C and $B = 0$, equation 1.18 has the trivial solution $M = 0$ and two $M_\pm$ with non-zero values. The solution $M = 0$ is unstable. Therefore, any small fluctuation will push the system to either one of the stable states. As a result, below T_C, even with the absence of a field the system becomes magnetized.

When approaching T_C while heating, calculation for $H = 0$ yields

$$M \propto (T-T_C)^{1/2}, \tag{1.22}$$

while above T_C, $M = 0$. This change of behaviour in the magnetization reveals that a second-order phase transition takes place at T_C. For this transition, the magnetization is the order parameter used to quantify the degree of order in the system and distinguish between ordered (ferromagnetic) and disordered (paramagnetic) phases. The mean-field approach used in this section yields the critical exponents for the ferromagnetic-paramagnetic phase transition $\beta = 1/2$ and $\gamma = 1$, as will be discussed later in section 1.1.3

In antiferromagnets, the energy is minimized when the atomic magnetic moments antialign with their closest neighbors. That can be expressed mathematically by making the coefficient $J_{ij} < 0$ in the Hamiltonian written in equation 1.15. The Weiss molecular field has to be divided then into two sublattices of equal magnetization but opposite direction

$$\begin{aligned} B_+ &= -\lambda M_- \\ B_- &= -\lambda M_+, \end{aligned} \tag{1.23}$$

where the molecular field in one sublattice is determined by the magnetization in the other. Using the same reasoning as for the ferromagnetic case, one can write the magnetization for small fields as

$$M_\mp \approx \frac{C}{\mu_0}\left(\frac{B_\pm + \lambda M_\mp}{T}\right). \tag{1.24}$$

Solving the system of equations yields

$$M = M_+ + M_- \approx \frac{2C}{\mu_0}\left(\frac{B}{T+T_N}\right), \tag{1.25}$$

where $T_N = \dfrac{C\lambda}{\mu_0}$ is the Néel temperature and has the same derived expression as T_C for the ferromagnetic case. The magnetic susceptibility at low field and high temperatures is

$$\chi(T) = \frac{2C}{T+T_N} \tag{1.26}$$

Those results give a way to interpret data above the transition temperature. By fitting experimental data to the Curie-Weiss law

$$\chi(T) \propto \frac{1}{T-\theta}, \tag{1.27}$$

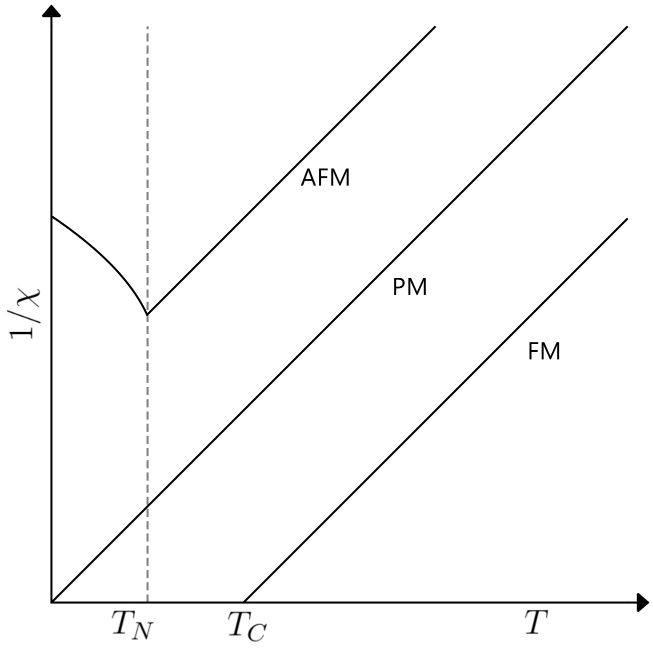

Figure 1.4: Schematic plot of the Curie-Weiss law for different magnetic phenomena.

one can intuit the character of the magnetic order. If the $\theta = 0$ the substance is a paramagnet. If $\theta > 0$ is a ferromagnet with $T_C = \theta$. If $\theta < 0$ is an antiferromagnet and $T_N = \theta$ is expected. Figure 1.4 shows a diagram of how $1/\chi$ varies with temperature for the three cases. In real materials, the measured θ values may differ from the actual transition temperature. This difference is more prominent in antiferromagnets, where the Curie-Weiss temperature is often far away from the real transition temperature [13].

1.1.3 Magnetic phase transitions

The phenomenological Landau theory is usually used as an introduction to phase transitions. The basic idea of this approach is to focus on the local magnetization configurations. Near the transition temperature the magnetization M is small so one can expand the free energy $F(M)$ as a power series

$$F = F_0(T) + \int d^d r \left[\frac{1}{2} a(T) M^2(\vec{r}) + \frac{1}{4} b(T) M^4(\vec{r}) + \frac{1}{2} c(T) (\nabla M(\vec{r}))^2 - H(\vec{r}) M(\vec{r}) \right]. \tag{1.28}$$

Here the coordinate $\vec{r}$ is taken as a continuous, ignoring the discrete structure of the material. The term containing $\nabla M(\vec{r})$ talks about the coupling between neighboring spins. For uniform configurations, in the absence of an external field, the free energy is minimized by

$$\frac{\partial F}{\partial M} = aM + bM^3 = 0. \tag{1.29}$$

The energetic configuration changes abruptly when the parameter $a(T)$ changes signs (see figure 1.5). For $a > 0$, F is minimized by $M = 0$, while for $a < 0$, $M = (-a/b)^{1/2}$ is required. Assuming $a(T) \propto (T - T_C)$ in the vicinity of T_C one obtains

$$M \propto (T - T_C)^{1/2}. \tag{1.30}$$

Also, for a small but uniform applied field $H(\vec{r}) \equiv H$ the minimization condition reads

$$\frac{\partial F}{\partial M} = aM + bM^3 - H = 0 \tag{1.31}$$

and one can find that at the critical temperature $a(T_C) = 0$

$$M \propto H^{1/3}. \tag{1.32}$$

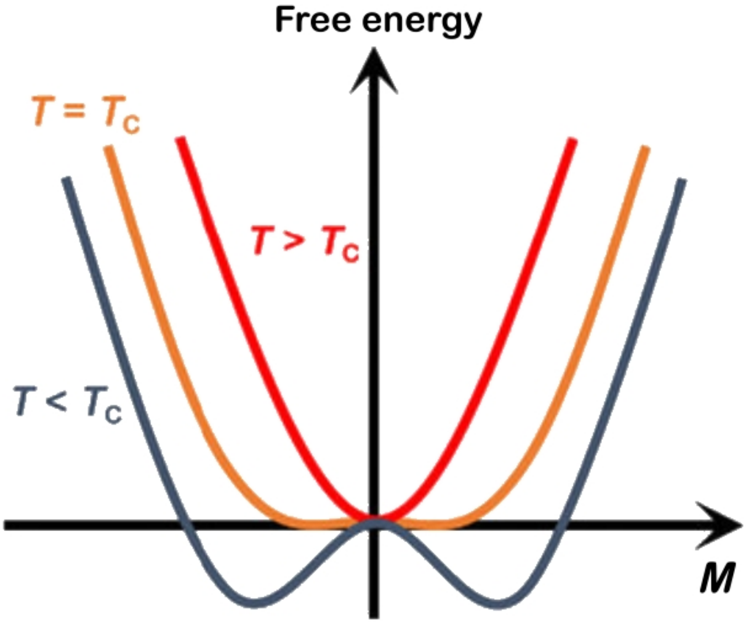

Figure 1.5: Diagram of the Landau free energy $F = aM^2 + \frac{1}{2}bM^4$ in $H = 0$. By assuming $a(T) \propto (T - T_C)$, the change fo sign $a(T)$ leads to a different energy landscape and the emergence of spontaneous magnetization.

Furthermore, if one considers a small magnetic field $H \to 0$ and recall the values of M at zero-field, is easy to derive that the zero field susceptibility is given by

$$\chi(T, H \to 0) \equiv \left.\frac{\partial M}{\partial H}\right|_{H=0} \propto |T - T_C|^{-1} . \tag{1.33}$$

Additionally, the interaction term introduced in equation 1.28 leads to an estimate of the spin correlation length. Discarding the small M^4 term and applying the Fourier transform it is possible to write the free energy as:

$$F - F_0 = \sum_k \left[\frac{1}{2}(a + ck^2)|M_k|^2 - h_{-k}M_k\right] , \tag{1.34}$$

which is minimized by

$$M_k = \frac{h_k}{a + ck^2}. \tag{1.35}$$

For a constant magnetic field, $h_k = \delta(k)$, the susceptibility reduces to equation 1.33. For a spatially varying field $H(\vec{r})$ the non-local susceptibility $\chi(\vec{r})$ can be found. The correlation function in the limit of large-r is

$$C(r) = \langle M(0)M(r)\rangle = Tr\{\chi(r)\} \propto r^{2-d} exp\left[-(a/c)^{\frac{1}{2}} r\right], \tag{1.36}$$

where d is the dimensionality. Thus, spin correlations have a range of

$$\xi = (a/c)^{-\frac{1}{2}} \propto (T - T_C)^{-1/2}. \tag{1.37}$$

This correlation length shows how far thermal fluctuations propagate in the material. At high temperature, the correlation length is small because the fluctuations are so strong that they disrupt any correlation. At low temperature, the fluctuations are small, so again they result in a very small correlation length. Near the critical point, the correlation length increases since the thermal energy is in the range of the interaction energy and diverges at the critical point. Therefore, fluctuations are extremely important near critical points.

As seen in equations 1.30, 1.32, and 1.33, the Landau phase transition theory yields the same exponents that were obtained using the Weiss molecular field, see section 1.1.2. However, this derivation does not depend on the microscopic physical details of the material but comes from the overall symmetry of the system expressed in the expansion 1.28. This gives rise to the concept of universality. Systems that exhibit the same statistical behaviour with the same set of critical exponents are said to form a universality class. This class does not depend on the physical details of the systems or the order parameter used, but on the symmetry group of the Hamiltonian, the dimensionality, and if the interactions are short-ranged or not [14].

The mean-field theory critical exponents for the paramagnetic to ferromagnetic transition are $\beta = 1/2$, $\gamma = 1$, $\delta = 3$, $\eta = 0$ and $\nu = 1/2$ for the equations

$$\begin{aligned} M &\propto (T - T_C)^{\beta} && \text{for} && H = 0,\ T < T_C, \\ \chi &\propto (T - T_C)^{-\gamma} && \text{for} && H = 0,\ T > T_C, \\ M &\propto (H)^{\delta} && \text{for} && H \to 0,\ T = T_C, \\ \xi &\propto \left|T - T_C\right|^{-\nu} . \end{aligned} \tag{1.38}$$

It is important to point out that Landau's theory of phase transitions is not self-consistent. It makes the same assumptions that other classical theories like the Weiss mean-field equation (equation 1.18) do. Namely, it replaces the magnetization with its average value, and fluctuations of that value are ignored. However, this same theory tells us that fluctuations are not negligible near a critical point and in fact diverge at it. Depending on the dimensionality and symmetry, the fluctuation effects may change the qualitative nature of the transition predicted by mean-field theories (e.g. different values of the critical exponents), and, in some cases, the predicted transition point does not even exist [15].

1.1.4 Broken ergodicity and thermodynamic average

The ergodic hypothesis states that, at equilibrium, the system should be found with Gibbs-Boltzmann probabilities, $p \propto e^{-\beta E}$, in any of its possible configurations, and thus, the statistical average over a long period of time will be equal to the average across all possible configurations. In the case of a paramagnet, it means that the spin will explore all accessible orientations, allowing the macroscopic magnetic properties to be calculated as the average of an ensemble of these orientations, $M \equiv \langle S_i \rangle = 0$ at $H = 0$.

However, in the case of a ferromagnet the ergodicity is broken. A ferromagnet with its magnetization pointing up will never be found later in a state where the magnetization is pointing down (in the limit where the number of spins $N \to \infty$). In this case the averages are not conventional Gibbs averages over all the spin configurations, which vanish by symmetry, but rather averages over only a portion of the configuration space, either those with positive net magnetization or those with negative net magnetization. In all cases, broken ergodicity has to be manually included into the equations by restricting the trace used to define thermal averages. This trace restriction can be formally achieved in ferromagnets by keeping a small field term in the Hamiltonian and then taking the limit $H \to 0$ after $N \to \infty$.

It's important to point out that in finite ferromagnetic systems the ergodicity is not broken at $T \neq 0$. Due to thermal fluctuations, the system will be found eventually in the state with the opposite magnetization. The relaxation time of the system τ_0 is the dynamical quantity used to characterize this magnetization flip process and it increases with N as expected. In this scenario we can interpret the thermodynamic averages such as $\langle S_i \rangle$ as averages over an observation time interval $[0, t]$, when $t << \tau_0$. In this dynamical picture, we recover the broken ergodicity after $N \to \infty$, since $\tau_0 \to \infty$ and the limit of long observation times $t \to \infty$ is recovered.

1.1.5 Spin-glasses

Spin glasses are magnetic systems whose spins are unable to reach long-range ordering due to magnetic frustration. In ferromagnets and antiferromagnets, the sign of the exchange coupling between spins favors specific configurations in which the magnetic interaction energies of each pair of spins are minimized simultaneously, leading to long-range magnetic ordering. This is not the case for some spin structures. A triangular lattice, for example, for which the exchange energy of each pair of spins favors anti-alignment cannot minimize all energies simultaneously (see figure 1.6). This phenomenon is called magnetic frustration. Frustrated systems do not have well-defined ground energy states, and thus, at low temperatures the spins will freeze at a state characterized by randomness [16].

Frustration can also be induced in non-frustrated structures by creating randomness. For example, canonical spin-glasses are made by dispersing magnetic atoms (Fe, Mn, Eu, etc.) into a non-magnetic metal, resulting in alloys such as $Cu_{1-x}Mn_x$ and $Au_{1-x}Fe_x$. A crystal structure can also be made random by doping it with magnetic elements (e.g. $Eu_xSr_{1-x}S$ and $La_{1-x}Gd_xAl_2$). Finally, a collection of magnetic nanoparticles interacting via dipole-dipole interactions can become a spin-glass-like

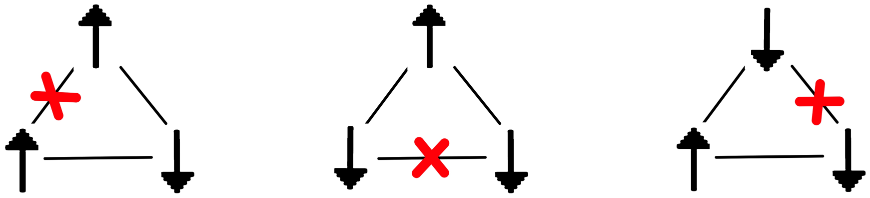

Figure 1.6: Diagram of a triangular spin lattice where each pair of spin's interaction energies favor anti-alignment. If a pair spins is antialigned the third one cannot antialign to both of them simultaneously (represented by the red marks), leading to frustration.

frustrated system due to positional and orientational randomness of the nanoparticles.

The randomness of spin-glasses can be expressed using the Ising Hamiltonian

$$\mathcal{H} = -\sum_{ij} J_{ij} \vec{S}_i \cdot \vec{S}_j, \tag{1.39}$$

with the particularity that we consider J_{ij} to be chosen randomly positive or negative, and independently for each pair of spins. If only close-range interactions between neighboring spins are considered in the sum, equation 1.39 is the Hamiltonian of the Edwards-Anderson model; if long-range interactions are considered, then equation 1.39 is the Hamiltonian of the Sherrington-Kirkpatrick model. We won't delve into any of the specific models, nor into the replica symmetry techniques used to solve the latter. We will focus on explaining the generalities of spin-glasses and presenting the magnitudes that are generally used to characterize the spin-glass to paramagnet transition and its critical behaviour.

When a spin-glass is at high temperatures, the thermal energy overcomes the interaction energies and the system will be in a disordered paramagnetic state. At low temperatures, we expect the system to enter a qualitatively different state, and so, we need an order parameter to characterize this transition. In the case of the ferromagnetic-paramagnetic phase transition, $M \equiv \langle S_i \rangle$ is the order parameter, and a spontaneous $M \neq 0$ appears below the transition temperature. However, due to the lack of long-range periodic order in the frozen spin-glass state, $\langle S_i \rangle = 0$ for this system if one averages over all possible configurations. This is where the concept of broken ergodicity can be used.

Let's assume that the system goes below the glass temperature T_g and enters the

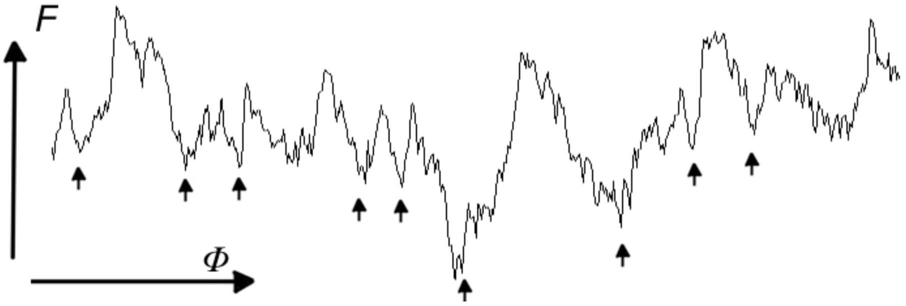

Figure 1.7: Many-valley diagram of a hypothetical free energy as a function of one of the coordinates in the configuration space. Each of the local minima have its own locally metastable magnetic configuration.

spin-glass state. The many-valley picture can help to visualize the glass state (see figure 1.7). The rugged nature of the energy landscape illustrates the many possible configurations the system can adopt and the energy barriers between them. Due to the complexity of glass dynamics, the energy landscape is usually described as having fractal properties and hierarchical structures in which small energy minima are nested within larger ones.

If one assumes that in the observation time, t, the accessible configurations are limited to a region surrounding one local minimum of the free energy in the configuration space, then, the local magnetization

$$m_i \equiv \langle S_i \rangle \neq 0. \tag{1.40}$$

Under this condition, the free energy will be a function of the states surrounding the local minima $F(m_1 \ldots, m_N)$. If we make $N \to \infty$ some of those energy barriers may become infinite and the configuration space may be restricted to one of the many mutually inaccessible valleys that may result. Each valley corresponds to a configuration like the up and down configurations in the ferromagnetic case.

Now, let's assume the system is in one of those valleys. We want to take averages over the distribution of the interactions J_{ij} between each pair of neighboring spins inside this valley (this average is represented as $[\ldots]_{av}$). However, we cannot take the average over m_i since it vanishes due to the random nature of the local magnetization. In the ferromagnetic case, $[\langle S_i \rangle]_{av}$ is the order parameter. But in the spin-glass case, we need higher-order terms such as the mean square local equilibrium magnetization

$$q = [\langle S_i \rangle^2]_{av} = [m_i^2]_{av} = \frac{1}{N} \sum_i m_i^2. \tag{1.41}$$

The magnitude q is called the equilibrium order parameter and it is usually taken as the order parameter that characterize the spin-glasses phase [15].

In a ferromagnet the susceptibility, χ, is the magnetization induced per unit of field H. In spin-glasses we can induce a non-zero q by turning on a random field h_i. If we do so, we obtain

$$\langle S_i \rangle = \sum_j \chi_{ij} h_j \tag{1.42}$$

and therefore,

$$q = [\langle S_i \rangle^2]_{av} = \sum_{ij} [\chi_{ij}^2]_{av} \sigma^2 = \chi_{SG} \sigma^2, \tag{1.43}$$

where σ is the variance of the random field that acts as a conjugate field to the order parameter q, and χ_{SG} is the spin-glass susceptibility, which plays the role that the uniform susceptibility does in a ferromagnet. It is formally defined as

$$\chi_{SG} = [\chi_{ij}^2]_{av} = \beta^2 [(\langle S_i S_j \rangle - \langle S_i \rangle \langle S_j \rangle)^2]_{av}. \tag{1.44}$$

χ_{SG} is measurable through the quantity called the non-linear susceptibility as proposed by Suzuki and Chalupa [17, 18]. It is defined as the coefficient of the $-H^3$ term in the expansion of the magnetization in powers of the external field

$$M = \chi H - \chi_{nl} H^3 + \ldots \tag{1.45}$$

From linear response theory one can derive the relation [15]

$$\chi_{nl} = \beta \left(\chi_{SG} - \frac{2}{3}\beta^2 \right), \tag{1.46}$$

and thus, from χ_{nl} measurements, one can find important information about the nature of the spin-glass transition. Additionally, in the same way a random h_i will induce a $q \propto \sigma^2$, an uniform external field H will also induce a $q \propto H^2$. Thus, an external uniform field can also be used to study the spin-glass transition.

The critical behaviour in ferromagnetic systems that we saw in section 1.1.3 also extends to spin-gasses. In this case

$$\begin{aligned} q &\propto (T - T_g)^\beta && \text{for} && H = 0,\ T < T_g \\ \chi_{SG} &\propto |T - T_g|^{-\gamma} && \text{for} && H = 0, \\ q &\propto (H^2)^\delta && \text{for} && H \to 0,\ T = T_g \\ \xi &\propto\ |T - T_g|^{-\nu}, \end{aligned} \tag{1.47}$$

and the mean-field-theory critical exponents obtained for the spin-glass-paramagnetic transition are $\beta = 1, \gamma = 1, \delta = 2$, and $\nu = 1/2$ [15]

1.1.6 Scaling hypothesis

The Widom-Kadanoff scaling hypothesis combines together the results from equation 1.30, for the growth of the magnetization below T_C in the absence of a field, and equation 1.32, for its dependence with the field at the critical temperature

$$\begin{aligned} M(t,h=0) &\propto \begin{cases} 0 & t>0, \\ \pm|t|^{\beta} & t<0, \end{cases} \\ M(t=0,h) &\propto \pm|h|^{1/\delta}, \end{aligned} \tag{1.48}$$

where $t = (T - T_C)/T_C$ and $h = H/K_B T$ are the reduced temperature and field respectively.

These results form a single formula for $M(t,h)$

$$M(t,h) \propto \begin{cases} t^{\beta} F_M^{+}(h/t^{\Delta}) & t>0, \\ (-t)^{\beta} F_M^{-}(h/(-t)^{\Delta}) & t<0, \end{cases} \tag{1.49}$$

which is assumed valid for $|h|$, $|t| \ll 1$. The critical exponents β and Δ, as well as the scaling functions $F_M^{+}(x)$ and $F_M^{-}(x)$, are assumed to be universal. Figure 1.8 shows a sketch of of the magnetization as a function of h and t. If the data were plotted against temperature, there would be one curve per value of the external field h. But, when $M/|t|^{\beta}$ is plotted against $|h|/|t|^{\Delta}$, these curves collapse to only two, one for $T > T_C$, and the other for $T < T_C$. This phenomenon of the data collapse is the main idea behind the scaling analysis.

We can also use the Widom-Kadanoff scaling hypothesis to analyze the spin-glass transition as well. This requires modifying equation 1.49 by replacing the order

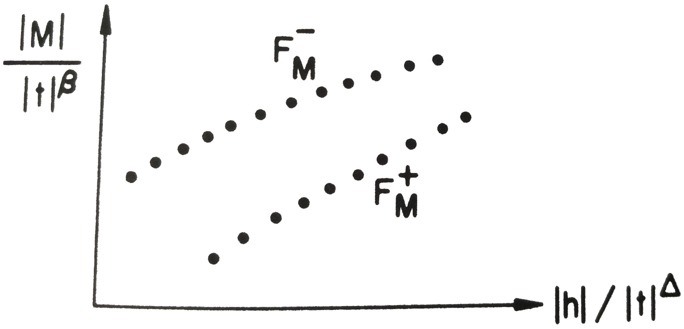

Figure 1.8: Sketch of the magnetization as a function of t and h. Hypothetical data is plotted in a way that shows the points falling into two curves, one for $T > T_C$, and the other for $T < T_C$.

parameters (from M to q) and the field associated to the order parameter (from h to σ^2). For $t > 0$ one can expect that

$$q(t,h) \propto t^{\beta} F\left(\frac{\sigma^2}{t^{\Delta}}\right). \tag{1.50}$$

Now, to be able to apply this theory to experimental data we need to replace the order parameter and the random field for measurable quantities. For this purpose we can use the non-linear susceptibility as proposed by Suzuki and Chalupa [17, 18]. Instead of using $q = \chi_{SG}\sigma^2$ we can use the equivalent

$$R = 1 - \frac{M}{\chi H} = \chi_{nl} H^2 \tag{1.51}$$

to obtain a static scaling relation for spin glasses

$$R(t,h) \propto t^{\beta} F\left(\frac{h^2}{t^{\Delta}}\right), \tag{1.52}$$

where F is a scaling function, $h = H/K_bT$ and $t = (T - T_g)/T_g$ are the reduced field and temperature, respectively, and β and γ are the critical exponents that govern the spin-glass transition.

1.1.7 Dynamic scaling

In dynamic critical phenomena, the fractal-cluster model is widely used. This model assumes the existence of clusters of correlated spins that can have fractal-like shapes. These clusters have a characteristic size that is temperature and field-dependent and determines all physical quantities of the spin-glass [10, 12].

In spin-glasses the correlation length of the function $\chi_{SG}(\vec{r})$ (equation 1.44) diverges in the same way that the correlation length of the spin correlation function does in the ferromagnet (equation 1.37) [15]. Namely, its dependency is given by

$$\xi \propto \left| \frac{T - T_g}{T_g} \right|^{-\nu}, \tag{1.53}$$

where T_g is the spin-glass transition temperature and ν is the critical exponent of the correlation length. The divergence of the characteristic time τ of a system is directly related to the divergence of the correlation length. The fractal-cluster model assumes τ to be governed by power laws [19, 20], i.e.

$$\tau/\tau_0 = |\xi/\xi_0|^z \propto \left| \frac{T - T_g}{T_g} \right|^{-z\nu}, \tag{1.54}$$

where we have to introduce a dynamical exponent z that describes the ratio between the time and space rescaling factors that are characteristics of standard critical slowing down when approaching a freezing temperature with cooling.

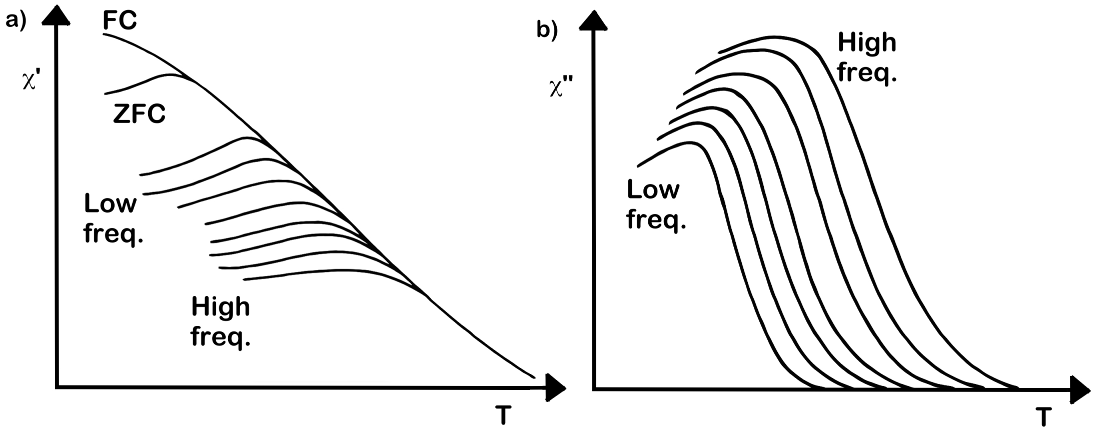

Figure 1.9: Sketch of the typical behaviour of the AC-susceptibility in a spin-glass system. Both in-phase (χ') and out-of-phase (χ'') susceptibilities show a frequency dependent maxima that shifts toward higher temperatures when higher frequencies are used. The curves FC and ZFC represents the static susceptibility measurements.

To extract the dynamical exponents from experimental data the frequency dependency of AC-susceptibility measurements is widely used. Typical AC-susceptibility data is shown in figure 1.9. One simple approach to analyze the data is to fit the frequency dependency of the temperature maxima of χ' into equation 3.4. This way one can get a first estimate of $z\nu$. However, this analysis has no theoretical basis [19, 21].

In order to link the dynamic scaling with the static scaling we need a way to analyze the non-linear part of the susceptibility. As seen in figure 1.9, at high temperatures all χ' curves coincide as expected in the paramagnetic region. As the temperature decreases, a deviation from that main line occurs. One can define the an analogous to the static non-linear susceptibility as

$$\frac{\chi'(T,f)-\chi_{eq}(T)}{\chi_{eq}(T)}, \tag{1.55}$$

where f is the frequency and χ_{eq} is called the equilibrium susceptibility. χ_{eq} can be taken as the low-field static susceptibility (since $\chi_{eq} = \chi'(f \to 0) \approx \chi_{ZFC}$), or alternatively, as the extrapolation to low temperatures of a Curie-Weiss law fit done in the paramagnetic region [19, 22]

One widely used dynamic scaling relation, derived from the cluster model [19, 21], is

$$\frac{\chi'(T,f) - \chi_{eq}(T)}{\chi_{eq}(T)} = \epsilon^{\beta} G(f\epsilon^{-z\nu}), \quad T > T_g, \tag{1.56}$$

where $\epsilon = \dfrac{T - T_g}{T_g}$ is the reduced temperature, and G is a scaling function, with asymptotes

$$\begin{aligned} G(x) &\to x \quad , \quad x \to 0 \\ G(x) &\to x^{\beta/z\nu}, \quad x \to \infty. \end{aligned} \tag{1.57}$$

It's important to point out that discrepancies between the $z\nu$ exponents obtained from equation 3.4 and equation 1.56 may appear. Some authors consider the fit of the temperature maximas to the power law (equation 3.4) to be not suitable to describe the critical dynamics [21, 22], since the maximum value of the χ' differs from the equilibrium value in the high-frequency range, which reduces the validity of this approach to relatively low frequencies. While others point out that the $z\nu$ exponents obtained via equation 1.56 are larger (e.g. $z\nu \approx 11 - 15$ [19]) than those obtained in theory and simulations (e.g. $z\nu \approx 7 - 10$ [23]).

1.2 Superparamagnetism

In bulk ferromagnets the formation of domains minimizes the magnetostatic energy, which is proportional to the volume of the material. But, in sufficiently small particles, the formation of domain walls becomes energetically unfavorable. Thus, a critical size may be reached, below which, the sample consists of a single uniformly magnetized domain. These mono-domain ferromagnetic nanoparticles are in a state of uniform magnetization and behave like small magnets, each having a magnetic moment of thousands of μ_B [3].

The simplest model for magnetization reversal of single-domain non-interacting particles was developed by Stoner and Wohlfarth [4]. It assumes the magnetization reversal is caused by the coherent rotation of all the spins. The anisotropy energy can be written as

$$E_a = KV\sin^2\theta, \tag{1.58}$$

where K is the anisotropy constant, V is the volume of a nanoparticle and θ is the angle of the magnetization with respect to the easy axis (see figure 1.10). When the thermal energy is higher than the activation energy $k_BT > KV$, the ensemble of particles will behave like a paramagnet, with the difference that the independent moments are the sum of moments from the atoms inside each FM particle. These nanoparticle systems are called superparamagnetic. For energies $k_BT \ll KV$ the magnetization reversal can no longer occur and the particles will appear to be blocked in one of the two states. The temperature that describes this transition to the blocked state is the superparamagnetic blocking temperature T_B

For $k_bT > KV$ the particle overcomes the anisotropy threshold by thermal energy.

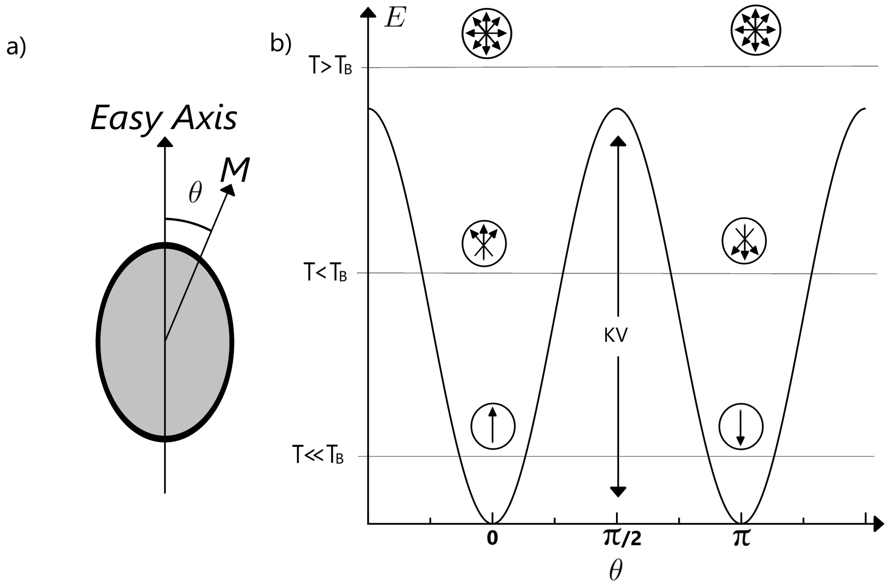

Figure 1.10: a) Illustration of an uniaxial anisotropic superparamagnet at zero field with its magnetization M pointing along some angle θ with respect to the easy axis. b) Dependence of the anisotropy energy on the magnetization axis. For $T < T_b$ the M is blocked in one of the two states. Increasing the temperature causes temporal fluctuations around those values. For $T > T_b$ spontaneous magnetization reversals occurs.

However, it's rotation is still hampered by the potential wells. Therefore, the direction of magnetization will fluctuate between the two energy minima with a characteristic frequency f or relaxation time $\tau = (2\pi f)^{-1}$ described by the Néel relaxation model [5, 6]

$$\tau = \tau_0 \exp\left(\frac{KV}{k_b T}\right) \tag{1.59}$$

where τ_0 is a material-dependent characteristic length of time called the attempt time, whose measured value is usually in the range of $\sim 10^{-11} - 10^{-8}$ s [24]. τ_0 is usually attributed to gyromagnetic precession in the anisotropy field [24, 25]. According to the model, the relaxation frequency can be understood proportional to the probability of the system to switch from one energy minimum to the other, overcoming the energy barrier KV. Thus, equation 1.59) is a Boltzmann distribution. For high temperatures, when the relaxation time τ is larger than the experimental measuring time τ_m, the measured magnetization will be averaged out to zero. Only when the temperature is lowered and $\tau_m \sim \tau$ the system appear blocked, and a net magnetization can be measured. The superparamagnetic blocking temperature T_b can be found then by inverting equation. 1.59,

$$T_b \approx \frac{KV}{k_b T}\ln\left(\frac{\tau_m}{\tau_0}\right). \tag{1.60}$$

Equation 1.60 is valid for individual particles or a system of non-interacting particles with the same size and anisotropy. The blocking temperature is not unequally defined but depends on the measuring time of the experiment. Experimental techniques have different measuring times depending of the physical principle they use. For inelastic neutron scattering $\tau_m \sim 10^{-12} - 10^{-10}$ s, Mössbauer spectroscopy $\sim 10^{-10} - 10^{-7}$ s, and a typical AC magnetometry $\sim 10^{-5} - 10^{-1}$ s [3]. While this dynamical behaviour is often regarded as being due to individual particle blocking, the interparticle interactions often change the frequency dependencies [26].

1.2.1 Anisotropy

Magnetic materials have anisotropy, which is a term that describes the dependency of the energy on the direction of the spontaneous magnetization. When a magnetic material is exposed to a field the anisotropy affects the direction of the magnetization, creating easy axes that are energetically favorable for the spins to align with, and hard axis that act as energy barriers. The dependency of the energy with respect to the axis can be written as

$$E_a = K_1\sin^2(\theta) + K_2\sin^4(\theta) + K_3\sin^6(\theta) + \ldots \tag{1.61}$$

where K_1 and K_2 are anisotropy constants, and θ is the angle between the magnetization and the easy axis. There are multiple factors that contribute to the anisotropy. The spin-orbit coupling is responsible for intrinsic (magnetocrystalline) anisotropy, while in fine particles, thin films, and nanostructures, other kinds of anisotropies such as shape and surface anisotropy are relevant [27].

1.2.2 Coercivity

In anisotropic materials, when an external field H is applied at an angle ϕ with respect to the easy axis, the magnetization will lie along a different angle θ. The Stoner-Wohlfarth model then dictates that the relevant part of the free energy is given by

$$E(\phi,\theta) = KV\sin^2\theta - \mu_0 H M_S V\cos(\phi-\theta), \tag{1.62}$$

where M_S is the saturation magnetization of the particle, $(\phi-\theta)$ is the angle between the magnetization and the field as shown in figure 1.11.a. Minimizing $E(\phi,\theta)$, one obtains the hysteresis loops shown in figure 1.11.b. When the magnetic field is either aligned ($\phi = 0$) or anti-aligned ($\phi = \pi$) to the easy axis, the hysteresis has a rectangular shape, the remanent magnetization is $M_r = M_S$ and the coercivity is $H_C = 2K/M_S$. On the contrary, when the field is perpendicular to the easy axis ($\phi = \pi/2$) no hysteresis is found in the Stoner-Wohlfarth model. For an ensemble of non-interacting particles with randomly oriented anisotropy, these values can be calculated for $T = 0$ as $M_r = 0.5M_S$ and $H_C = 0.96K/M_S$.

When thermal energy is taken into account, for $T > 0$, the value of $H_C(T)$ is given by the competition between the thermal and magnetic energies. A description

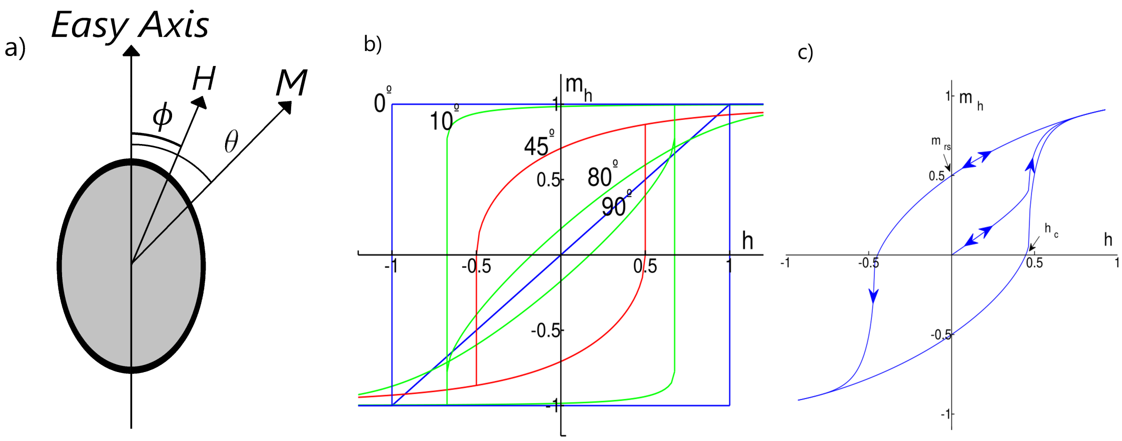

Figure 1.11: Hysteresis loops of $m = M/M_S$ versus $h = M_S H/2K$ calculated for single-domain nanoparticles with uniaxial anisotropy. a) Direction of the field H and the magnetization M pointing along some angles ϕ and θ, respectively. b) Hysteresis loops for different orientations of the particle easy axis relative to H. c) Hysteresis loop calculated for a randomly oriented assembly of particles.

of $H_C(T)$ can be found by combining the Néel relaxation model (equation 1.59) and the Stoner-Wohlfarth model (equation 1.11) as done in [28].

$$\mu_0 H_C(T) = \frac{2K}{M_S}\left(1 - \sqrt{\frac{T}{T_B}}\right). \tag{1.63}$$

This expression is only valid for temperatures below the blocking temperature, $T < T_B$, where blocked states yield $H_C > 0$.

1.2.3 Saturation

As seen in section 1.1.1, for a classical paramagnetic material composed of atoms whose magnetic moments can align in any spatial direction, the magnetization $M(H/T)$ follows a Langevin function (equation 1.11). Substituting the atomic magnetic moments for the magnetic moments of the whole particles we can find a similar equation for superparamagnets [29]

$$M(H/T) = M_S \mathcal{L}\left(\frac{M_S V \mu_0 H}{K_b T}\right), \tag{1.64}$$

valid only for $T > T_B$ where M_S is the magnetic saturation of the whole ensemble of nanoparticles and V is the average magnetic volume of the nanoparticles. Taking into account the size distribution of an ensemble of particles, the magnetization can be found as the convolution of the volume distribution function $f(V)$ and equation 1.64,

$$M(H/T) = M_S \frac{1}{\nu} \int_0^\infty \mathcal{L}\left[\frac{M_S V \mu_0 H}{K_b T}\right] V f(V) dV, \tag{1.65}$$

where $\nu = \int_0^\infty V f(V) dV$. When approaching the blocking temperature this conventional Langevin-type behaviour may be sensitively modified by the anisotropy, since anisotropy has a significant influence on the low field equilibrium magnetization $M(H,T)$ as $T \rightarrow T_b$ [30, 31].

The saturation of the particles is also influenced by temperature. The internal magnetic structure of the particles is usually composed of a single-domain ferro-, ferri- or antiferromagnet whose critical temperature usually sits far above the temperature range of the experiments. In this ordered state fluctuations arise from collective spin-wave excitations. In the bulk the temperature dependence of the internal magnetization of the particles $M_S(T)$ decreases with temperature as the Bloch $T^{3/2}$ law [32]

$$M_S(T) = M_0 \left[1 - BT^{3/2}\right], \tag{1.66}$$

where M_0 is the limit of $M_S(T)$ as $T \rightarrow 0$ and B is a coefficient that depends on the structure of the crystal lattice and the strength of the exchange interaction.

Deviations from $T^{3/2}$ law has been found both from the numerical solution of the Heisenberg spin clusters [33, 34], and from experiments with nanoparticles [35]. Experimental values ranges from $0.5 - 3$. The causes are usually attributed to gaps in the spin-wave spectrum that appear due to the small size of the nanoparticles or high crystalline anisotropy.

1.2.4 Interparticle interactions

In practice, interactions between the magnetic nanoparticles are always present. Particles interact with each other via dipolar interaction, leading to a cooperative effect at low temperatures. The dipolar energy arising from the interactions modifies the energy barrier generated by the anisotropy contributions of each particle, and hence the spin dynamical properties of the particle system. In this case, priority may be given to the total free energy of the system, while single-particle energy barriers are no longer solely relevant. The reversal of one particle moment may change all energy barriers within the system. To describe the relaxation time of interacting nanoparticle systems, Tholence [36] suggested that the Néel-Arrhenius law, equation 1.59, should be modified such that $T \to T - T_0$, which leads to the Vogel-Fulcher law

$$\tau = \tau_0 \exp\left\{ \frac{KV}{k_B \left(T - T_0\right)} \right\}. \tag{1.67}$$

This modification is necessary to fit the temperature dependence of τ and to explain the magnitude of the activation energy of the relaxation process [37]. Theoretical calculations of T_0 and τ_0 are hard to do in practice, and only models based on approximations exist. In the cluster model, values for T_0 and τ_0 can be derived from the particle coupling energies by assuming the system to be formed by correlated clusters of effective volume estimated from the correlation length of the magnetization [37, 38].

The Curie-Weiss law seen in superparamagnetic particles also gets modified by interparticle interactions. If we consider a system of non-interacting dipoles whose dipolar moments μ can be oriented parallel or anti-parallel to the applied field H, the free energy per particle of the system can be written as.

$$F = -\mu H p + \frac{1}{2}(1+p)K_bT\ln((1+p)/2) + \frac{1}{2}(1-p)K_bT\ln((1-p)/2), \tag{1.68}$$

where $-1 \leq p \leq 1$ is an order parameter representative of the fraction of dipoles pointing parallel to the field, named reduced magnetization. If the order parameter is small, $|p| << 1$, equation 1.68 becomes

$$F = -\mu H p + \frac{1}{2}K_bTp^2, \tag{1.69}$$

which reduces to the $p = \dfrac{\mu H}{K_bT}$ expected in paramagnets. If the system is weakly interacting, then we can add a Landau expansion to equation 1.68 to represent the interaction-free energy. Therefore, the total interaction energy per particle is given by

$$F = -\mu H p + \frac{1}{2}K_bTp^2 + ap^2 + bp^4 + \ldots = -\mu H p + p^2(\frac{1}{2}K_bT + a), \tag{1.70}$$

taking only the term p^2 since $|p| << 1$. Minimizing equation 1.70 gives

$$p = \frac{\mu H}{K_bT + 2a}, \tag{1.71}$$

and therefore, if we call $2a/K_b = T^*$, the reduced susceptibility for a weakly interacting dipolar system is

$$\chi_r = p/H = \frac{\mu}{K_b(T - T^*)}, \tag{1.72}$$

which is equivalent to the Curie-Weiss law as observed in ferromagnets. This approach cannot predict a quantitative value for the order temperature T^*. A detailed microscopic approach is required to obtain an expression for T^* as done in [39].

Chapter 2

Experimental methods

The synthesis and experimental techniques are described in this chapter. Several nanoparticle systems were synthesized by thermal decomposition. The crystal structure and morphology of the nanoparticles were determined using powder x-ray diffraction (XRD) and transmission electron microscopy (TEM). Mössbauer spectroscopy identified the valence state and local environment of Fe cations and thus the magnetic structure of the iron oxide. Magnetic properties were studied using magnetometry and susceptometry.

2.1 Synthesis of Fe_3O_4 nanoparticles

Fe_3O_4 nanoparticle systems with different mean diameters were prepared by thermal decomposition following the method described in [40]. First we create the precursor. 10 mmol (2.7 g) of iron(III) chloride hexahydrate ($FeCl_3{\cdot}6H_2O$) (98% Alka Aesar) was dissolved in 120 ml of distilled water, and 30 mmol (9.1 g) of sodium oleate

($NaC_{18}H_{33}O_2$) (97% TC America) was dispersed in 80ml of ethanol. This creates $FeCl_3$ and sodium oleate solutions, respectively. The solutions were poured into a 500 ml 3-neck flask and stirred for 15 min under vigorous agitation to form a homogeneous black mixture. The reaction mixture was heated up to 85°and kept at reflux for 4 h. Thereafter, the mixture was cooled, transferred to a separatory funnel, and washed 3 times with 50 ml of warm distilled water to remove the NaCl byproduct of the reaction. Afterwards the organic top layer was separated, transferred to a beaker an left to dry at room conditions for 3 weeks, forming a black waxy liquid. The resulting iron(III) oleate ($FeOl_3$) was used as the precursor for the Fe_3O_4 nanoparticles syntheses.

Different amounts of previously synthesized Fe_3Ol and oleic acid surfactant (99% Thermo Fisher) were mixed with 15m l of 1-Octadecene ($C_{18}H_{36}$) (90% Thermo Fisher) in a 250 ml 3-neck flask. The mixture was then heated to 120° C under air for 1 h to remove moisture, and then heated to 325° C with a temperature ramp rate of 20-30° C and let it reflux for 2 h. Subsequently, the mixture was washed three times with chloroform/acetone in a 1/4 volume ratio and precipitated using a magnet. The resulting samples were dispersed in hexanes.

In order to create weakly interacting nanoparticle systems, a portion of the samples were further diluted in paraffin at 60 °C. Alternatively, in order to make strongly interacting nanoparticle systems, another portion of the samples were washed by dispersing them in xylenes and heating the dispersion to 100 °C for 30 min, obtaining a magnetic black powder.

2.2 Powder x-ray diffraction (XRD)

Crystallography uses the diffraction of x-rays, neutrons, or electrons to determine the structure of a crystalline solid. Incident x-rays interact with the electron cloud surrounding each atom, producing secondary spherical waves in a process known as elastic scattering. Given the spatial periodicity and symmetry of the crystal, the scattered rays will interfere, generating a diffraction pattern. The optical path length of the rays is determined by the distance between crystallographic planes d_{hkl} labeled by the Miller indices hkl (see figure 2.1). High-intensity regions take place at the angles θ where the difference in optical path length from the interfering rays are integer multiples of the wavelength ($n\lambda$), and are described by the Bragg equation:

$$n\lambda = 2d_{hkl}\,\sin(\theta) \tag{2.1}$$

Powder x-ray diffraction makes use of the random orientation of crystals in a powder sample to compress the 3D spatial information into a 1D diffraction pattern. The measured reflection positions and intensities are like fingerprints of particular crystalline phases. Identification is accomplished by comparison of the measured pattern with reference databases using a search-match algorithm [41].

The width of the reflections also gives information about the crystal structure. It is inversely proportional to the crystallite size, which is the length of the diffracting domains where the crystal structure has the same crystallographic orientation. The broadening of the reflections due to crystallite size is described by the Scherrer formula [42]:

$$\tau = \frac{K\lambda}{\beta\cos(\theta)}, \tag{2.2}$$

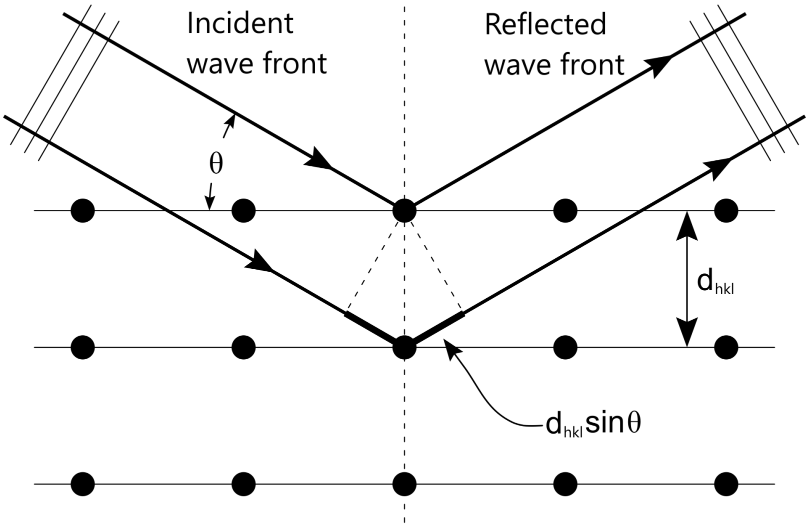

Figure 2.1: Schematic diagram of the Bragg diffraction. Constructive interference occurs only when the difference in optical path length is an integer multiple of the wavelength.

where τ is the mean crystallite size, K is a dimensionless shape factor with a typical value of 0.9 for spherical domains, and β is the broadening of the reflection in radians.

X-ray diffraction patterns were collected on all samples to determine the crystal structure, composition, and crystallite size, using a Bruker D8 DaVinci diffractometer with Cu-K_α (8.04 keV) radiation in Bragg-Brentano geometry (Figure [41]). The x-ray tube produces a beam of electrons (40 mA) from a heated tungsten cathode, which then are accelerated in vacuum by an excitation voltage (40 kV) and hit the Cu-anode, generating characteristic Cu x-rays on top of a background of Bremsstrahlung radiation. The primary set of optics collimates the x-rays and focuses them to the sample surface. It consists of one programmable and one Soller slit that collimate the beam in the x and y axes, respectively. The secondary set of optics consists of a programmable slit that refocuses the beam into the detector and a Ni-filter that

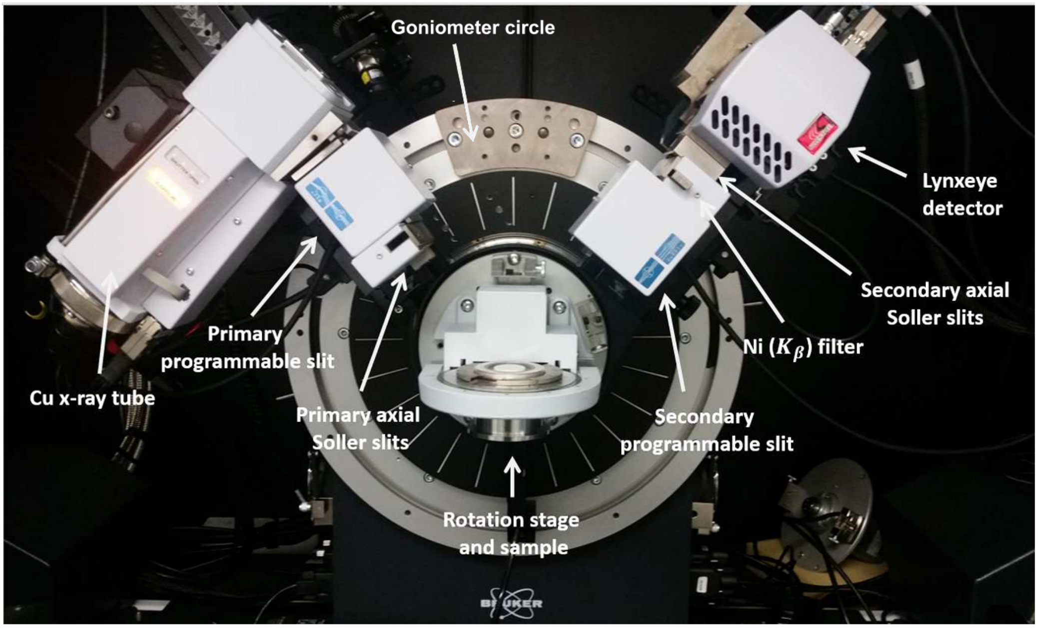

Figure 2.2: Bruker D8 DaVinci diffractometer using a Bragg-Brentano geometry. The main components are identified.

attenuates the Bremsstrahlung and Cu-K_β rays. The detector consists of a Lynxeye Si 1D-strip. The x-ray tube, optics, and detector are held by mechanical arms that move along the goniometer circle, and their positions are tracked and controlled by software.

The patterns were collected using dried nanoparticle samples placed on a zero-background quartz slide positioned on top of a rotation stage. The structural information from the samples was extracted using computational and analytical methods, i.e. Rietveld refinement [43].

2.3 Transmission Electron Microscopy (TEM)

Transmission electron microscopy is a technique that uses a beam of electrons to form an image. It produces significantly higher resolution than light microscopes due to the smaller de Broglie wavelength of electrons

$$\lambda = \frac{h}{p} = \frac{h}{m_e v}, \tag{2.3}$$

where h is the Planck constant and p, m_e, and v are the momentum, mass, and velocity of the electrons, respectively. For electrons emitted into vacuum from a heated filament and accelerated through a potential difference of 50 V, $v \approx 4.2 \times 10^6$ m/s and $\lambda = 0.17$ nm, and they will be strongly diffracted by the atoms at the surface of a crystal. With an even higher accelerating voltage of 50 kV, $\lambda = 5$ pm and the electrons can penetrate distances of several micrometers into a solid and be diffracted by atomic planes inside the material [44]. The transmitted electron beam loses intensity as it travels through the material, and the resulting attenuation can then be related to the thickness, spatial orientation of the crystal, and atomic number Z of the ions [45]. Focusing the transmitted electrons using magnetic lenses allows us to create images at the nanometric scale. Nowadays, the use of high-resolution transmission electron microscopy (HRTEM) gives the possibility of studying the atomic configuration of solids with a resolution of 0.08 nm [46].

TEM samples were prepared by suspending the nanoparticle systems in hexanes and depositing a drop on top of a 200-mesh carbon-coated copper grid. To determine the particle size distributions, low magnification images containing a large sample of nanoparticles were taken. The diameter of individual particles was measured using the image processing software ImageJ [47]. Around 300-500 particles where measured per sample and their diameters were plot with histograms and fitted to log-normal distributions [48, 49]

$$P(d) = \frac{1}{\sigma d\sqrt{2\pi}}\exp\left(-\frac{(\ln\, d\ - \mu)^2}{2\sigma^2}\right), \tag{2.4}$$

where d is the particle diameter and the mean particle diameter d_0 and standard deviation Δd can be calculated as $d_0 = \exp\left(\mu + \frac{1}{2}\sigma^2\right)$ and $(\Delta d)^2 = [\exp(\sigma^2) - 1]\exp\left(2\mu + \sigma^2\right)$, respectively.

2.4 Mössbauer Spectroscopy

Mössbauer spectroscopy is a useful technique that allows to study the local atomic environment of a sample by analyzing the resonant absorption and emission of gamma rays. Due to its sensitivity, it can detect subtle changes in the local electronic and magnetic environments of the target nuclei, giving information about its coordination number and position in the crystal lattice. Also, in magnetically ordered materials, e.g. ferromagnets, the atomic nucleus experiences a local magnetic field generated by the atom's electrons and neighboring atoms via exchange interactions. This internal magnetic field causes a splitting in the energy level of the nucleus that can be detected using Mössbauer spectroscopy. Therefore, this technique is very useful for studying the magnetic structure of materials. Moreover, the time scale of Mössbauer spectroscopy is on the order of nanoseconds, covering a range of relaxation times that are not easily measured by other techniques, e.g. AC magnetometry and neutron diffraction [50]. Thus, Mössbauer spectroscopy is also widely used to study the relaxation phenomena in paramagnetic materials and nanoparticle systems, since it complements the lack of site specificity and slow measurement time scales of magnetometry. In paramagnets due to the lack of magnetic order, an external magnetic field is usually required.

The Mössbauer technique makes use of the recoilless absorption of γ-rays that takes place in solids. γ-rays carry momentum, so when they are generated by free nuclei of mass (M), they will lose some energy, which becomes kinetic energy (recoil) of the nuclei due to the momentum conservation. The resultant energy loss E_R is given by:

$$E_R = \frac{E_0^2}{2Mc^2} \tag{2.5}$$

where E_0 is the energy of the nuclear transition that generated the γ-rays and c is the speed of light. The energy of the emitted γ-rays will then be reduced by this amount, $E_\gamma = E_0 - E_R$. Similarly, to excite the same transition in a free nucleus, a more energetic radiation $E_\gamma = E_0 + E_R$ is required. The recoil phenomenon induces an energetic separation between the emission and absorption lines of $2E_R$. In solids, the nuclei are bound, and the recoil energy is transmitted to the vibrational modes of the crystal lattice. Since those modes are quantized, when the recoil energy is less than the lowest vibrational energy, a recoil-free absorption has a probability of occurring.

In Mössbauer spectroscopy, the radioactive source moves towards and away from the sample with periodic and controlled velocities. The relative motion shifts the energy of the γ-rays due to the Doppler effect. The transmitted photons are detected with a γ-counter and recorded as a function of the drive velocity. This is known as the Mössbauer spectrum. The overlap of the Doppler-shifted emission line and absorption line determines the strength of the nuclear γ-rays absorption. Maximum

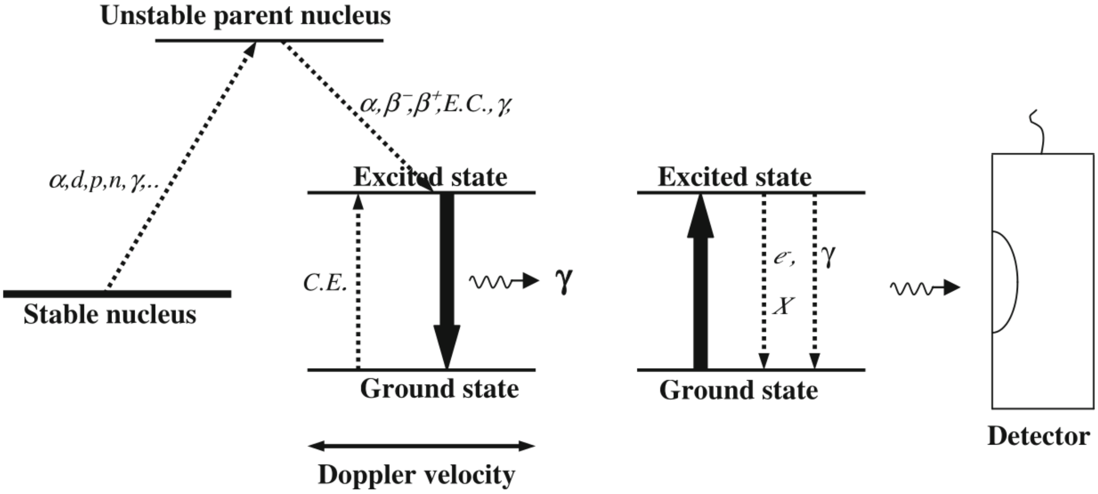

Figure 2.3: Schematics of the emission and absorption of γ-rays in Mössbauer spectroscopy.

absorption is achieved when there is a complete overlap of shifted emission and absorption lines. Those absorption lines deviate from the source γ-rays due to hyperfine interactions. The interaction of the nucleus with its surrounding electron cloud produces a shift and/or split of the nuclear levels. Due to its complexity, this interaction can be separated into components called the hyperfine interactions [51]. By analyzing these energy shifts/splits, it is possible to measure the local electronic and magnetic environments surrounding the target nuclei. There are only three kinds of interaction that must be considered in practical Mössbauer spectroscopy: the electric monopole interaction that causes the isomer shift (δ), the electric quadrupole interaction that generates the quadrupole splitting (QS), and the magnetic dipole interaction that results in the hyperfine splitting [50]. They are shown in figure 2.4

The deviation of the spectra center with respect to the zero velocity is called isomer shift δ. It is caused by the interaction between the charge distribution in the nucleus

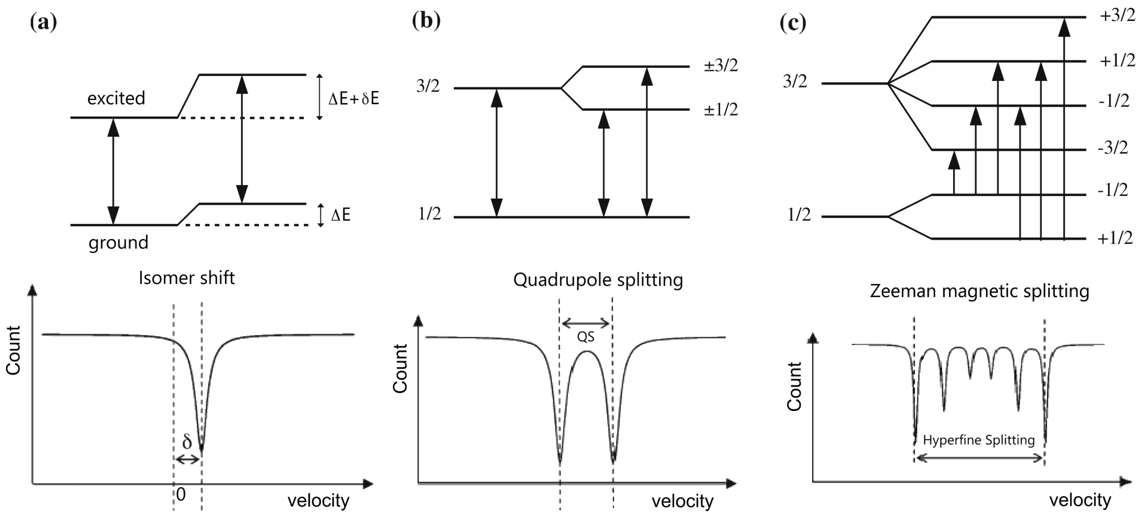

Figure 2.4: Schematics of the hyperfine interactions. a) isomer shift, b) quadrupole splitting and c) Zeeman magnetic splitting.

and the electron cloud. The charge density of the nucleus can be approximated using a Taylor expansion. The first relevant term can be split into an isotropic (monopole) and an anisotropic (quadrupole) component [50]. The isotropic part depends only on the radial part of the electric field. It can be calculated using a classical Coulomb potential, assuming that the nucleus is a uniformly charged sphere surrounded by the radially symmetric s-orbital electrons. This interaction causes a uniform shift ΔE of both the nuclear ground and excited energy states. However, a small difference δE also appears, giving rise to the isomer shift δ of the Mössbauer spectrum (figure 2.4.a).

The anisotropic component of the electric nuclear moment interacts with the electric gradient field caused by the non-radially symmetric part of the electron cloud. It produces a quadrupole splitting. Nuclei with spin $l = 0$ and $l = \frac{1}{2}$ have spherical symmetry and hence, the quadrupole momentum is zero, e.g. the ground state of ^{57}Fe. Those states don't exhibit quadrupole splitting. Those with $l > \frac{1}{2}$ may have a quadrupole momentum e.g. the excited state of ^{57}Fe with $l = \frac{3}{2}$. Therefore, as shown in figure 2.4.b, the ground state of ^{57}Fe remains undivided, but the excited state splits into two double degenerated states $m_l = \pm\frac{3}{2}$ and $m_l = \pm\frac{1}{2}$.

The magnetic hyperfine splitting is caused by the interaction between the nuclear magnetic dipole moment and its surrounding magnetic field. The presence of a magnetic field in a nucleus with spin l lifts the degeneracy of its $2l + 1$ energy levels, as shown in figure 2.4.c. The resulting split is called the nuclear Zeeman effect. For ^{57}Fe, both ground and excited energy levels have magnetic dipole momentum and interact with the magnetic field produced by the electron cloud. The ^{57}Fe ground state has $l = \frac{1}{2}$ and splits into two levels: $m_l \in \left\{-\frac{1}{2}, \frac{1}{2}\right\}$, while the excited state $(j = \frac{3}{2})$ splits into four: $m_l \in \left\{-\frac{3}{2}, -\frac{1}{2}, \frac{1}{2}, \frac{3}{2}\right\}$. A total of eight γ-transitions can be expected from ground to excited state, but only six of them occur in practice due to the dipole selection rules $\Delta l = 1$, $\Delta m_l = 0, \pm 1$.

2.5 Magnetic Property Measurement System (MPMS)

The magnetic properties of a system are usually determined by the measurements of static and dynamic magnetization using a magnetic properties measurement system (MPMS). Because of its high sensitivity, the use of a superconducting quantum interference device (SQUID) magnetometer is required to detect the small magnetic signal of nanoparticle systems, even more so if they were dispersed in non-magnetic media to reduce the effect of interparticle interactions.

The SQUID-MPMS combines several superconducting components, including a SQUID, detection coils, superconducting magnet, and superconducting shields [52].

Figure 2.5.a shows a schematic of the components. SQUID devices consist of a closed superconducting loop that includes one or two Josephson junctions in the loop's current path that makes it extremely sensitive to changes in the magnetic flux. The superconducting loop also includes the detection coil that surrounds the sample area. It consists of a single superconducting wire bent in a set of three coils in a configuration called second-order gradiometer, capable of detecting the change rate of the gradient (second derivative) of a magnetic field (see figure 2.5.b). This configuration is used to reduce the noise caused by magnetic fluctuations in the superconducting magnet [53]. A magnetic field of up to 5T can be applied to the sample area by a superconducting magnet. It consists of a closed-loop superconducting solenoid that can be charged up to a specific current and be operated in persistent mode without the need of an external power supply or current source. Due to the high sensitivity of the detector to magnetic fluctuations, the SQUID sensor must be shielded from the strong magnetic fields produced by the superconducting magnet using a superconducting shield. This shield also reduces fluctuations from environmental magnetic fields, granting a volume of stable and relatively low magnetic field in which the SQUID can operate. Because of the superconducting nature of the MPMS components, the whole chamber is submerged in liquid helium inside a double-walled vacuum vessel (dewar). The magnetic properties of the nanoparticle systems were characterized using a Quantum Design SQUID MPMS-XL-5. The sample was mounted in plastic straws and inserted using a row. The sample motion was controlled by a reciprocating sample option system (RSO) that uses short-range periodic movements of the sample through the coils to produce an oscillating AC signal in the SQUID. This method increases the sensitivity of DC measurements. The temperature (T) is controlled by helium gas flow from a reservoir at the bottom of the dewar and a heater above the sample. The

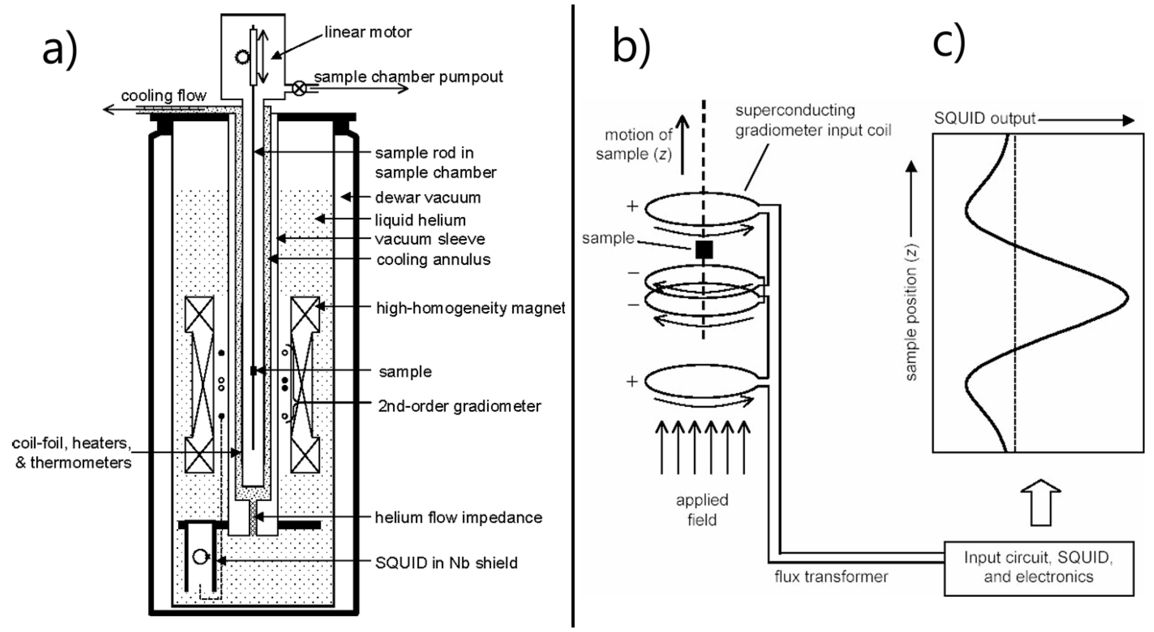

Figure 2.5: a) Schematics of the MPMS showing the main components. b) Gradiometer, the upper coil and the bottom coils area single turn bent clockwise, and the center coil have two turns bent counter-clockwise. c) The output voltage of the SQUID as as a function of the sample position.

magnetic field (H) is controlled by the intensity of the persistent current circulating through the superconducting magnet coil. The magnetic response from the sample couples inductively to the detection coils as the sample moves through them and this signal is converted to voltage thanks to the Josephson junctions in the SQUID (see figure 2.5.c). The voltage is then fitted with a magnetic dipole approximation to extract the magnetization (M). AC measurements uses

DC susceptibility χ_{dc} measurements were performed in field cooling (FC) and zero field cooling (ZFC) protocols, using small applied field values of 50 Oe and temperatures ranging from 5 K to 300 K. AC susceptibility χ_{ac} measurements were done in ZFC using a small drive field of 2.5 Oe and seven frequencies ranging from

10 Hz to 1 kHz from 5 K to 300 K. Hysteresis loops were measured from −25 kOe to 25 kOe at selected temperatures from 5 to 300 K. For the samples dispersed in paraffin the field range of the loops was reduced to −10 to 10 kOe since the paraffin diamagnetic component became dominant at large fields.

Chapter 3

Theory and analysis protocols

The methodology followed for the analysis of the magnetometry and susceptometry experimental data is presented in this chapter. The theory underlying the interpretation of the experimental data is also discussed in here.

3.1 AC-susceptibility

In order to study the magnetic dynamics of our samples, AC-susceptibility experiments (χ_{ac}) were performed. This technique uses an AC-field to induce a time-varying magnetization in the samples. AC-susceptibility data gave us information about the relaxation time of the magnetization as a function of the temperature and its freezing during the transition to the spin-glass configuration.

We examined the in-phase, χ', and out-of-phase, χ'', parts of the AC-susceptibility as a function of temperature. All of our samples have the typical $\chi_{ac}(T, f)$ features present in superparamagnetic samples and spin-glass-like systems [3]. Namely, at low temperatures, the thermal energy is not enough to overcome the anisotropy energy, resulting in a weak response to the AC drive-field. $\chi'(T,f)$ shows a frequency-dependent maximum at the superparamagnetic blocking temperature, T_B, above which the system has enough thermal energy to undergo 180° rotations of the nanoparticle's magnetization in the measurement time window given by the frequency. At high temperatures, $T > T_B$, the system shows no frequency dependence since each nanoparticle behaves as a free (super)paramagnetic spin. Similarly, $\chi''(T,f)$ has a frequency-dependent maximum near $T_B(f)$, indicating strong energy dissipation in the system when the AC drive field is comparable to the time scale of magnetization reversals. The same temperature and frequency dependence is observed on interacting nanoparticle systems, with the particularity that the magnetic entities can become cluster-like collections of coupled nanoparticles instead. Under these conditions, the magnetization reversals are correlated among particles, and we can no longer speak in terms of individual blocking but collective magnetic freezing below a certain freezing temperature T_f that depends on frequency. Thus, the first step was to identify which relaxation model describes this behaviour appropriately.

To extract the temperature of the $\chi'(T)$ maxima, a polynomial fit of degree five was fit to each cusp (see figure 3.1). This is useful for detecting small temperature variations in the peak for samples that present weak frequency sensitivity or high noise. With this information, we proceeded to test the Néel-Arrhenius law for non-interacting nanoparticle systems,

$$\tau = \frac{1}{f} = \tau_0 \exp\left\{\frac{KV}{k_B T_B}\right\}. \tag{3.1}$$

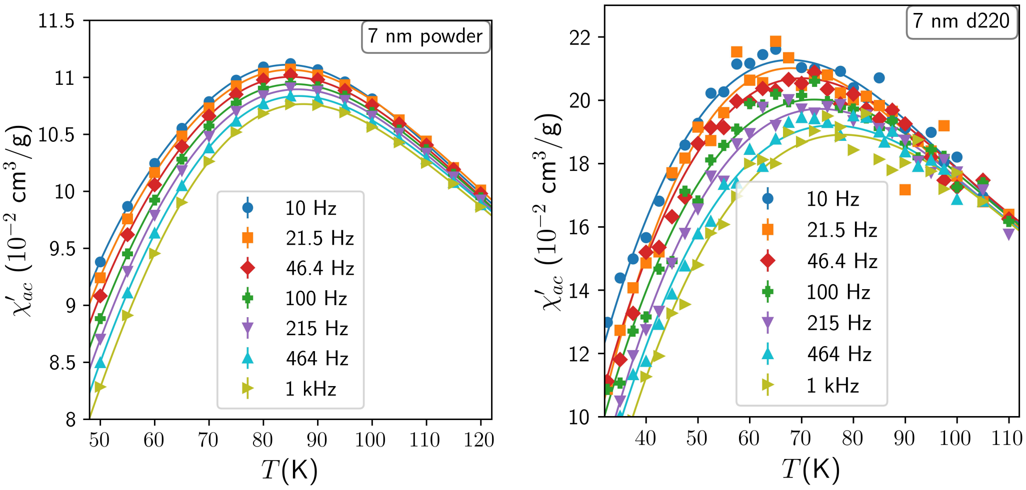

Figure 3.1: $\chi'(T)$ cusps for two of our samples. The solid lines are fits as described in the text.

Here, τ_0 is the attempt time, V and K are the volume and effective anisotropy of the particles, and $k_B = 1.36 \times 10^{-16}$ erg/K is the Boltzmann constant. We find that this equation fails to fit the data properly, and yields unphysically small values of τ_0, specially when magnetic interparticle interactions are present in the system [36]. Since that is the case for all our systems (see figure 3.2), interactions must be taken into account in our work. We can estimate the strength of the interactions by looking at the frequency dependence of T_f of the spin freezing which is often used to compare different classes of spin-glass systems with distinct interacting magnetic entities (magnetic atoms, particles, spin clusters, etc.). Interaction strength can be classed by the Mydosh parameter[54, 55]

$$\delta_f = \frac{\Delta T_f}{T_f \Delta \log_{10}(f)}. \tag{3.2}$$

For strongly interacting magnetic entities, a large frequency change is needed to observe a detectable frequency-dependent peak shift in T_f. As a result, systems

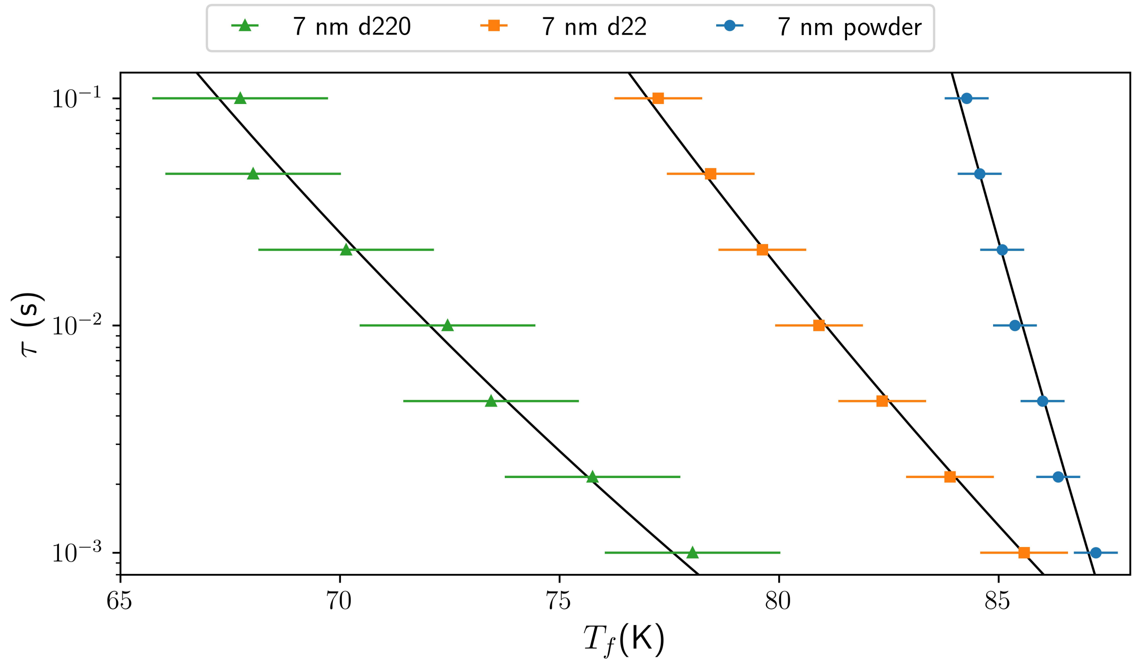

Figure 3.2: Relaxation time, τ, vs T_f for some of our samples. The solid lines are the Néel-Arrhenius fits. The obtained τ_0 values are $\sim 10^{-16}$ s, $\sim 10^{-21}$ s and $\sim 10^{-60}$ s, respectively.

with stronger magnetic interacting entities are less frequency sensitive than those interacting weakly. Using δ_f, changes in the interaction strength were identified between samples, and their values were compared with the literature.

For weak interactions, a description of the frequency dependence of T_F can be obtained using the empirical Vogel-Fulcher law [36, 37]

$$\tau = \frac{1}{f} = \tau_0 \exp\left\{\frac{KV}{k_B\left(T_f - T_0\right)}\right\} \tag{3.3}$$

where T_0 is a phenomenological parameter introduced to the standard Arrhenius law to account for interactions between magnetic entities. Using the Vogel-Fulcher law not only improved the quality of the fit but also gave values of $\tau_0 \sim 10^{-8}$ that are reasonable for the attempt time [56]. The fitted values of K provided an estimation of the effective anisotropy of individual nanoparticles, and T_0 gave an appropriate estimate of the temperature T_g at which the glass transition of the system takes place that marks the onset of glass-like slow dynamics observed at macroscopic timescales in spin-glass systems.

Next, we searched for the standard critical slowing-down characteristic of spin-glasses and spin-glass-like systems that takes place on approaching T_g from high temperatures. According to the dynamic scaling hypothesis [20], the frequency dependence of T_f is described by a power law

$$\tau_c = \tau_* \left|\xi/a\right|^z = \tau_* \left|\frac{T_f - T_g}{T_g}\right|^{-z\nu}, \tag{3.4}$$

where τ_* is the characteristic relaxation time of the nanoparticles, ν is the critical exponent that describes the growth of correlation length ξ, and z is the dynamic exponent that describes the slowing down of the relaxation rate of the system.

Then, we performed a scaling analysis using the real part of the susceptibility $\chi'(T,f)$. The quantity

$$\Delta\chi'(f) = \frac{\chi'(T,f) - \chi_{eq}(T)}{\chi_{eq}(T)} \tag{3.5}$$

measures how the AC-susceptibility deviates from its equilibrium value, $\chi_{eq}(T)$ as we approach T_g. The equilibrium susceptibility, $\chi_{eq}(T)$, is defined as $\chi_{eq}(T) = \chi'\left(T, f \to 0\right)$ and can be obtained from extrapolating to low-temperatures the high temperature $\chi'(T)$ Curie-Weiss-like behaviour [57]. Incidentally, in the low frequency limit, $\chi'(T,f)$ is expected to behave as $\chi'\left(T,f\right) \approx \chi_{ZFC}(T,f)$, where $\chi_{ZFC} = M_{ZFC}/H$ is the low-field susceptibility obtained from M vs T data, and $f = 1/\tau \to$

0 [58].

Using linear response theory, it is possible to derive from equations 3.4 and 3.5 the following scaling relation [21]:

$$\Delta\chi'(f) = \epsilon^{\beta} G(f\epsilon^{-z\nu}), \quad T > T_g. \tag{3.6}$$

where $\epsilon = \dfrac{T_f - T_g}{T_g}$ is the reduced temperature, and $G(f\tau_c)$ is a scaling function with asymptotes

$$\begin{aligned} G(x) &\to x \quad, \quad x \to 0 \\ G(x) &\to x^{\beta/z\nu}, \quad x \to \infty. \end{aligned} \tag{3.7}$$

According to equation 3.6, AC-susceptibility data should collapse to a single curve, G, by choosing appropriate exponents. We successfully employed this technique to our experimental data. In the results chapter, we compared the obtained exponents among our samples and with the ones reported in literature.

3.2 Magnetometry

We started by examining the temperature dependence of the low-field DC-susceptibilities by using zero-field-cooled (ZFC) and field-cooled (FC) measurements. The ZFC configuration consists of cooling the sample in the absence of any applied magnetic field, from 300 to 5 K. By using the ZFC procedure, the random orientation of the nanoparticles' magnetizations present above the nanoparticles' T_B was obtained at 5 K. A DC magnetic field of 50 Oe was then applied, and the magnetization was measured with warming. The increase of the DC-susceptibility, $\chi_{dc}(T) = M_{dc}(T)/H$, takes place when thermal fluctuations allow the nanoparticles' magnetizations to align with the applied field. With further warming, thermal energy becomes sufficient for the nanoparticles to undergo 180° magnetization reversals resulting in a decrease in $\chi_{dc}(T)$. For the FC measurement, the same 50 Oe field was used, and the nanoparticles' magnetizations were measured while cooling from 300 to 5 K. Above T_B the nanoparticles are superparamagnetic and the same response for $\chi_{ZFC}(T)$ and $\chi_{FC}(T)$ is expected. With further cooling, the system's magnetizations remain aligned with the applied field as it freezes, causing a divergence between $\chi_{ZFC}(T)$ and $\chi_{FC}(T)$.

A precise determination of T_B of the nanoparticles from DC-susceptibility is problematic due to the influence of interparticle interactions, particle size distribution, and the use of an applied field which may perturb the spontaneous magnetization reversal. T_B is typically found close to the maximum of $\chi_{ZFC}(T)$ and is related to the onset temperature of $\chi_{dc}(T)$ irreversibilities [27, 59, 29]. For systems where interparticle interactions are present, the magnetic dipolar coupling causes the system's magnetization to freeze and enter a glass-like configuration at $T_g > T_B$. This freezing causes a shift of the $\chi_{ZFC}(T)$ maximum toward higher temperatures that can be linked to the dipolar interaction strength [60, 61, 62]. Additionally, samples prepared with comparable interparticle spacings and measured with the same temperature and field history, a qualitative change in T_B can indicate a change in the overall anisotropy of the nanoparticles.

We started by fitting χ_{dc} with a Curie law, $\chi_{dc} = C/T$, in the high-temperature range where nanoparticles are superparamagnetic. We found that none of the samples could be described as a simple paramagnet and that at least two other parameters were required. The best fits were found with a modified Curie-Weiss expression of the form

$$\chi_{dc} = \frac{C}{T+\theta} + a, \tag{3.8}$$

where θ and a are two constants. These observations lead us to use a more specific model of superparamagnetism that accounts for the spontaneous magnetization of the ferrimagnetic domain of the nanoparticle and the interparticle interactions. Considering the nanoparticles as single-domain ferrimagnets of volume V with a (giant) magnetic moment of $\mu_p = M_S V$, the magnetization should be describe by the Langevin function [63]

$$M(H,T) = M_S\left[\coth(\chi) - \frac{1}{\chi}\right], \quad \text{with} \;\; \chi(H,T) = \frac{M_S \rho V H}{k_B T}, \tag{3.9}$$

where M_S is the spontaneous magnetization, and the magnetic volume $V = \frac{\pi}{6}D^3$ can be obtained from the known particle diameter D. Since we are working with mass normalized magnetization, we have to include ρ as the density of the oxide. For temperatures well above T_g, the low-field (linear) susceptibility reduces to

$$\chi_{dc} = \frac{\rho V}{3k_B}\frac{M_S^2(T)}{T}. \tag{3.10}$$

This equation reduces to a simple Curie law if we assume the spontaneous magnetization constant. This is usually done in nanoparticle systems where the temperature dependence of M_S is negligible (e.g. antiferromagnetic fine particle systems [63]). However, in our case, assuming M_S to be constant leads to inconsistent results. One way to determine the temperature dependence of the spontaneous magnetization of ferrimagnetic nanoparticles is by examining the overall saturation magnetization of an ensemble. At high fields, saturation occurs when the magnetic moments of all particles align with the field, and therefore, an increase in the field intensity cannot increase the magnetization any further. Under those conditions the magnetization of the system (collective) is reflective of the saturation magnetization of individual nanoparticles.

We also measured the magnetization as a function of the applied field (M vs. H) at selected temperatures. The saturation magnetization, M_S, was extracted from the high-field data using the empirical law of approach to saturation [64]

$$M = M_S(T)(1 - b/H^2) + \chi_{hf}H, \tag{3.11}$$

where $M_S(T)$ is the saturation magnetization, and b is a phenomenological constant. χ_{hf} is the high-field linear component of the DC-susceptibility. The obtained $M_S(T)$ data was fitted to the Bloch T^α law for spin-wave excitations

$$M_s\left(T\right) = M_0\left(1 - bT^\alpha\right), \tag{3.12}$$

where α is equal to $3/2$ in the bulk, b is the Bloch constant, and M_0 is the magnetization extrapolated to zero temperature.

Hysteresis curves were observed below certain temperatures, which are also indicative of blocked/frozen configurations. The coercivity, H_C, was extracted as the value of the field that makes $M = 0$. Using the values of H_C and M_S, another estimation of the anisotropy was found with equation [28]

$$H_C = \frac{2K}{\rho M_S}[1 - (T/T_B)^{1/2}], \qquad \text{for} \;\; T < T_{B,H_C} \tag{3.13}$$

for uniaxial non-interacting particles, where T_{B,H_C} is the blocking temperature defined as the onset of the hysteresis, $H_C(T) > 0$.

Using the previously calculated $M_S \propto (1 - bT^{\alpha})$ we can examine the inverse DC-susceptibility, modulated by $M_S^2(T)$, versus temperature

$$\frac{(1 - bT^{\alpha})^2}{\chi_{dc}} = \frac{T}{C}, \qquad \text{with} \qquad C = \frac{M_0^2 \rho V}{3k_B} \tag{3.14}$$

and perform a linear fit at high temperatures. This fit has $1/C$ as slope, which allows us to compare the fitted C values with those calculated using equation 3.14.

It is important to point out that the Langevin behaviour given by equation 3.14 was obtained by assuming non-interacting and isotropic nanoparticles. Deviations from equation 3.14 are expected in real systems with non-zero interparticle interactions and anisotropy. For systems with strong magnetic interactions between particles, a larger value of the C from equation 3.14 can indicate that the magnetic entities are not single particles but clusters of strongly correlated particles of higher magnetic moment $\mu_c \approx \eta M_S V > M_S V$, with $\eta > 1$. The intercept of equation 3.14 (linear fit) can also be influenced by interparticle interactions. A $T \neq 0$ intercept can be understood in terms of an equivalent Curie-Weiss law of the form

$$\chi_{dc} = \frac{\eta \rho V}{3k_B} \frac{M_S^2(T)}{(T + T^*)} \tag{3.15}$$

with the inclusion of an interaction ordering temperature T^* that can be attributed to the effects of interactions. Thus, we have a static counterpart to the Vogel-Fulcher T_0 observed in dynamic effects, equation 3.3. T^* is expected to increase with the magnetic interaction strength of the nanoparticles [39, 65, 66]. Also, T^* can be obtained from the Landau free energy expansion as seen in section 1.2.4. However, this approach cannot predict a magnitude for T^*. A detailed microscopic approach is required to obtain a T^* magnitude [39].

Anisotropy also causes deviation from the Langevin behaviour [63, 30]. A simple analogy with atomic paramagnetism helps to understand this. As seen in section 1.1.1 when discussing paramagnetism, a system composed of magnetic moments that can access an infinite (continuous) number of sates (classical limit) is described by $M \sim (\coth(\chi) - 1/\chi)$, but when the magnetic moments are restricted to only two states, then $M \sim \tanh(\chi)$. This two behaviours of the magnetization result in expressions for the low-field paramagnetic susceptibility that differ by a factor of three. If we assume that our nanoparticles, due to high anisotropy, have their magnetic states restricted to some spatial directions, then deviations from $M = M_S \left[\coth(\chi) - 1/\chi\right]$ are expected. As a result, if the low-field susceptibility of said particles is fitted with equation 3.15, a factor $\eta > 1$ is expected (for a system that behaves as $M = M_S \tanh(\chi)$, $\eta = 3$).

Both η and T^* can be found with the aforementioned fit and are expected to increase with the strength of interparticle magnetic interactions and anisotropy.

3.3 Static scaling analysis

To study the nature of the freezing phenomenon that takes place when we approach T_g from high temperatures, scaling analysis was performed using the temperature and field dependencies of the magnetization. To do so, we used the Widom-Kadanoff scaling relation for phase transitions discussed in section 1.1.6

$$M(h) = |\epsilon|^{\beta} f\left(\frac{h}{\epsilon^{\gamma+\beta}}\right), \tag{3.16}$$

where M is the magnetization, h is the effective field, and $\epsilon = \frac{T - T_c}{T_c}$ is the reduced temperature around the critical point of a second order magnetic transitions. β and γ are two critical exponents that corresponds to

$$M = |\epsilon|^{\beta}, \qquad \text{and} \qquad \chi = \frac{dM}{dh} = |\epsilon|^{-\gamma} \tag{3.17}$$

when $h \to 0$.

The spin-glass transition does not present the divergence of the DC-susceptibility observed in the ferromagnetic-paramagnetic phase transition. Instead, the spin-glass DC-susceptibility presents a sharp maxima at the glass transition temperature T_g. This behaviour is usually attributed to a divergence of the non-linear part of the susceptibility, χ_{nl}, at T_g. Therefore, testing the critical behaviour of spin-glasses requires first extracting the non-linear part of the susceptibility, defined as

$$\chi_{nl} = \chi_0 - \frac{M\left(H, T\right)}{H}, \tag{3.18}$$

and then finding the critical exponents that govern its divergence. Suzuki and Chalupa [18, 17] derived an scaling expression for the paramagnetic-spin-glass transitions,

$$R(h^2) = 1 - \frac{M}{\chi_0 h} = |\epsilon|^{\beta'} f\left(\frac{h^2}{\epsilon^{\gamma+\beta'}}\right), \tag{3.19}$$

where the order parameter is not M but R (related to the non-linear part of the susceptibility), and h^2 plays the role of the field.

For the non-linear DC-susceptibility of nanoparticle systems a similar expression to equation 3.19 can be found using the Langevin model of the magnetization [67].

The Langevin function in equation 3.9 can be expanded as a power series.

$$\frac{M}{M_S} = \sum_{n=0}^{\infty} a_{2n+1} L_{2n+1} x^{2n+1} \tag{3.20}$$

which results in

$$R(H^2) = 1 - \frac{M}{\chi_0 H} = \frac{1}{15} a_3 x^2 - \frac{2}{305} a_5 x^4 ... \tag{3.21}$$

where $\chi_0\,(T)$ is the low-field susceptibility and $L_1 = \frac{1}{3}$, $L_3 = -\frac{1}{45}$, $L_5 = \frac{2}{915}$,...,L_{2n+1} are the numerical coefficients of the series expansion of the Langevin function. For non-interacting isotropic systems the expression for $\chi_0\,(T)$ and $\chi\,(T,H)$ are given by equation 3.10 and equation 3.9 respectively. But for magnetically coupled clusters with moment $\mu_c = \eta M_S V > M_S V$ or for systems with large anisotropy, the susceptibilities are better described by

$$\chi_0\,(T) = \frac{\eta\rho V}{3k_B} \frac{M_S^2\,(T)}{(T + T^*)} \qquad \text{and} \qquad \chi\,(T,H) = \frac{\eta\rho V}{k_B} \frac{M_S\,(T)}{(T + T^*)} H \tag{3.22}$$

for which η and $T*$ can be found by carefully fitting the low-field susceptibilities.

For spin-glasses, the coefficients $a_3(T)$, $a_5(T)$ ... $a_{2n+1}(T)$ are all equal to one on the high temperature limit, and are expected to diverge at T_g as

$$a_3(T) \sim \left(\frac{T - T_g}{T_g}\right)^{-\gamma}, \quad a_5(T) \sim \left(\frac{T - T_g}{T_g}\right)^{-(2\gamma+\beta')}, ... \tag{3.23}$$

Equation 3.23 is only valid in the vicinity of T_g, and therefore a very precise determination of T_g and high-resolution data are required to extract the exponents. Since our data is mostly in the range of $1.2T_g < T < 2T_g$, (see chapter 4), we must find a way to extend the validity of equation 3.23 to higher temperatures. Omari et al. [67] suggested working with the high-temperature behaviour of $a_3(T)$ instead of its divergence at T_g. In the high-temperature limit $T >> T_g$, the asymptotic behaviour of $a_3(T)$ can be expanded as

$$a_3(T) \sim \left(1 + \gamma' \frac{T_g}{T} - ...\right) \approx \left(1 - \gamma' \frac{T_g}{T}.\right)^{-1} = \left(\frac{T - T_g}{T}\right)^{-\gamma'} \tag{3.24}$$

Where γ' is just the first coefficient of the expansion. This expression for $a_3(T)$ becomes constant at high temperatures and for $\gamma' = \gamma$ recovers its divergence at T_g, i.e.

$$\left(\frac{T}{T - T_g}\right)^{\gamma} \sim \left(\frac{T_g}{T - T_g}\right)^{\gamma} + \mathcal{O}\left(\frac{T_g}{T - T_g}\right)^{\gamma - 1}, \quad \text{as} \quad T \to T_g \tag{3.25}$$

Therefore, changing the definition of the reduced temperature from the usual $\dfrac{T - T_g}{T_g}$ to the non-lineal $\epsilon = \dfrac{T - T_g}{T}$ allows us to extend the validity of the scaling arguments to a wide temperature range far away from the critical point. Equation 3.21 can be written as

$$R(H^2) = 1 - \frac{M}{\chi_0 H} = -\sum_{n=1}^{\infty} \frac{L_{2n+1}}{L_1} \frac{1}{\epsilon^{\gamma_{2n+1}}} \left(\frac{\eta \rho V}{k_B} \frac{M_S(T)}{(T + T^*)} H\right)^{2n}. \tag{3.26}$$

Then, using the scaling argument of Chalupa and Suzuki, equation 3.19, leads to

$$\frac{R}{\epsilon^{\beta'}} = \left(1 - \frac{M}{\chi_0 H}\right)\left(\frac{T}{T - T_g}\right)^{\beta'} \sim f\left[\left(\frac{\eta \rho V}{k_B} \frac{M_S(T)}{(T + T^*)} H\right)^2 \left(\frac{T}{T - T_g}\right)^{(\gamma + \beta')}\right] \tag{3.27}$$

for $T \to T_g$, where $f(x) = \alpha_1 x + \alpha_2 x^2 + \ldots$ is a scaling function. Our data was plotted as equation 3.27 suggests, and the exponents that collapse the data to a single curve were extracted.

Chapter 4

Intraparticle magnetism: Cobalt-doped magnetoferritin

In this section we explore the nanomagnetism of artificial magnetoferritin nanoparticles doped with different amounts of cobalt. Ferritin is a protein present in almost all living organism whose function is to store and release iron. Using biomimetic mineralization, it is possible to synthesize iron oxide nanoparticles inside the cavity of an empty ferritin cage (apoferritin). The resulting nanoparticles, known as magnetoferritin, are composed of the ferritin shell that has a fixed external diameter of about 12 nm and an internal diameter of about 8 nm, and the magnetic core.

For this study, the ferritn shell fulfills two main roles: it acts as a way to control the particle size dispersion and to reduce the strength of interparticle interactions by granting equal spacing between the magnetic cores. Under these conditions of monodispersity and controlled interparticle spacing, the anisotropy was changed by substituting cobalt into the iron oxide structure, granting us a collection of weakly interacting nanoparticle systems in which the effects of the anisotropy on the magnetization can be studied.

Here, all the magnetometry and susceptometry data were normalized to the total mass of the oxide component of the ferritin nanoparticles [1]. Mass normalization of the magnetic data was chosen over the standard volume normalization to avoid the uncertainties that arise from assuming the density of nanoparticles and from estimations of the sample magnetic volume.

4.1 Composition, structure, and morphology

The morphology and crystal structure of the five cobalt-doped magnetoferritin samples (0%, 3%, 7%, 10%, 12%) were analyzed in previous work [1]. Briefly, they consist of a ferrimagnetic core of Fe/Co oxide surrounded by an organic protein shell. The particles have spherical morphology with a very narrow size distribution of (6.5 ± 0.5) nm diameter (see figure 4.1). The analysis of the Mössbauer spectra showed a core composition of γ-$Fe_2O_3/Co_xFe_{3-x}O_4$ with $x = 0, 0.25, 0.51, 0.56,$ and 0.63 for the samples containing 0%, 3%, 7%, 10%, and 12% Co, respectively. Also, the oxide-to-sample mass ratio was obtained from the Mössbauer spectra as $m_{oxide}/m_{sample} \approx 7/20$ and was used to normalize the susceptometry and magnetometry data [1].

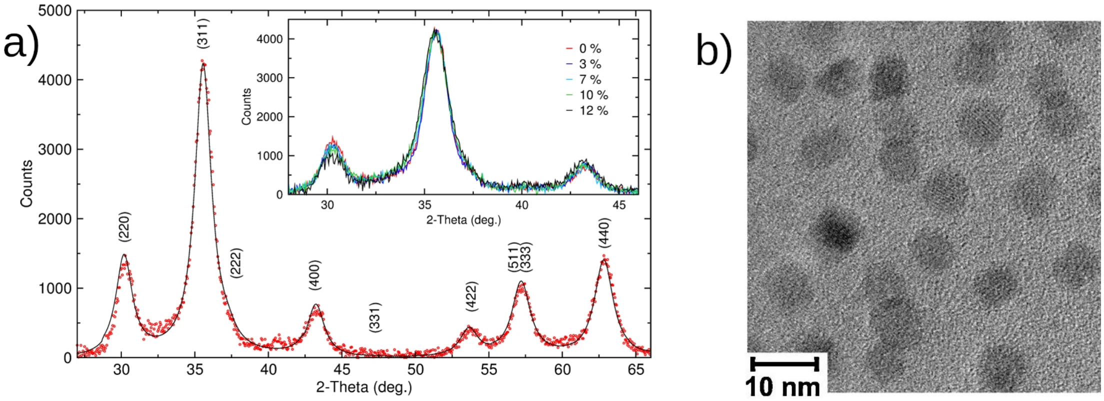

Figure 4.1: a) X-ray diffraction pattern for undoped (0%) Fe-oxide sample, with the solid line indicating the result of the Rietveld refinement. The inset is a selected 2θ range of the pattern for all samples. b) TEM image of the undoped MF sample dispersed and deposited on a grid. Figures taken from [1]

4.2 AC-susceptibility; dynamic magnetic properties

Figures 4.2 and 4.3 show the temperature dependence of the real part (in-phase) χ' and the imaginary part (out-of-phase) χ'' of the magnetic AC-susceptibility of all the nanoparticle samples. The measurements were from 10 K to 350 K when warming in a zero DC field, with an AC drive field of 2.5 Oe at specific frequencies spanning from 10 Hz to 1 kHz. Both χ' and χ'' exhibit frequency-dependent maxima characteristic of superparamagnetic nanoparticles, whose magnetic configurations block below a blocking temperature T_B. This behaviour is also observed in interacting nanoparticle systems, with the difference that instead of individual particle blocking, the nanoparticle magnetizations freeze collectively below a freezing temperature T_f.

We fit the frequency dependency of T_f with the Néel-Arrhenius law, equation 3.1, $\tau = \tau_0 \exp\left\{\frac{KV}{k_B T_f}\right\}$. This equation fails to fit the data properly and gives values of the

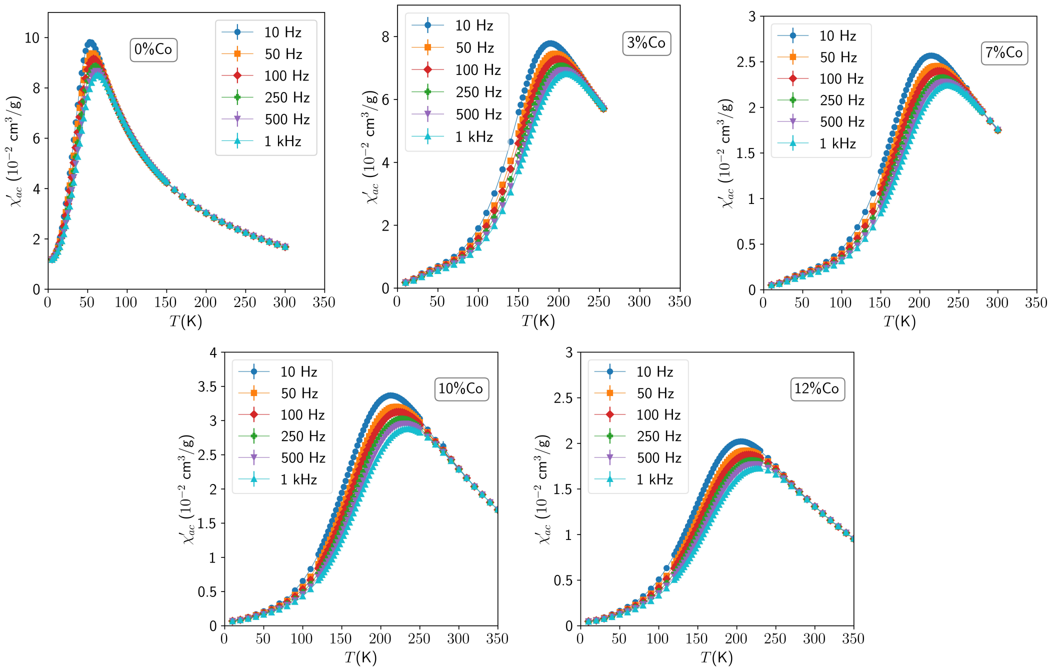

Figure 4.2: In-phase AC-susceptibility for undoped and cobalt-doped magnetoferritin nanoparticles.

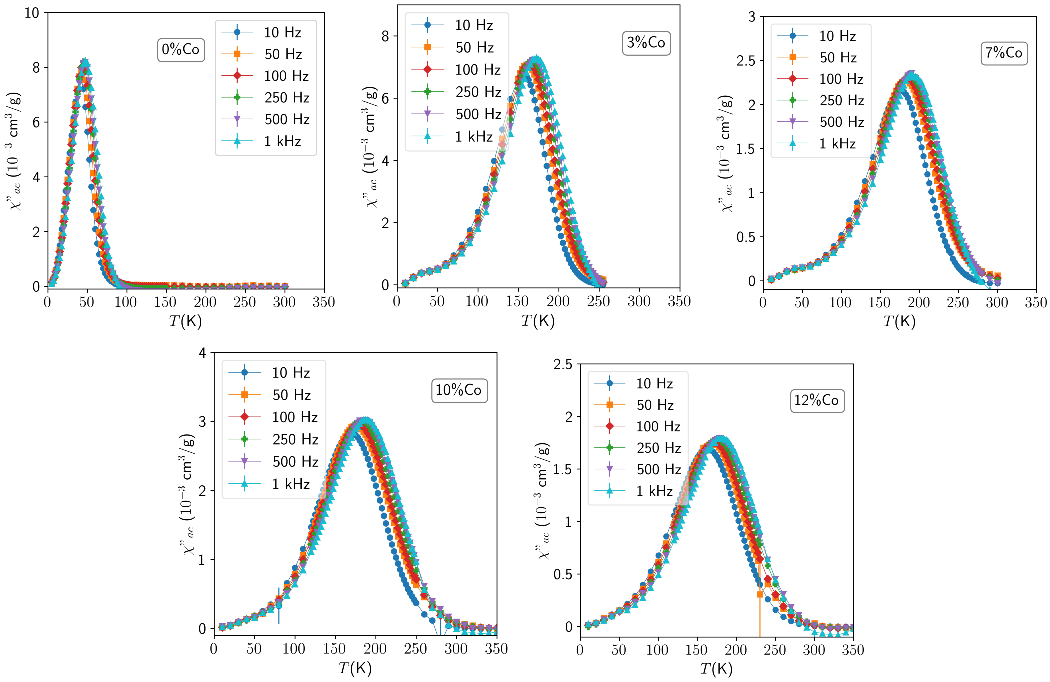

Figure 4.3: Out-of-phase AC-susceptibility for undoped and cobalt-doped magnetoferritin nanoparticles.

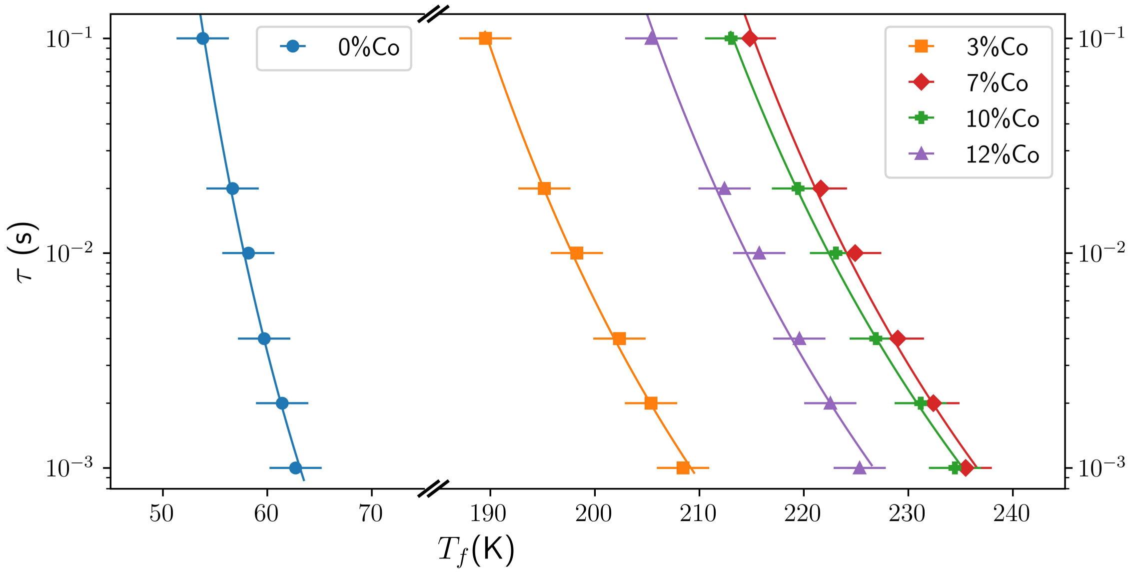

Figure 4.4: Frequency dependence of the freezing temperature (T_f). The solid lines are fits as described in the text. For each sample, the Vogel-Fulcher and the dynamic slowing down fits coincide in the measured frequency range.

relaxation time that range from 10^{-16} to 10^{-25} s, which are unphysically small. This result, in concordance with further analysis (see figure 4.4), shows that interparticle interactions are present and the system exhibits collective magnetic freezing instead of individual superparamagnetic blocking.

The frequency sensitivity of the spin freezing was analyzed using the Mydosh parameter, equation 3.2. The Mydosh parameter, δ_f, gives a way to qualitatively compare the strength of the interparticle interactions. Our calculated values are shown in figure 4.5.a. They are all in the value range of spin clusters like Fe-Al_2O_3, which suggests that weak interparticle interactions are present [55]. The values decrease with the cobalt addition.

A description of the frequency dependence of T_f for interacting systems was ob-

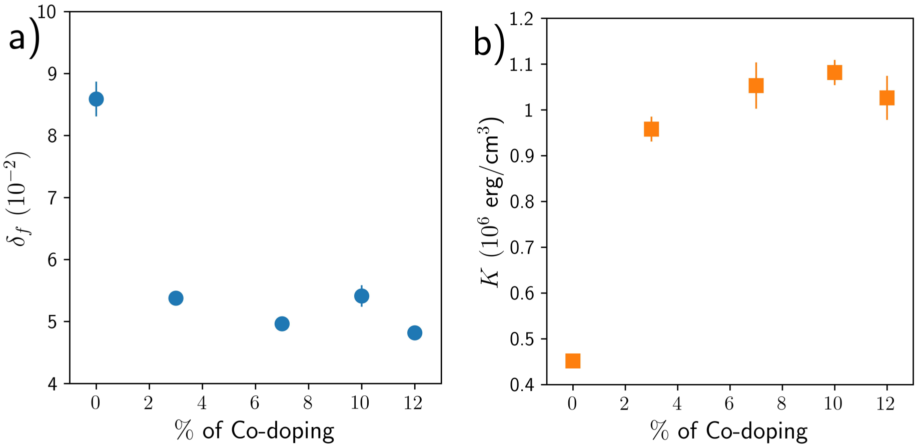

Figure 4.5: a) Mydosh parameter (δ_f) as a function of the cobalt content. b) Average magnetic anisotropy K.

Table 4.1: Critical parameters obtained by fitting the frequency dependence of T_f with equation 3.4.

Co-doping	T_0 (K)	τ_0 (s)	$z\nu$
0%	31 ± 1	$(9 \pm 5) \times 10^{-9}$	13.9 ± 0.3
3%	141 ± 2	$(9 \pm 3) \times 10^{-9}$	13.9 ± 0.2
7%	161 ± 3	$(8 \pm 4) \times 10^{-9}$	14.0 ± 0.2
10%	158 ± 2	$(9 \pm 3) \times 10^{-9}$	13.8 ± 0.2
12%	153 ± 4	$(8 \pm 5) \times 10^{-9}$	14.0 ± 0.2

tained using the empirical Vogel-Fulcher law, $\tau = \tau_0 \exp\left\{\frac{KV}{k_B\left(T_f - T_0\right)}\right\}$. The fit gives us a first estimate of the anisotropy, K, of the system, which increases with the cobalt dopant concentration and has a maxima at 10% Co (see figure 4.5). The increase in anisotropy is not proportional to the Co^{2+} content but has a sharp increase from the pure sample and then becomes essentially constant with the further substitution of Co^{2+}. The fitted value of T_0 also gives an estimate of the glass transition temperature of the system ($T_g \approx T_0$) see (table 4.1), which marks the onset of glass-like slow dynamics (also observed in DC measurements as discussed below).

The critical slowing-down on approaching T_g from high temperatures was studied next. The frequency dependence of the freezing temperature was fitted with the power law given by $\tau_c = \tau_* \left|\frac{T_f - T_g}{T_g}\right|^{-z\nu}$. The obtained critical exponents are shown also in table 4.1. All systems show similar exponents $z\nu \approx 14$. Similar expoents have been reported in the literature for iron oxide nanoparticles (e.g. $z\nu = 11$ for 15 nm hollow γ-Fe_2O_3 particles [68])

To further study the critical behaviour, dynamic scaling was performed. Figure 4.6 presents the results of applying the scaling relation, $\Delta\chi'(f) = \epsilon^\beta G(f\epsilon^{-z\nu})$, to each sample in the temperature range of $T_g < T < 2T_g$. The best collapse of the data points to a single line $G(f\tau_c)$ is obtained with the set of exponents shown in figure 4.7. The critical exponents (β and $z\nu$) are very sensitive to the selection of T_g. But when we use the $T_g \approx T_0$ values obtained previously from the Vogel-Fulcher analysis (table 4.1), β and $z\nu$ can be established uniquely.

4.3 Magnetization and DC-susceptibility; Static magnetic properties

For each sample, magnetization versus temperature was measured at 50 Oe over the 5 to 350 K temperature range. Figure 4.8 shows the FC and ZFC magnetic DC-susceptibility. The ZFC protocol consists of cooling the sample in the absence of an external field and then applying a field and measuring the magnetization while heating. For FC, a field is applied at the maximum temperature, and the measurements are done while cooling. Since magnetic irreversibility depends on the magnetic history of the material, the bifurcation of FC and ZFC magnetizations below a certain temperature marks the onset of blocked configurations in superparamagnetic samples [3].

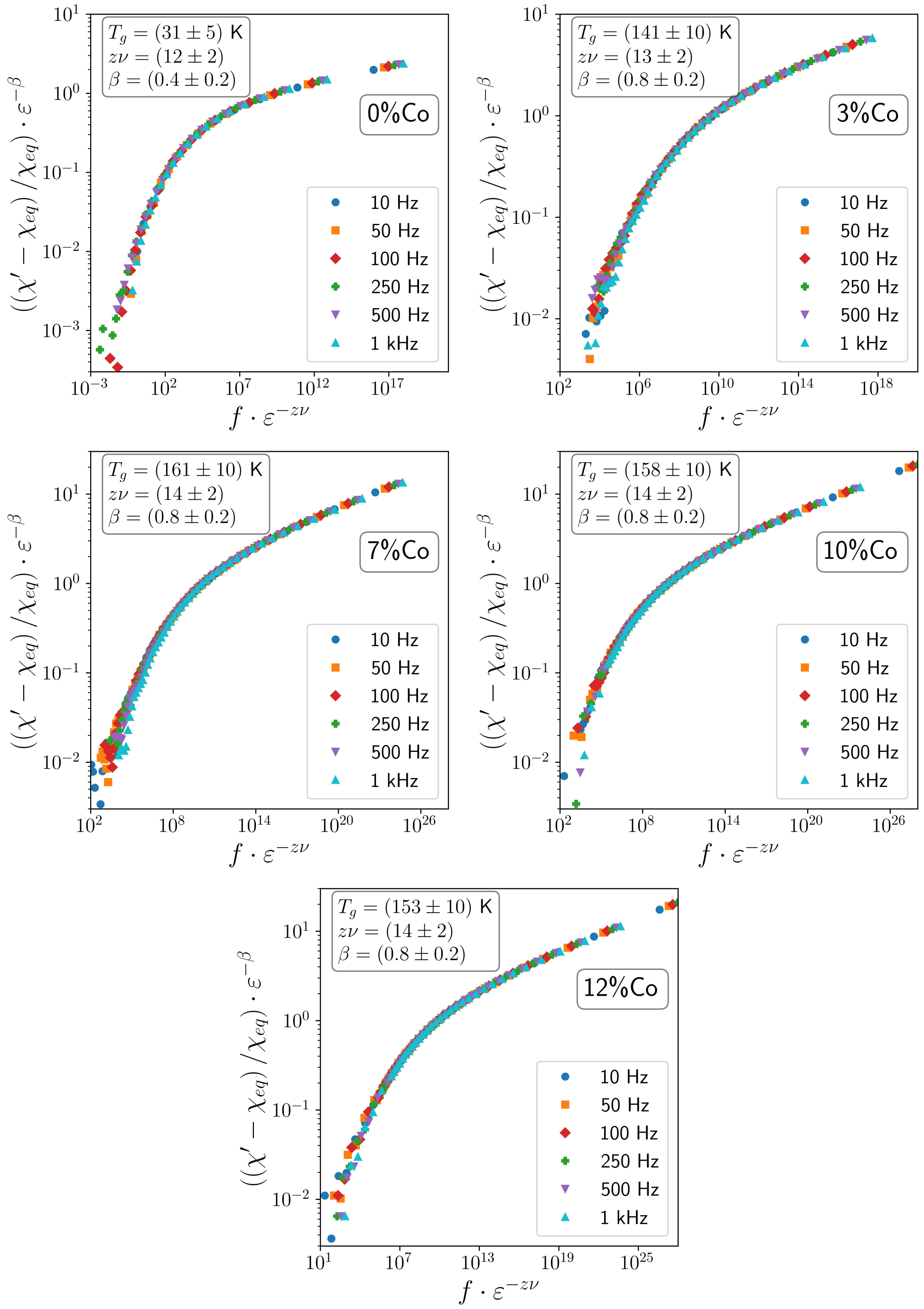

Figure 4.6: Rescaled AC-susceptibility data of the magnetoferritin samples of different cobalt dopant concentration. $\chi'(T, f)$ collapses onto a single curve when appropriate scaling exponents, β and $z\nu$, are chosen.

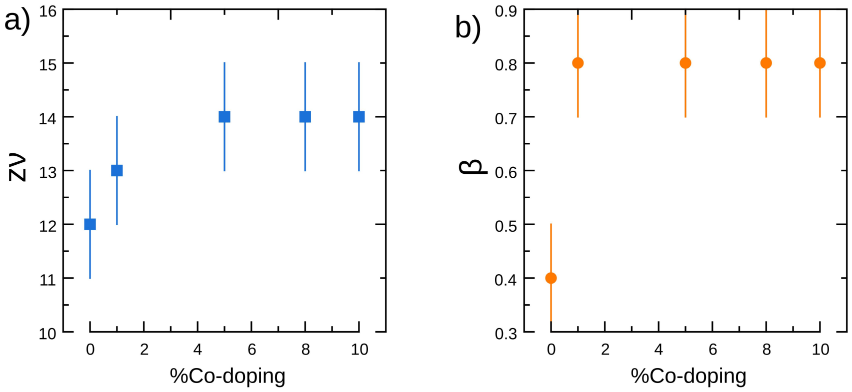

Figure 4.7: Critical exponents as a function of the dopant concentration obtained from the scaling analysis as described in the text.

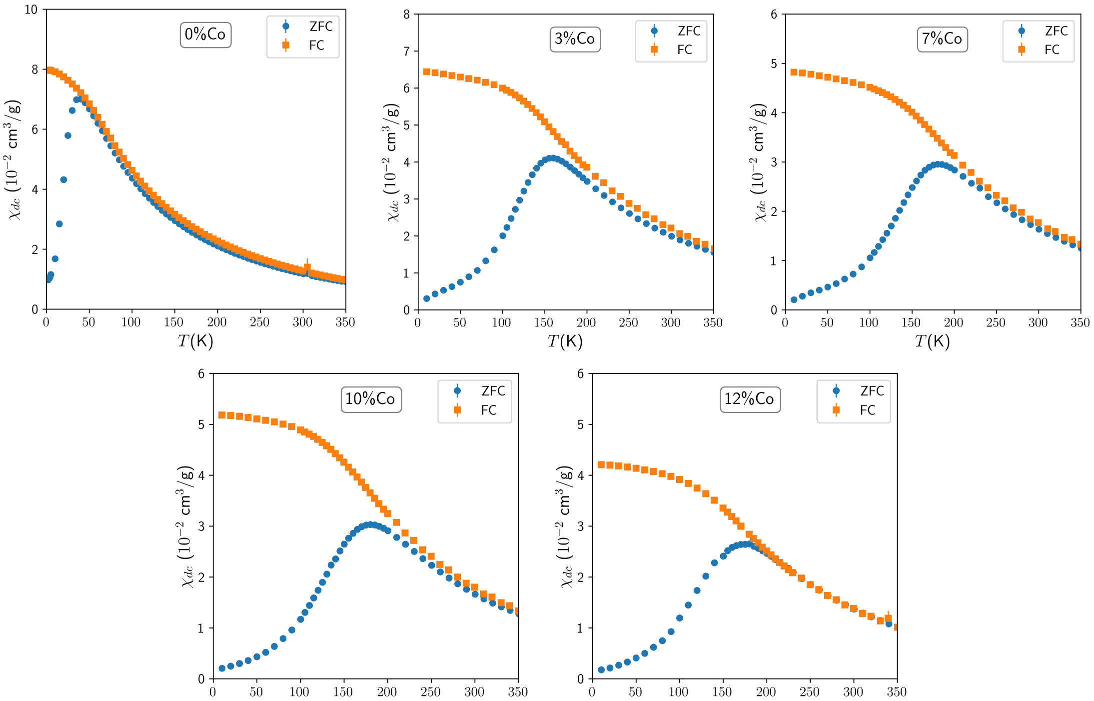

Figure 4.8: Low field ZFC and FC magnetization vs temperature for the magnetoferritin samples

An inspection of figure 4.8 reveals that the doped samples exhibit larger blocking temperatures in agreement with χ_{ac} results.

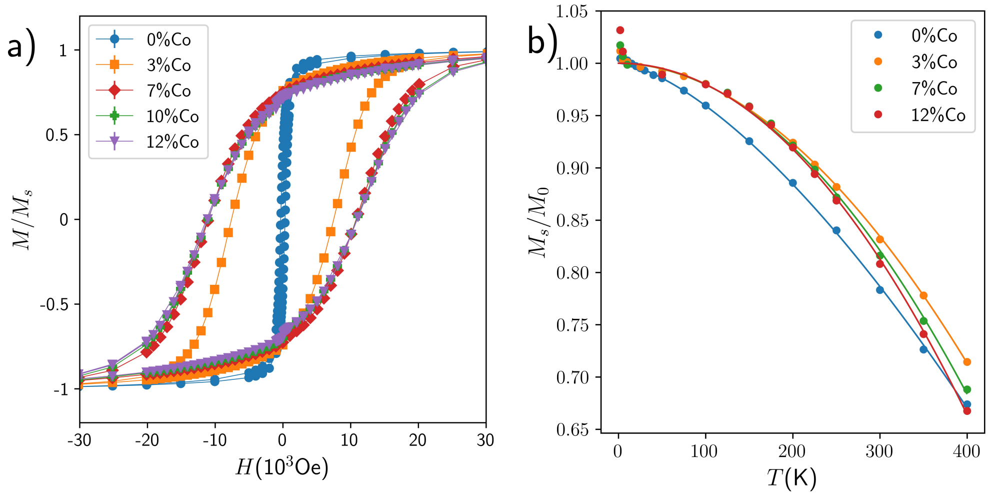

Figure 4.9: a) Hysteresis loops at 2 K for different dopant concentrations. b) Spontaneous magnetization and Bloch T^α fit. The obtained Bloch constants b are consistent with Fe-oxide nanoparticles [2]. For clarity, the data was normalized to $T = 0$ K saturation

Magnetization versus applied field (M vs H) was measured at selected temperatures across the 5 to 350 K range. The measurement range spans from relatively small fields (50 Oe), useful to study the linear part of the susceptibility, to high fields (50 kOe) used to determine the magnetic saturation of the ensembles. The saturation magnetization, M_S, was obtained using the empirical law of approach to saturation (equation 3.11). The high-field linear susceptibility, χ_{hf}, arises from the diamagnetic protein cell and the paramagnetic clusters of ions within the ferritin shell that behave like paramagnets as discussed in [1]. The fitted values of $\chi_{hf} \approx 10^{-6}$ emu/Oe and their temperature dependence are negligible for all samples. The obtained $M_S(T)$ data was fitted to the Bloch T^α law for spin-wave excitations, $M_s(T) = M_0(1 - bT^\alpha)$ as shown in figure 4.9.b. The results are in table 4.2.

For the undoped particles, $M_S(T)$ was well described by the normal Bloch law ($\alpha = 3/2$), and for the doped samples, the effective exponent was close to $\alpha = 2$.

Table 4.2: Parameters obtained by fitting the data with Bloch T^{α}, equation 3.12.

Co-doping	M_0 (emu/g$_{oxide}$)	b (10^{-6}K$^{-\alpha}$)	α
0%	72 ± 3	47 ± 6	1.47 ± 0.02
3%	69 ± 3	1.8 ± 0.4	2.00 ± 0.04
7%	63 ± 3	2 ± 1	1.99 ± 0.08
12%	60 ± 3	2 ± 1	2.0 ± 0.1

This increase of the effective exponent with the cobalt addition was interpreted as caused by an increase in crystalline anisotropy, (further discussion in chapter 7). For the undoped particles the Bloch constant, $b = 4 \times 10^{-5}$ K$^{-3/2}$, is consistent with Fe-oxide nanoparticles [69]. The Co-doped samples provided $b \approx 2 \times 10^{-6}$ K^{2}, consistent with a cobalt-ferrite composition [70].

M vs H hysteresis loops were observed at temperatures below blocked temperatures ($T_{B,HC} \approx T_g$) as expected. Figure 4.9.a shows representative loops at 2 K for all dopings, evidencing an increase of coercivity (H_C) with Co concentration that does not scale with the increase on T_g. The anisotropy K was also estimated using the dependencies of H_C and M_S with temperature (equation 3.13). This equation was derived for uniaxial non-interacting particles but gives a nice fit up to $\sim T_{B,H_c}/2$ even though interparticle interactions were identified from the dynamic analysis.

The next step is to analyze the data in the high-temperature (superparamagnetic) region. We examine the inverse low-field susceptibility according to equation 3.14 and fit it with a linear function as shown in figure 4.11. The low field susceptibility was well described by equation 3.15, $\chi_{dc} = \frac{\eta \rho V}{3k_B} \frac{M_S^2(T)}{(T + T^*)}$, and the parameter η, which speaks of agglomeration of correlated particles, and the Weiss-like ordering temperature T^* were extracted as shown in table 4.3. There is an increase of both parameters with the cobalt doping that could indicate an increase in the magnetic interactions between particles. However, since the size and spacing between particles did not change with

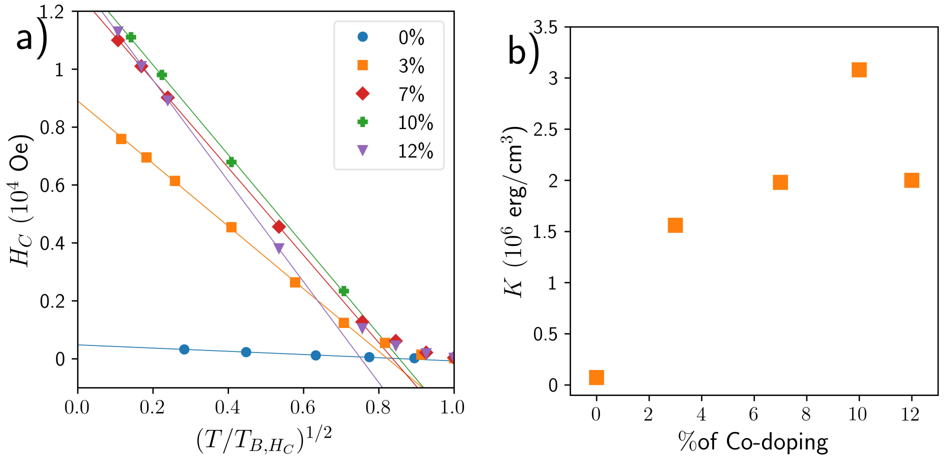

Figure 4.10: a) Temperature dependence of the coercivity of the different doped nanoparticles. b) Anisotropy K as a function of the cobalt content.

Table 4.3: Parameters obtained by fitting the data with a modified Curie-Weiss law (equation 3.15).

Samples	η	T^* (K)
0%	3.0 ± 0.3	4 ± 6
3%	4.8 ± 0.6	55 ± 2
7%	5.0 ± 0.6	71 ± 4
12%	4.2 ± 0.7	59 ± 9

the cobalt addition, and since the cobalt doping decreased the magnetization, this increase of parameters has to be caused by the anisotropy.

For higher fields, a Langevin behaviour is expected (equation 3.9). Figure 4.12 shows the behaviour of the left side of equation 3.21 as a function of $M_S H/T$. Well above T_g, the isotherms show a quadratic behaviour as expected from a magnetization that can be expanded in odd powers of field. But, this H/T range shrinks on lowering the temperature close to T_g. Due to a lack of H resolution at small fields we cannot really identify the curvature of the isotherms when $H \to 0$ and $T \to T_g$, but if equation 3.21 holds, in the limit of $H \to 0$, all $T > T_g$ isotherms should approach the

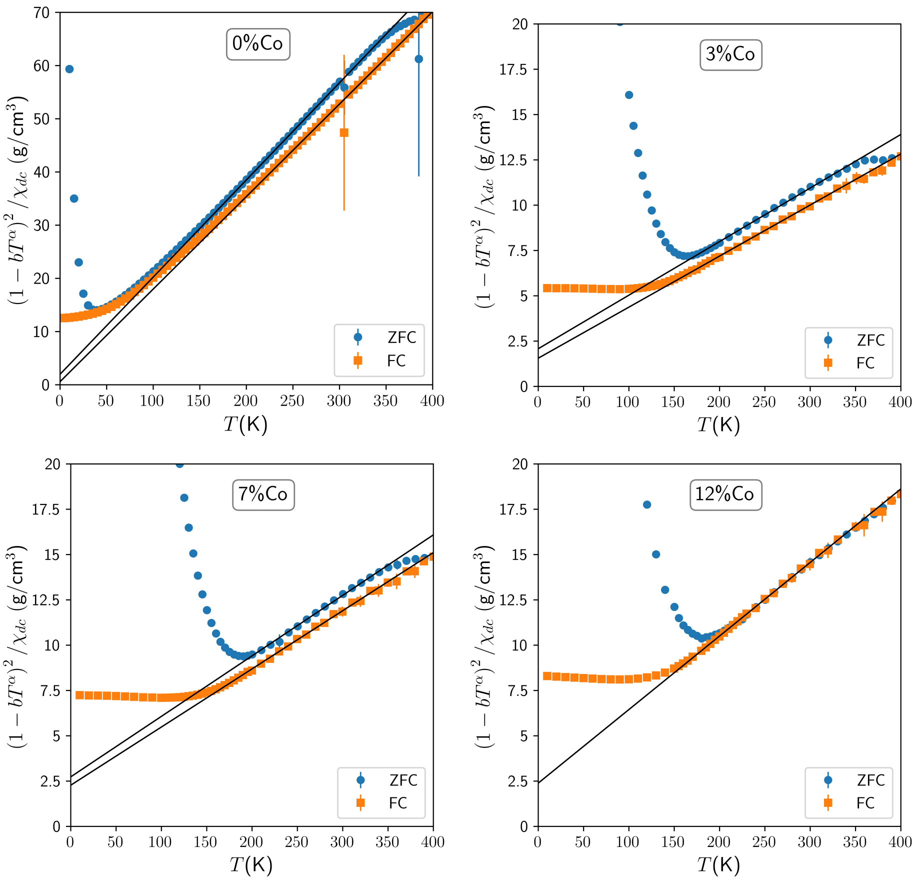

Figure 4.11: The low field inverse susceptibility vs. temperature. The black lines are linear fits at high temperatures.

value of 1, since at that limit, $\chi_{nl} = \chi_0$. From this initial slope the coefficient $a_3(T)$ and γ could be quantitatively determined [67].

The scaling analysis was performed. The low-field (linear) susceptibility was taken as the fit to equation 3.15. Then the data was plotted according to equation 3.27. The critical exponents β' and γ were adjusted until the collapse of the data to a single function was seen. As shown in figure 4.13, our data collapses to a single curve for $T_g = 31\ K$. The exponents β' and γ are dependent on the T_g used. However, if we set the values of $T_g = T_0$ as the one that was found in the dynamic scaling, then the resulting critical exponents are $\gamma = (4.0 \pm 0.5)$ and $\beta' = (0.4 \pm 0.1)$. And

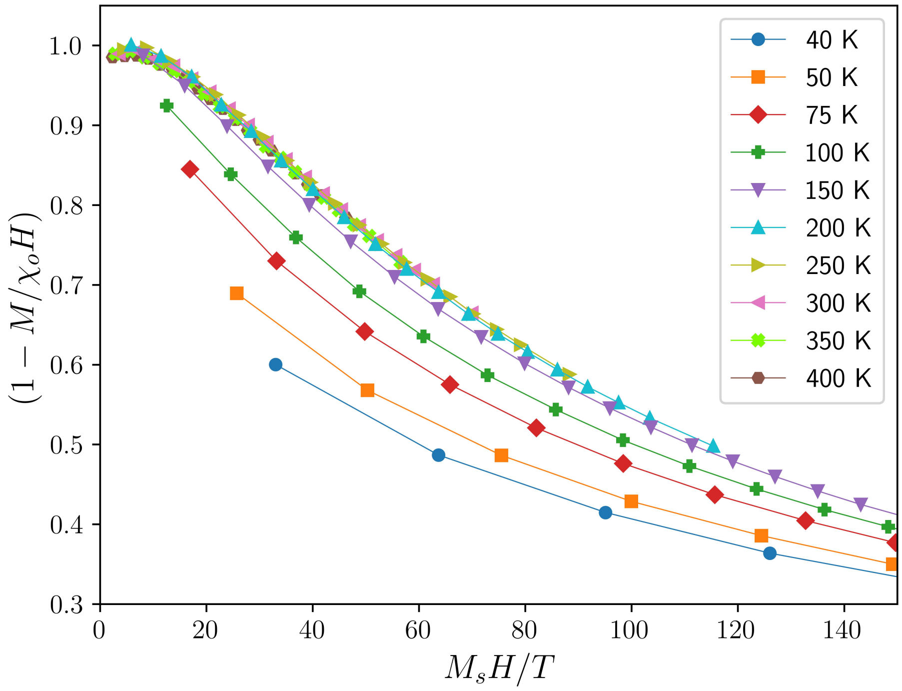

Figure 4.12: Non-linear part of the susceptibility vs. $M_S H/T$ for the 0% sample. Notice how the data starts from one in the limit of small H/T and the initial curvature changes as T gets close to, ($T_g \approx 31\ K$), as described in the text.

since the exponents extracted from the dynamic and static scaling agree ($\beta = \beta'$), we can use the hyperscaling relations $\alpha = 2 - 2\beta - \gamma$, $\nu = (2 - \alpha)/d$ and $\delta = (\gamma + \beta)/\beta$ to determine other exponents as well, $\alpha = -2.8 \pm 0.7$, $\nu = 1.4 \pm 0.3$, $\delta = 11 \pm 4$, and $z = 8.6 \pm 0.8$. Similar exponents were found in 3D Ising spin-glasses (e.g. $Fe_{0.5}Mn_{0.5}TiO_3$ [16]).

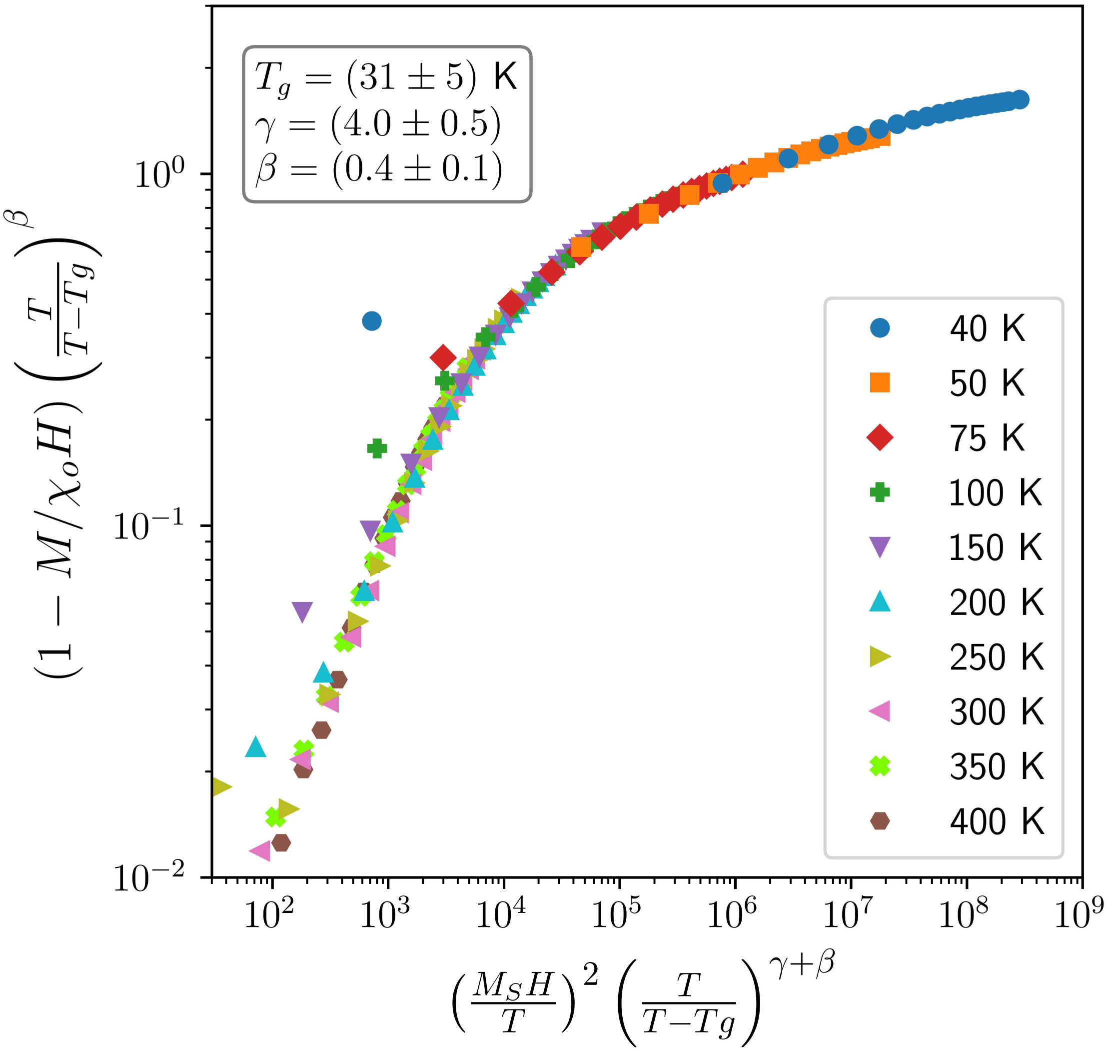

Figure 4.13: Rescaled AC-susceptibility data of the pure magnetoferritin sample in the temperature range of 1.3 $T_g < T < 10\ T_g$ and field range of 100 Oe $< H <$ 1 kOe. $M(H,T)$ collapses onto a single curve when appropriate scaling exponents, β and $z\nu$, are chosen.

Chapter 5

Interparticle interactions: Magnetite (Fe_3O_4) spheres of different sizes

While diluted nanoparticle systems show magnetic properties that can be described as the sum of individual particle contributions, we expect that sufficiently concentrated assemblies of nanoparticles may exhibit a distinct collective behaviour (e.g. glass phase). To explore collective behaviour, we turn to magnetite nanoparticles. Magnetite has some advantages; the thermal decomposition synthesis gives control over size and morphology, granting narrow size distributions and high magnetization. Coating them with oleic acid, which acts as a surfactant, facilitates the dispersion in solvents as a way to control the interparticle distance. In this section we explore the magnetism of Fe_3O_4 nanosphere powders with different size distributions. The samples are named based on their modal nanoparticle diameter (7 nm, 8.5 nm, and 10 nm).

5.1 Structure and morphology

The 7 nm, 8.5 nm, and 10 nm nanoparticle powder samples were analyzed. They consist of powder of Fe_3O_4 nanospheres of said diameters that were cleaned of their oleic acid layer to a point that they do not disperse in solvents anymore, granting them the biggest aggregation possible and the smallest interparticle distance of all our samples.

Table 5.1: Crystal parameters and sizes obtained from XRD data and TEM images.

Sample	lattice constant (Å)	crystallite size (nm)	particle diameter (nm)
7 nm	8.350	7.78 ± 0.07	6.9 ± 0.4
8.5 nm	8.355	8.08 ± 0.05	8.5 ± 0.3
10 nm	8.357	11.3 ± 0.1	10.1 ± 0.3

X-ray diffraction (XRD) patterns for the 7 nm, 8.5 nm, and 10 nm powder samples are shown in figure 5.1. A Rietveld refinement identified typical spinel structure ($Fd\bar{3}m$) characteristic of both Fe_3O_4 and γ-Fe_2O_3 crystal structure [71]. The broadening of the reflections is consistent with the particle volume decrease. The lattice constants for all samples are consistent with iron oxides and show little variation between sizes, evidencing that the particles are strain-free. The crystallite size was roughly estimated by using the Scherrer formula, equation 2.2, using the broadening of the main reflections. Their value sits close to the actual size of the nanoparticle measured by transmission electron microscopy images (TEM). Figure 5.2 shows TEM images of the particle systems. All samples have particles with spherical morphology and narrow size distribution. A thing to notice is that while the crystallite size of

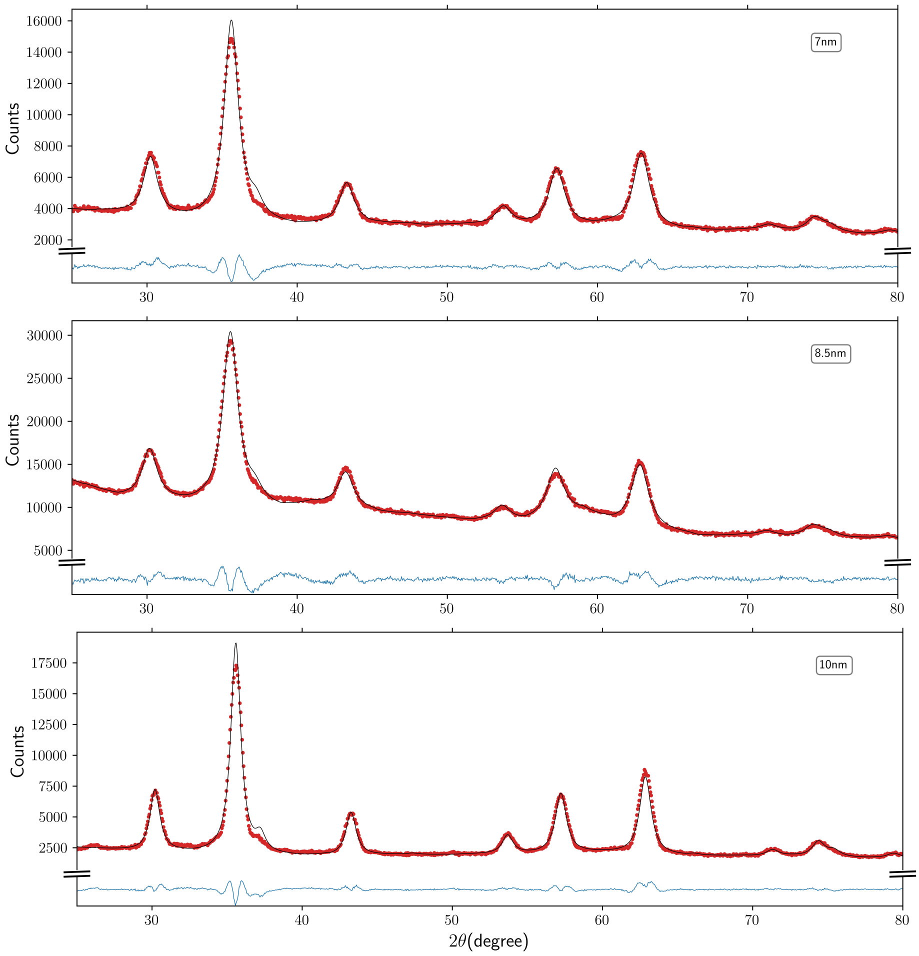

Figure 5.1: Powder x-ray diffraction pattern of 7 nm, 8.5 nm and 10 nm. The black lines show the results of the Rietveld refinement performed with FullProf. The observed diffraction pattern matches the characteristic pattern of spinel structures.

the 7 nm and 10 nm samples was overestimated to be 1 nm bigger than the actual size of the particle, for the 8.5 nm sample it appears to be smaller than its particle size. This observation suggests that the 8.5 nm sample presents lower crystallinity that adds extra broadening to the reflections.

Mössbauer spectra were obtained for all samples at 10 K to characterize the atomic ^{57}Fe electronic and magnetic environments via the hyperfine field (B_{hf}) and isomer shift (δ). As shown in figure 5.3, the spectra were fitted as a superposition of various

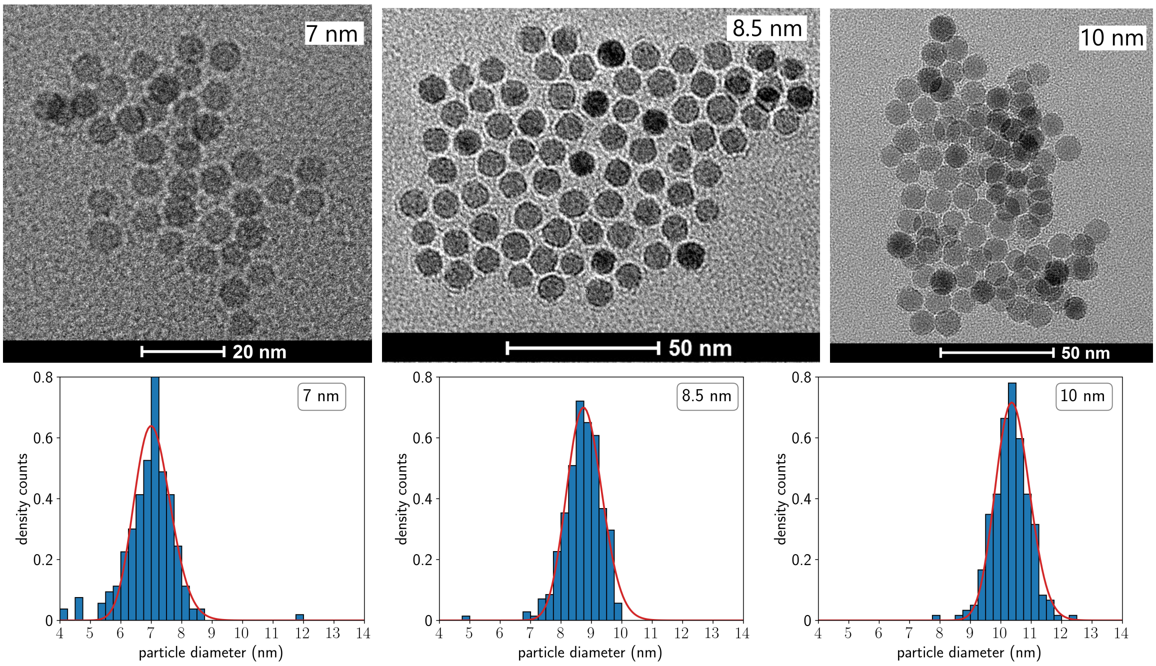

Figure 5.2: TEM images of the nanoparticle systems and size distributions. Images don't share the same magnification scale.

spectral components with specific hyperfine parameters. The hyperfine field and isomer shift values obtained for the 7 nm sample (see table 5.2) agree with the literature for Fe_3O_4 nanoparticles at low temperatures [72]. The spectra is composed of three components. It has two different values for B_{hf}, 53 T and 51 T, belonging to the B and A sites in the crystal structure, respectively. As well as one of the components having a higher δ that speaks of the different electronic structure present in the Fe^{2+} cation. The relative intensity of the components matches the 2:1 B to A ratio observed in Fe_3O_4.

For 8.5 nm and 10 nm, only two components of the spectra were resolved. B_{hf} values for 10 nm were identical to the 7 nm sample which suggests similar internal structure. On the other hand, 8.5 nm has visibly lower B_{hf} which indicates that this system's nanoparticles have a different internal structure. Further analysis of the

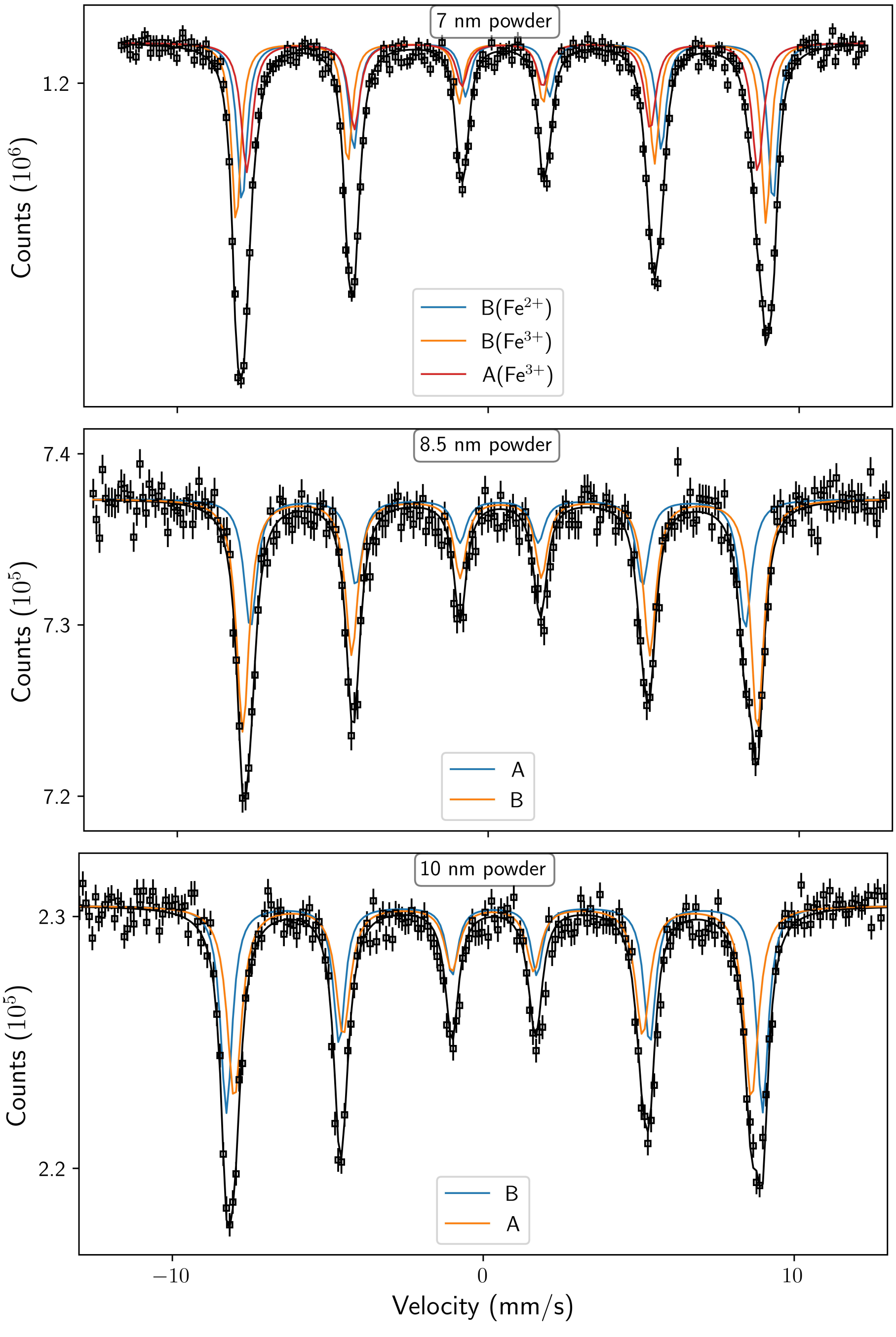

Figure 5.3: Mössbauer spectra collected at 10 K for the Fe_3O_4 powder samples. The solid lines are the results of a component fit as described in the text.

Table 5.2: Hyperfine parameters of the component fit of the Mössbauer spectra.

Size	site	δ (mm/s)	B_{hf} (T)	area (%)
7 nm	A(Fe^{3+})	0.455 ± 0.008	51.0 ± 0.1	34
	B(Fe^{2+})	0.62 ± 0.02	53.0 ± 0.1	32
	B(Fe^{3+})	0.41 ± 0.02		34
8.5 nm	A	0.33 ± 0.01	49.4 ± 0.1	36
	B	0.40 ± 0.01	51.4 ± 0.1	64
10 nm	A	0.310 ± 0.009	51.7 ± 0.2	40
	B	0.362 ± 0.07	53.5 ± 0.1	60

crystal and magnetic structures of Fe_3O_4 nanoparticles is not required for this work.

5.2 AC-susceptibility; dynamic magnetic properties

AC-susceptibility data was collected when heating from 5 to 300 K (after cooling in zero field) at seven different frequencies in a 2.5 Oe AC drive-field. The in-phase and out-of-phase AC-susceptibilities $\chi'(T, f)$ and $\chi''(T, f)$, shown in figure 5.4, have the frequency-dependent maxima that are characteristic of the dynamical freezing behaviour observed in cooled superparamagnetic nanoparticles as discussed earlier. They show that the position of the maxima on both $\chi'(T, f)$ and $\chi''(T, f)$ shifts toward higher temperatures when the size is increased. This shift is less sensitive to frequency changes than those obtained for the magnetoferritin samples. The $\chi_{ac}(T, f)$ of sample 10 nm showed two distinctive features not present in any of the other samples. It has a $\chi''(T, f)$ peak at ~40 K, as well as a small double-peak maxima in $\chi'(T, f)$ at $\sim$ 235 K (see figure 5.4 inset). These features suggest that even though the 10 nm nanoparticles

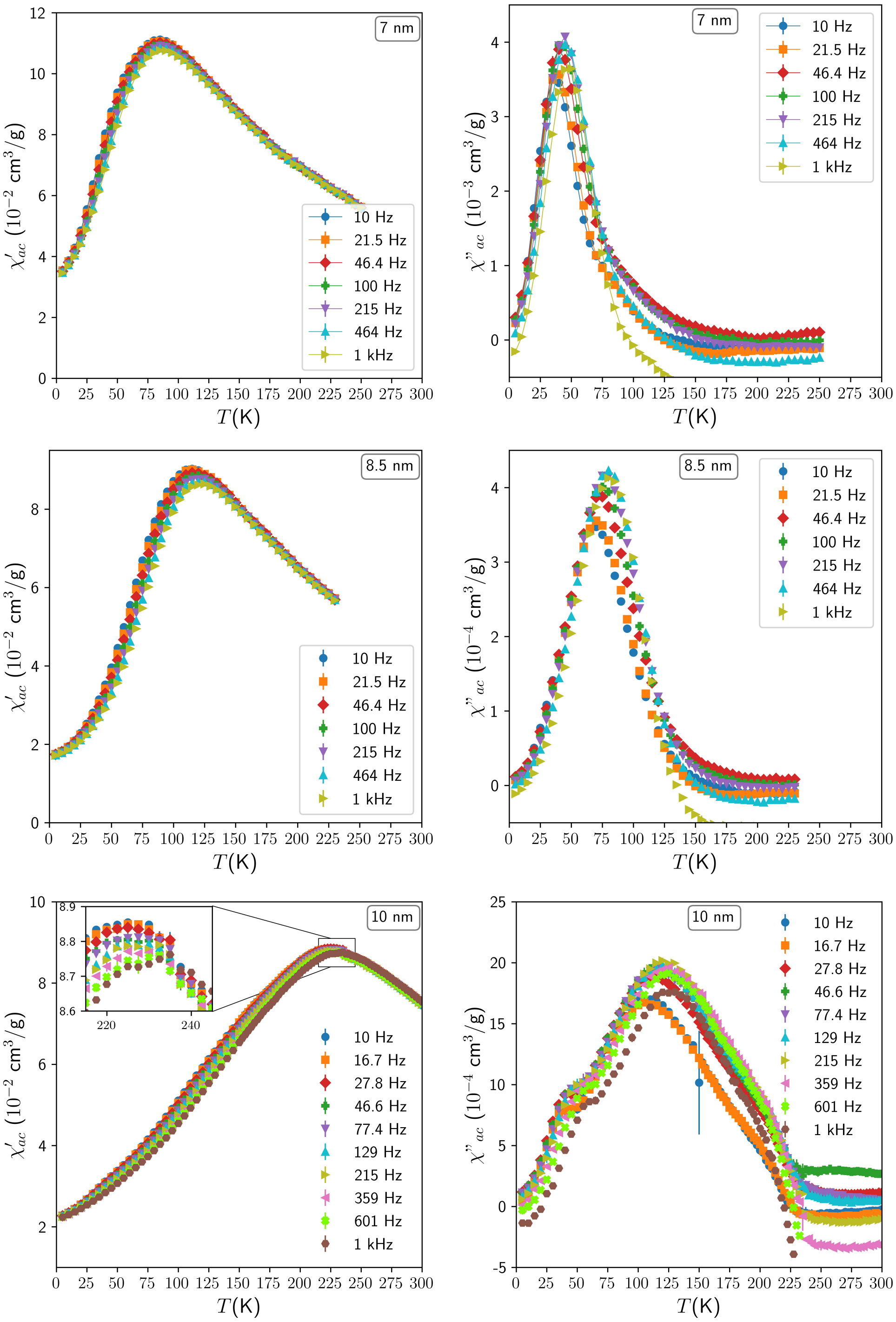

Figure 5.4: In-phase (left) and out-of-phase (right) AC-susceptibility for 7 nm, 8.5 nm and 10 nm Fe_3O_4 nanoparticle systems.

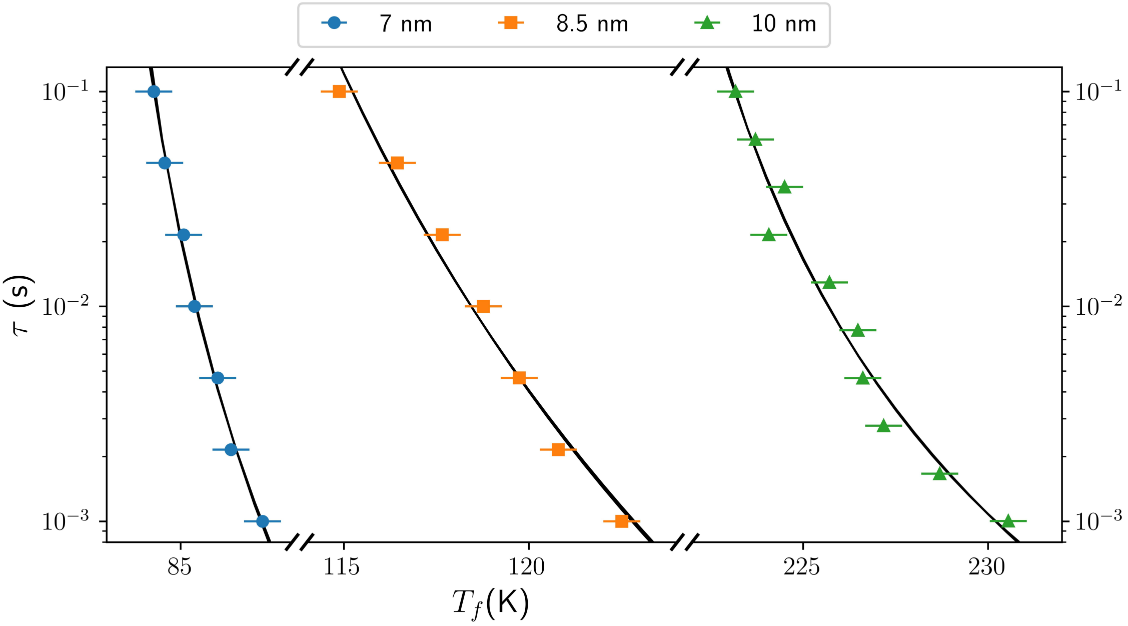

Figure 5.5: Frequency dependence of the freezing temperature. The solid lines are fits as described in the text. For each sample, the Vogel-Fulcher and the dynamic slowing down fits coincide in the measured frequency range.

are single-domain and superparamagnetic at room temperature, the larger size and stronger magnetic interactions may allow different magnetization reversal processes (e.g. the fanning process of correlated nanoparticle chains [73]), different from the purely coherent domain rotations assumed by the Stoner-Wohlfarth model. Analyzing the physics behind this phenomenon observed in the 10 nm sample is beyond the scope of this thesis. And thus, coherent domain reversals will be assumed regardless.

The Mydosh parameter, δ_f (equation 3.2), was used to compare the frequency sensitivity of spin freezing for the Fe_3O_4 samples. The obtained values are shown in table 5.3. δ_f were in the same range of insulating spin-glasses (e.g. 0.021 for $Eu_{0.4}Sr_{0.6}S$ [55, 74]). The larger value of δ_f observed for 8,5 nm suggests that interparticle interactions are weaker in this system [55].

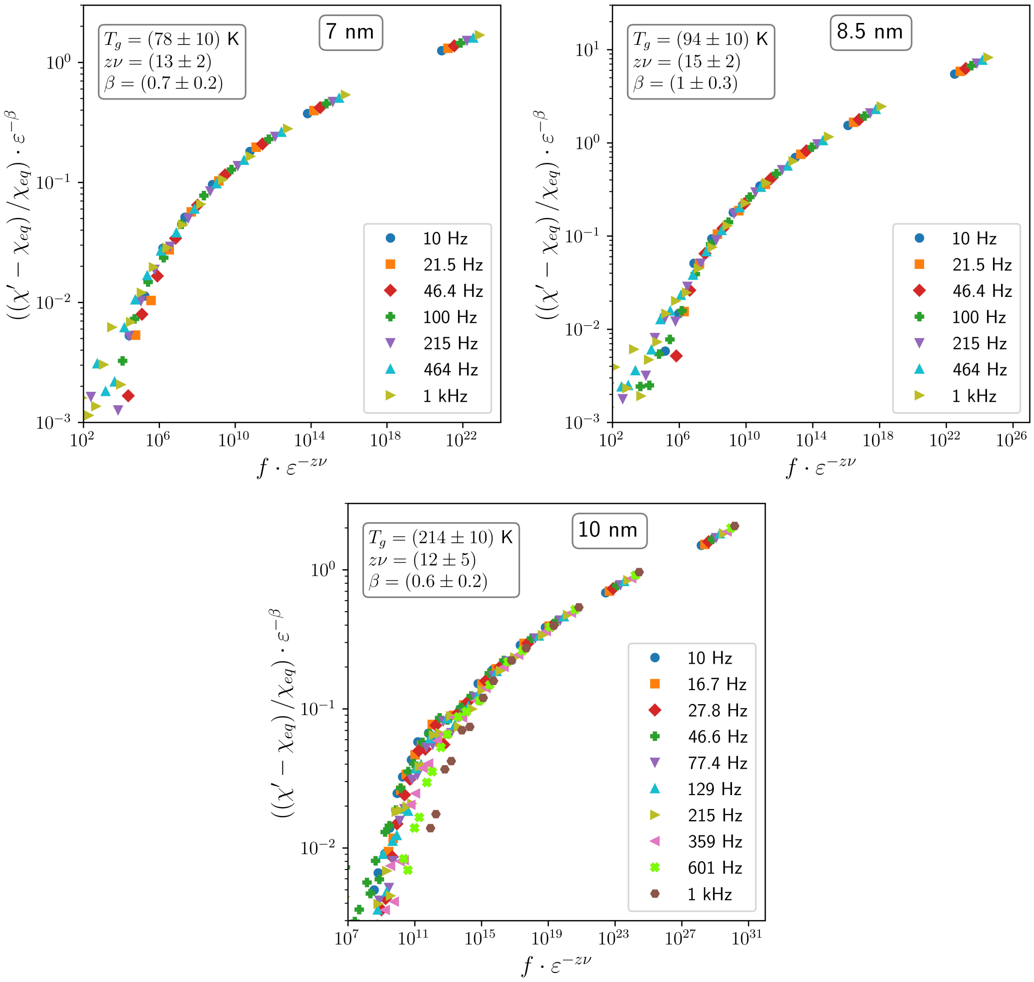

Figure 5.6: Rescaled AC-susceptibility data of the different sized nanoparticles. $\chi'(T, f)$ collapses onto a single curve when appropriate scaling exponents, β and $z\nu$, are chosen.

As before, simple Arrhenius behaviour was not observed. The frequency dependency of the maxima was fitted with the Vogel-Fulcher law (figure 5.5). The obtained coefficients are shown in table 5.3. T_0 increases with the particle size as expected. The values of K are smaller than Fe_3O_4 bulk (e.g. 18.7×10^4 erg/cm^3 [75]). The frequency dependency of the maxima was also fitted to the power law that describes the dynamic slowing down of spin-glasses equation 3.4. The obtained $z\nu$ exponents are shown in table 5.3 as well. Similar exponents has been reported in the literature

Table 5.3: Mydosh parameter, effective anisotropy, and critical parameters obtained by fitting the data with equations 3.2, 3.3 and 3.4.

Size	δ_f	T_0 (K)	K (10^4 erg/cm^3)	τ_0 (s)	$z\nu$
7 nm	0.018 ± 0.001	78 ± 2	6 ± 4	$(9 \pm 30) \times 10^{-9}$	4.8 ± 0.1
8.5 nm	0.030 ± 0.001	93 ± 4	16 ± 2	$(2 \pm 20) \times 10^{-9}$	7.3 ± 0.1
10 nm	0.016 ± 0.002	214 ± 5	2 ± 2	$(3 \pm 10) \times 10^{-6}$	4 ± 2

for iron oxide nanoparticle systems (e.g. 5.3 for γ-Fe_2O_3 [76])

Afterwards, dynamic scaling analysis was performed. Figure 5.6 shows the collapse of the data and the obtained critical exponents. We found that the dynamics of all our Fe_3O_4 nanoparticle powders are described by similar $z\nu$ and β exponents. 8.5 nm shows slightly higher values of both exponents, but they are still in range of the uncertainties. The data spread observed in the bottom-left corner of the last plot of figure 5.6, corresponding to 10 nm, is related to the double-peak maxima observed in $\chi'(T, f)$ in the same sample. Because of this special feature in 10 nm, the collapse is only seen for temperatures between 214 and 235 K (top-right corner of the last plot of figure 5.6).

5.3 Magnetization and DC-susceptibility; Static magnetic properties

DC-susceptibility, χ_{dc} vs T, was measured in zero field cooling (ZFC) and field cooling (FC) protocols, from 5 to 300 K, in a 50 Oe field. The data (shown in figure 5.7) reveals an increase in the freezing temperatures with size in agreement with χ_{ac} results. The 8.5 nm shows an anomaly in the magnetization; the ZFC line

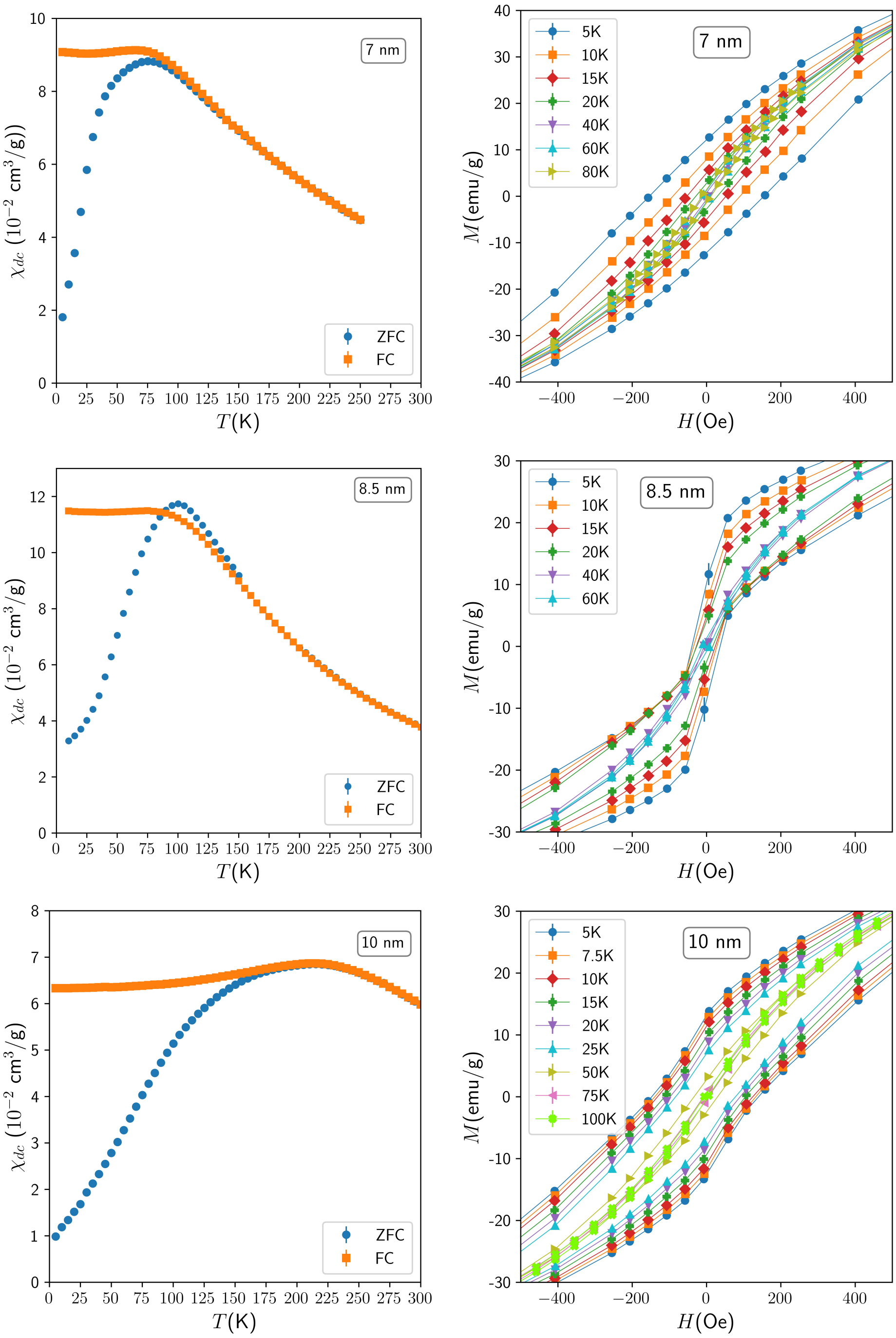

Figure 5.7: Left side: low field magnetization vs. temperature. Right side: Zoom in of M vs T showing hysteresis loops for the Fe_3O_4 nanoparticle powders of different sizes.

Table 5.4: Parameters obtained by fitting the data with Bloch T^{α} equation 3.12 and an estimation of the anisotropy with equation 3.13

Particle size	M_0 emu/g	b (10^{-6}K$^{-\alpha}$)	α	K (10^3 erg/cm^3)
7 nm	71.4 ± 0.1	13 ± 1	1.66 ± 0.01	9.8 ± 0.5
8,5 nm	51.4 ± 0.1	12 ± 2	1.63 ± 0.03	1.4 ± 0.1
10 nm	57.6 ± 0.1	2.2 ± 0.3	1.94 ± 0.03	5.7 ± 0.1

goes over the FC near the cusp. This feature disappeared when a larger H field of 200 Oe was used. This behaviour can be found in nanostructured multilayer films [77] but is something rare to find in pure systems like nanoparticles of magnetite. Further understanding of this anomaly observed in the magnetization was left for future work.

Magnetization versus applied field (M vs H) was measured at selected temperatures across the 5 to 350 K temperature range. M vs H hysteresis loops are shown in figure 5.7. The saturation magnetization, M_S, was obtained using the empirical law of approach to saturation $M = M_S(T)(1 - a/H^2) + \chi_{hf}H$. For pure Fe_3O_4 samples χ_{hf} arises from uncompensated surface spins. As seen in figure 5.8, the values of $\chi_{hf} \approx 10^{-5}$ cm^3/g are small and show an increasing trend with temperature. The increase of χ_{hf} with temperature is more pronounced the smaller the particles since the surface-to-volume ratio is inversely proportional to the particle size. The obtained $M_S(T)$ data was fitted to the Bloch T^{α} law for spin-wave excitations as seen in figure 5.8. The results are shown in table 5.4. There is a clear reduction of M_0 with particle size, which is minimum for 8.5 nm. There is also a decrease in the Bloch constant b and an increase in the α exponent with the increase in particle size. 7 nm and 8.5 nm have almost identical b and α.

M vs H hysteresis loops were observed at temperatures below blocking temperatures ($T_{B,HC}$) as expected. Figure 5.7 shows the loops at $T < T_{B,HC}$ for all sizes.

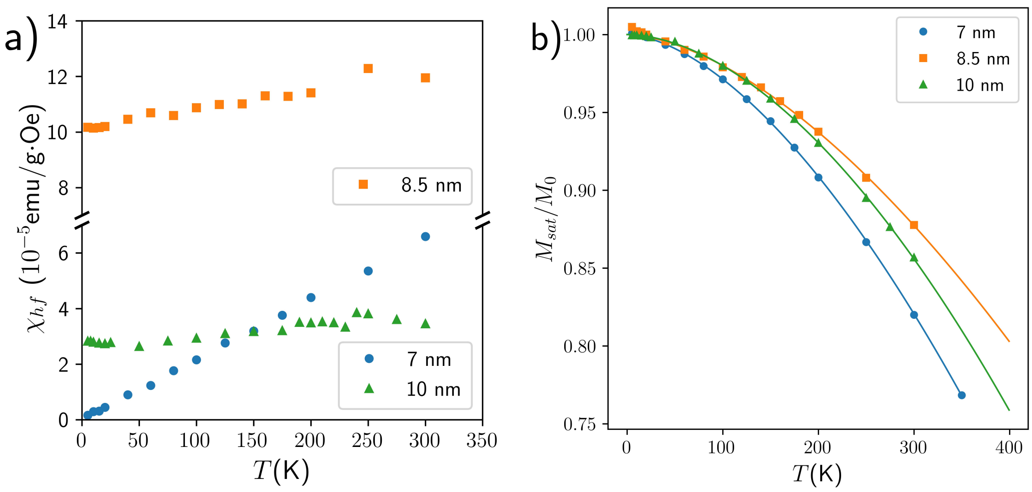

Figure 5.8: a) Temperature dependence of the high field susceptibility. b) Temperature dependence of the saturation magnetization. Solid lines are fits as described in the text

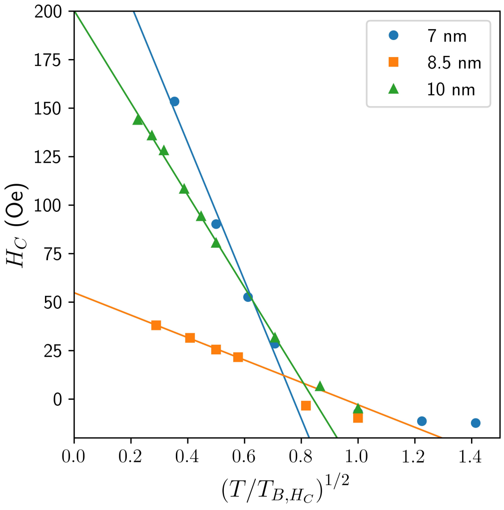

Figure 5.9: Temperature dependence of the coercivity of the different sized nanoparticles. Solid lines are fits as described in the text

The visible skewness that appears in the 8.5 nm sample for -100 Oe< $H < 100$ Oe is similar to the observed anomaly in the previous DC-susceptibility measurements (they are in the same field and temperature ranges). Estimations of the anisotropy (K) were performed by fitting the obtained coercivity from the hysteresis curves with equation 3.13, as seen in figure 5.9. The resulting K values (see table 5.4) are even smaller than those obtained previously from the AC-susceptibility. This can be explained by the fact that equation 3.13 is only valid for uniaxial non-interacting nanoparticles. Our powder samples have strong interparticle interactions and are, therefore, outside of equation's 3.13 validity range.

The inverse susceptibility $1/\chi_{dc}$ vs. T was plotted according to equation 3.14 and fitted with a linear function at high temperatures, as shown in figure 5.10. The low field susceptibility was well described by equation 3.15, $\chi_{dc} = \frac{\eta\rho V}{3k_B}\frac{M_S^2(T)}{(T+T^*)}$. In the case of the 10 nm sample, the fit was not possible since higher temperatures would be required to reach the free particle regime. For 7 nm and 8.5 nm, the fitted η and T^* are presented in table 5.5. The close-to-zero value found in the 8.5 nm sample suggests that interparticle interactions are weaker for this system. This value is identical to the value of T^* obtained for the pure magnetoferritin sample.

The low field susceptibility χ_{dc} was then used to perform scaling with equation 3.27 to the samples. The collapse of the data is shown in figure5.11. The obtained exponents for the Fe_3O_4 powders are shown in table 5.5. The γ exponent is larger for the 8.5 nm sample compared to 7 nm, and really close to the value found for the pure magnetoferritin. The similarities found between pure magnetoferritin and 8.5 nm Fe_3O_4 may indicate resemblance in the internal structure of the particles. Namely, the 8.5 nm nanoparticles may have in their composition a γ-Fe_2O_3 component which explains the differences in Mössbauer spectra observed between 8.5 nm and other Fe_3O_4 particle sizes.

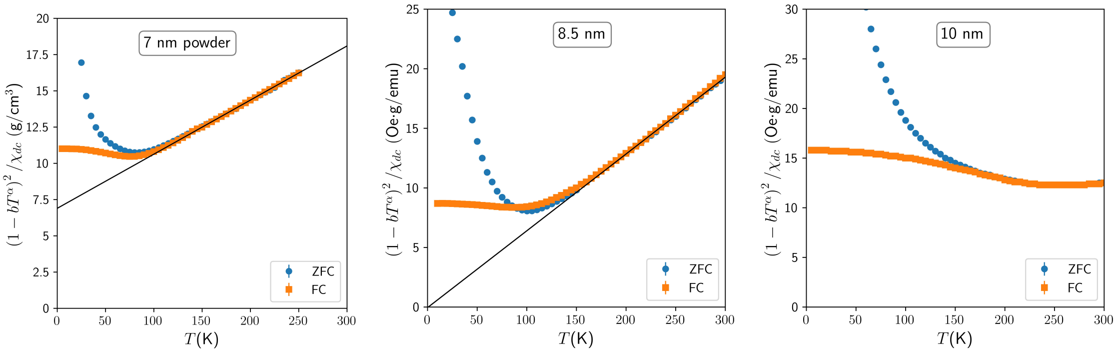

Figure 5.10: Low-field inverse susceptibility vs. temperature. The black lines are linear fits at the high-temperature regime.

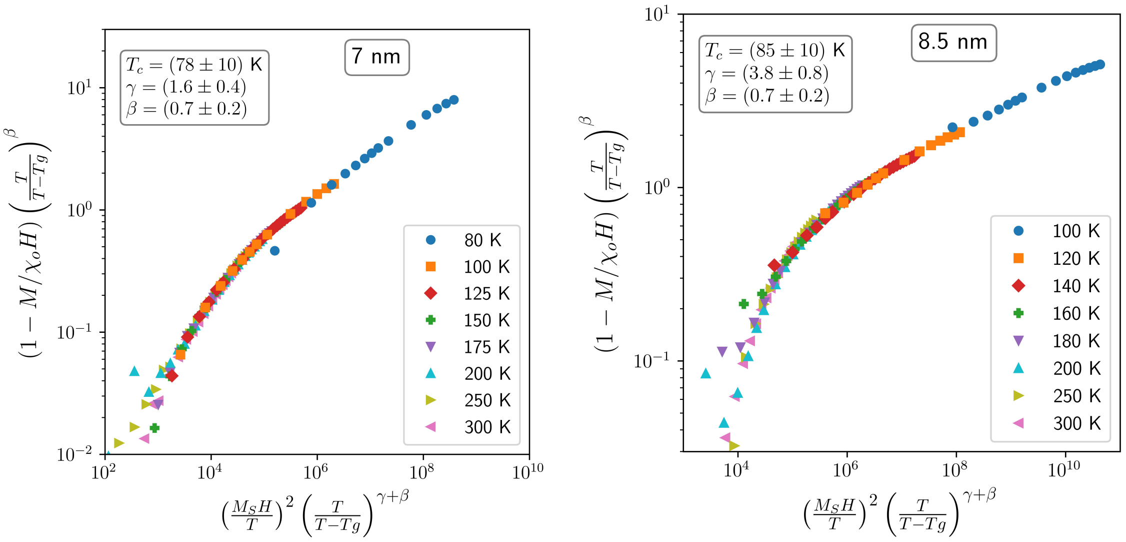

Figure 5.11: Rescaled magnetization data of the different sized nanoparticles. $M(H,T)$ data collapses onto a single curve when appropriate scaling exponents, β and γ, are set

Table 5.5: Parameters obtained by fitting the data with a modified Curie-Weiss law (equation 3.15) and critical exponents extracted from the scaling analysis.

Samples	η	T^* (K)	β'	γ
7 nm	3.0 ± 0.2	174 ± 6	0.7 ± 0.2	1.6 ± 0.4
8.5 nm	2.0 ± 0.3	0 ± 2	0.7 ± 0.2	3.8 ± 0.8

Chapter 6

Interparticle interactions: Dispersions of 7 nm Fe_3O_4 spheres with different interparticle distance

In this section we reduced the interparticle interactions of the ensembles by increasing the mean interparticle distance. Using the 7 nm powder sample as a reference, we coated it with oleic acid, resulting in an oxide mass concentration of $(11.6 \pm 0.8)\%$, and further diluted it in paraffin up to $(1.12 \pm 0.7) \times 10^{-2}\%$. This process resulted in three samples with different mean interparticle separations and therefore reduced interaction strength. The average interparticle distance was estimated as $\langle d \rangle \approx (22 \pm 3)$ nm and $\langle d \rangle \approx (220 \pm 30)$ nm, respectively, using the equation

$$\langle d \rangle = \frac{D}{2} \left(\frac{4\pi}{3n_v} \right)^{1/3} \tag{6.1}$$

where D is the mean nanoparticle diameter and n_v is the volume fraction. The samples are named powder, d22 and d220. It's important to point out that, since we lack a method to control agglomeration in our solutions, agglomeration may have been present in the systems.

The oxide masses of the dispersed samples were obtained by comparing the magnetic saturation data at 300 K after the diamagnetic components from paraffin and oleic acid were subtracted.

6.1 AC-susceptibility; dynamic magnetic properties

AC-susceptibility data was collected when heating from 5 to 300 K, after cooling in zero field, at seven different frequencies ranging from 10 Hz to 1 kHz in a 2.5 Oe drive-field. The in-phase and out-of-phase AC-susceptibilities, $\chi'(T, f)$ and $\chi''(T, f)$, figure 6.1, show the frequency-dependent maxima that were observed in all the samples. An inspection of the frequency-dependent maxima of $\chi'(T, f)$ reveals that the spin freezing becomes more sensitive to frequency as we decrease the concentration.

The Mydosh parameter, δ_f, (equation 3.2) used to compare the frequency sensitivity was calculated for the dilutions. The obtained values are shown in table 6.1. There is a clear increase in δ_f with the mean particle distance that indicates a decrease of the interparticle magnetic interactions [55]. The frequency dependency of the maxima was fitted with a Vogel-Fulcher law, equation 3.3, and with the critical slowing down described by equation 3.4 (figure 6.2). Results are displayed in table 6.1.

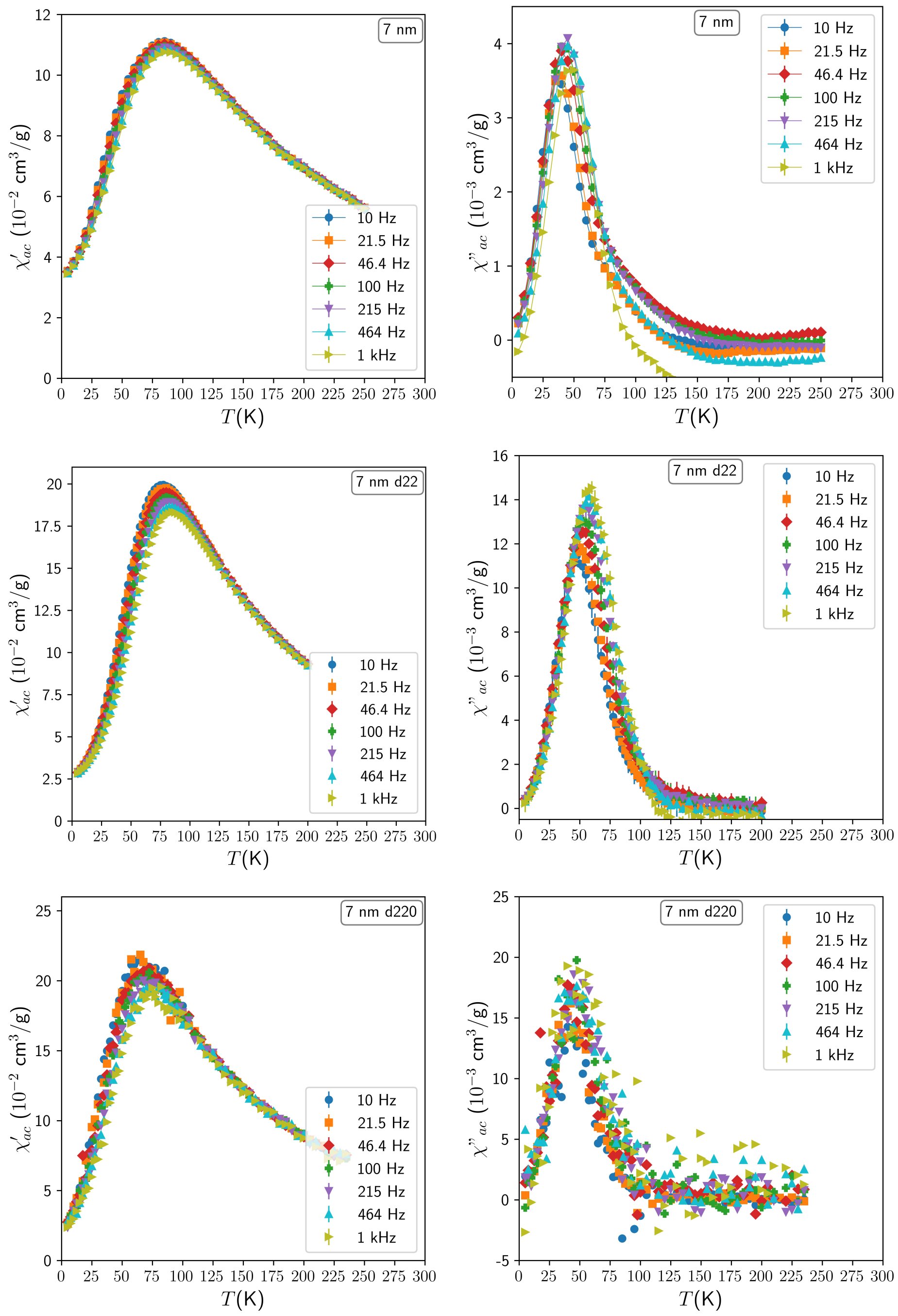

Figure 6.1: In-phase (left) and out-of-phase (right) AC-susceptibility for 7 nm Fe_3O_4 systems at different nanoparticle concentrations. The data from sample 7 nm d220 shows relatively high noise, represented by the random dispersion of the values. For clarity, the error bars were removed.

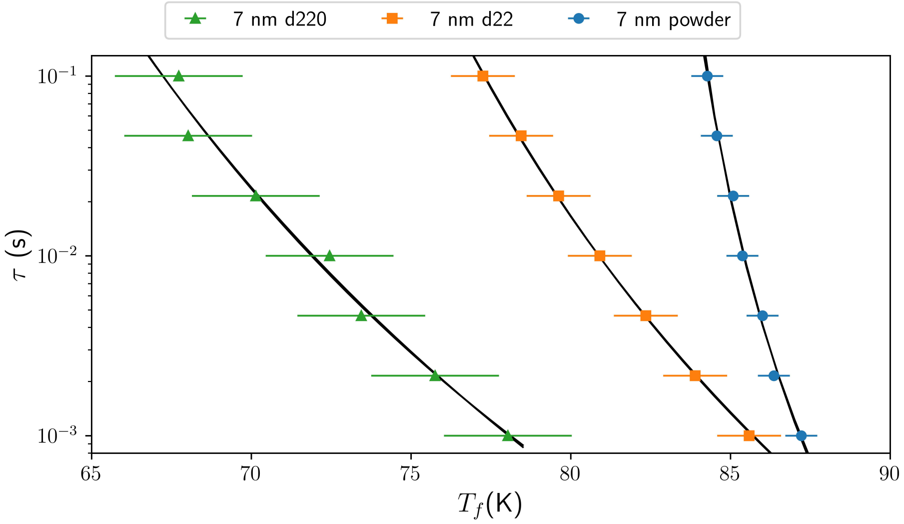

Figure 6.2: Frequency dependence of the freezing temperature. The solid lines are fits as described in the text. For each sample, the Vogel-Fulcher and the dynamic slowing down fits coincide in the measured frequency range.

Table 6.1: Mydosh parameter, effective anisotropy, and critical parameters obtained by fitting the data with equations 3.2, 3.3 and 3.4.

Sample	δ_f	T_0 (K)	K $(10^4$ erg/cm$^3)$	τ_* $(10^{-9}$s$)$	$z\nu$
7 nm powder	0.018 ± 0.01	78 ± 2	6 ± 4	8.6 ± 0.3	4.8 ± 0.1
7 nm d22	0.055 ± 0.02	65 ± 1	27 ± 1	2 ± 2	7.7 ± 0.1
7 nm d220	0.086 ± 0.04	50 ± 8	36 ± 4	1.4 ± 0.2	8.8 ± 0.1

We can see that the glass transition temperature T_g decreases and the exponent $z\nu$ increases with the decrease in concentration. The increased uncertainties reported for the 7 nm d220 come from the low signal-to-noise ratio (see figure 6.1) present in those measurements, which in turn arises from the relatively smaller oxide mass in the sample holder.

Dynamic scaling analysis was performed using the real part of the AC-susceptibility (figure 6.3). The obtained exponents don't agree with those of the critical slowing down (table 6.1). Namely, $z\nu = 12$ does not change with concentration. Also, β goes

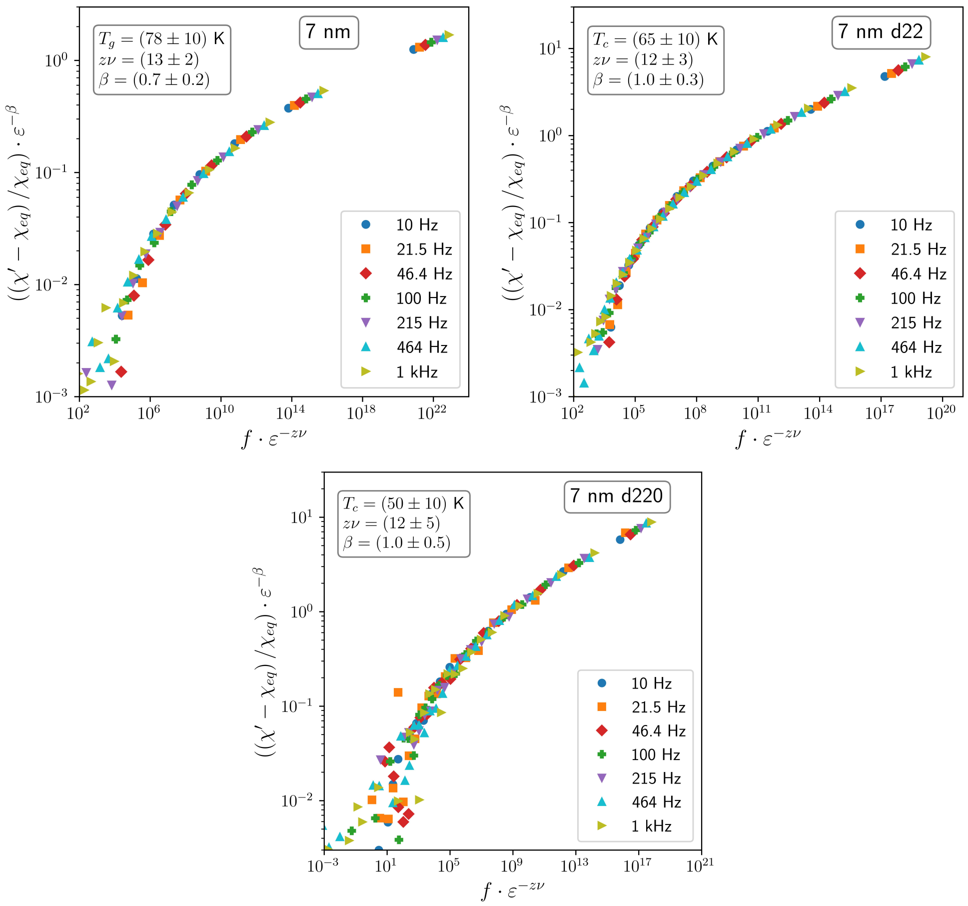

Figure 6.3: Rescaled AC-susceptibility data of the systems at different nanoparticle concentrations. $\chi'(T, f)$ collapses onto a single curve when appropriate scaling exponents, β and $z\nu$, are chosen.

from 0.5 to 1 when the sample is dispersed. Both dispersed samples have the same dynamical exponents regardless of the concentration.

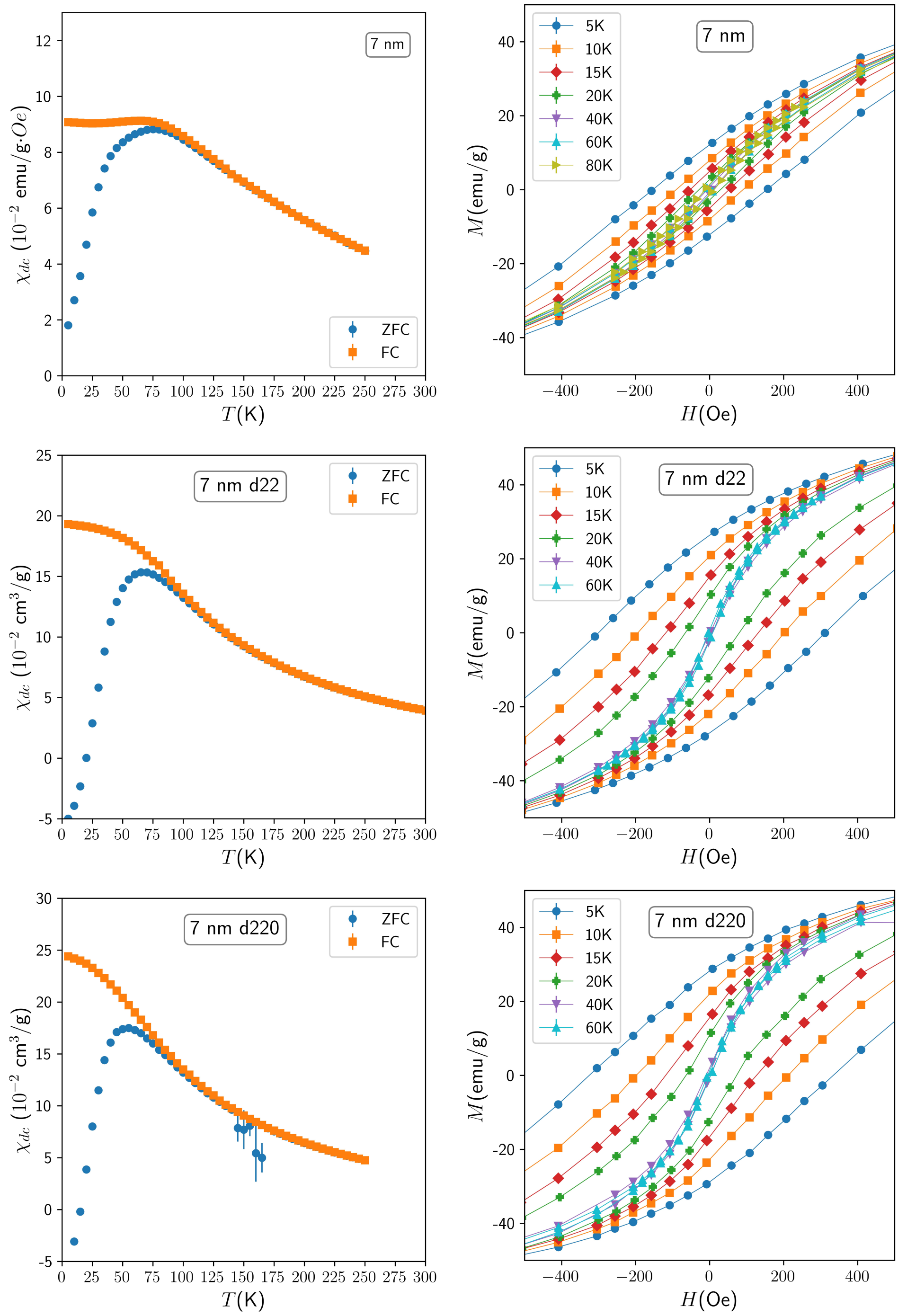

Figure 6.4: Left side: low field magnetization vs. temperature. Right side: Zoom in of M vs T showing hysteresis loops for the 7 nm sample at different concentrations.

6.2 Magnetization and DC-susceptibility; Static magnetic properties

M vs. T (see figure 6.4, top) was measured with zero field cooling (ZFC) and field cooling (FC) protocols, from 5 to 300 K in a 50 Oe field. Two things to notice are that dispersing the sample did decrease the temperature maxima of the ZFC susceptibility by a small amount and that the FC curve continues increasing in value when we further reduce the temperature. Both observations are indicative that the dispersion weakened the interparticle interactions strength.

Magnetization versus applied field (M *vs* H) was measured at selected temperatures across the 5 to 350 K temperature range. M *vs* H hysteresis loops are shown in figure 6.4. The coercivity, H_C, becomes larger when the sample is dispersed, and as a result, a better estimation of the K can be found when equation 3.13 is used (see figure 6.5.a and table 6.2).

The high-field susceptibility χ_{hf} and saturation magnetization, M_S, temperature dependencies were obtained with the empirical law of approach to saturation equation 3.11 (see figure 6.5.b). Due to the paraffin used as a dispersion medium, the sample 7 nm d220 presents a large diamagnetic component that becomes dominant at high fields. From the χ_{hf} fits, the paraffin diamagnetic component was estimated as $(-7 \pm 1) \times 10^{-7}$ g/cm^3, in agreement with literature [78]. The paraffin diamagnetic component was subtracted from the data. The resulting temperature dependence of the high-field susceptibility χ_{hf} is shown in figure 6.6.a. For the diluted samples (7 nm d22 and 7 nm d220), the temperature dependence of χ_{hf} indicated a paramagnetic-like behaviour ($\chi_{hf} \propto 1/T$) for $T < 50$ K. This paramagnetic-like

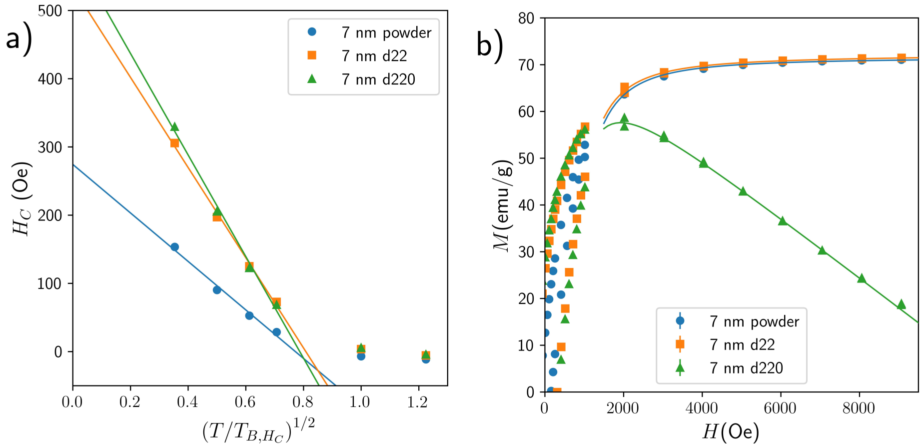

Figure 6.5: a) Temperature dependence of the coercivity of the different concentration nanoparticle systems. b) Magnetization at high fields at 5K. The solid lines are fits as described in the text.

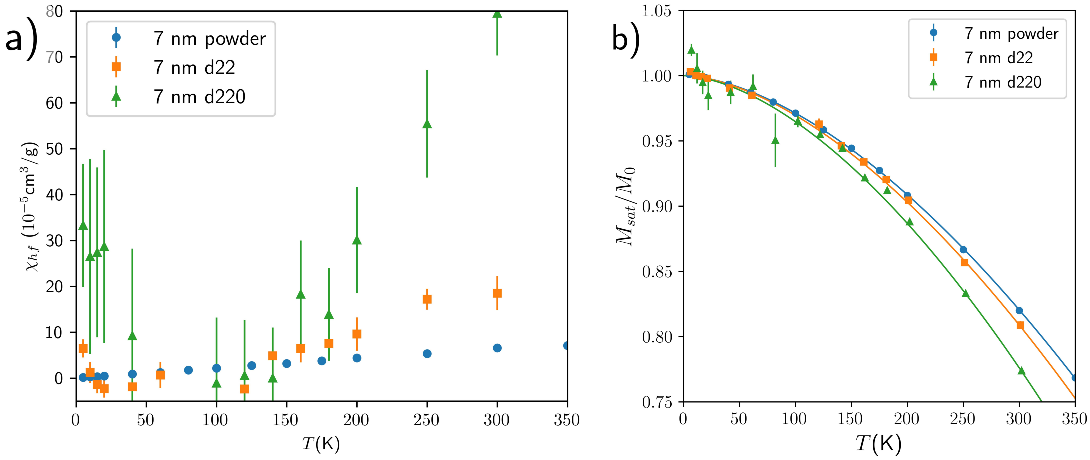

Figure 6.6: a) Temperature dependence of the high field susceptibility. b) Temperature dependence of the saturation magnetization. The solid lines are fits to the Bloch T^α law.

behaviour at low temperatures is not seen in any of the powder samples, and it is attributed to disordered spins in the surface of the particles. In the powder samples, the strong interparticle interactions reduce the mobility of surface spins, and their paramagnetic contribution is not observed.

The saturation magnetization $M_S(T)$ was then fitted to the Bloch T^α law for

Table 6.2: Parameters obtained by fitting the data with Bloch T^α equation 3.12 and an estimation of the anisotropy with equation 3.13

Sample	M_0 emu/g	b (10^{-6}K$^{-\alpha}$)	α	K (10^4 erg/cm^3)
7 nm powder	71.4 ± 0.1	13 ± 1	1.66 ± 0.01	0.98 ± 0.05
7 nm d22	72.3 ± 0.3	13 ± 4	1.67 ± 0.05	2.18 ± 0.06
7 nm d220	74.3 ± 0.8	15 ± 10	1.7 ± 0.2	2.2 ± 0.1

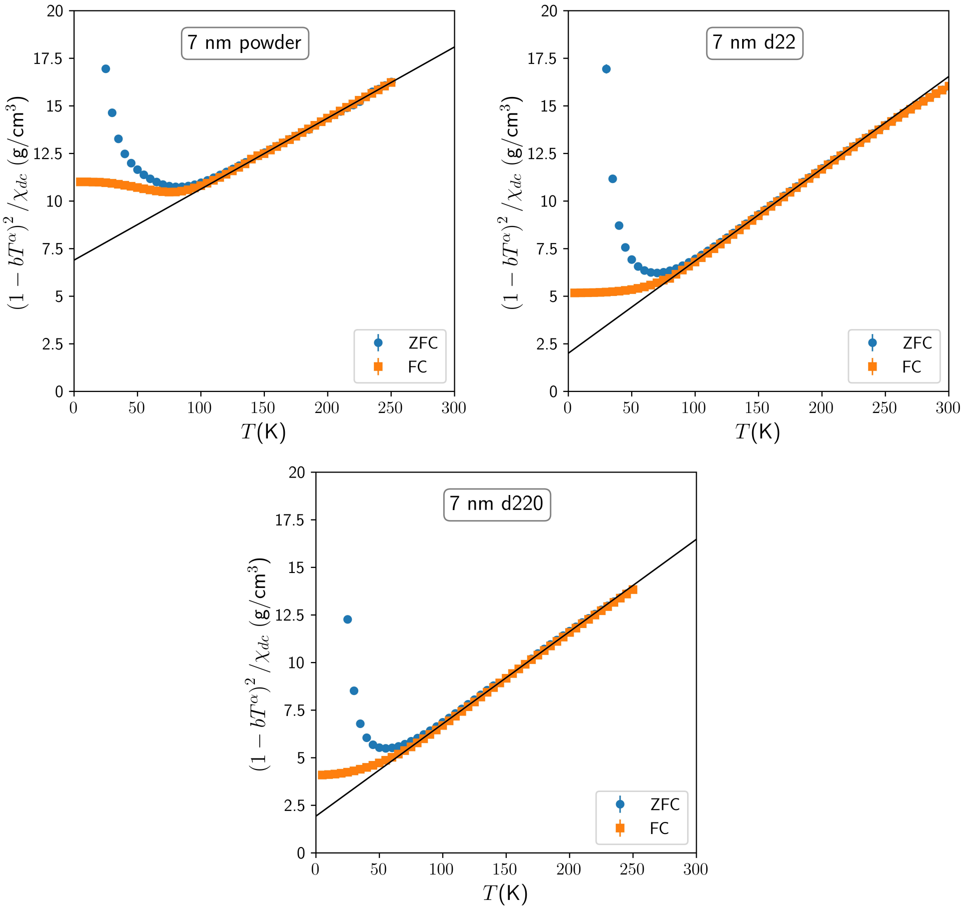

Figure 6.7: The low field inverse susceptibility vs. temperature. The black lines are linear fits at the high-temperature regime.

spin-wave excitations as displayed in figure 6.6b. The results are shown in table 6.2. The measured values of b and α are independent of the nanoparticles concentration, which indicates that the spin-wave oscillations that take place in the magnetic core are not influenced by interparticle interactions.

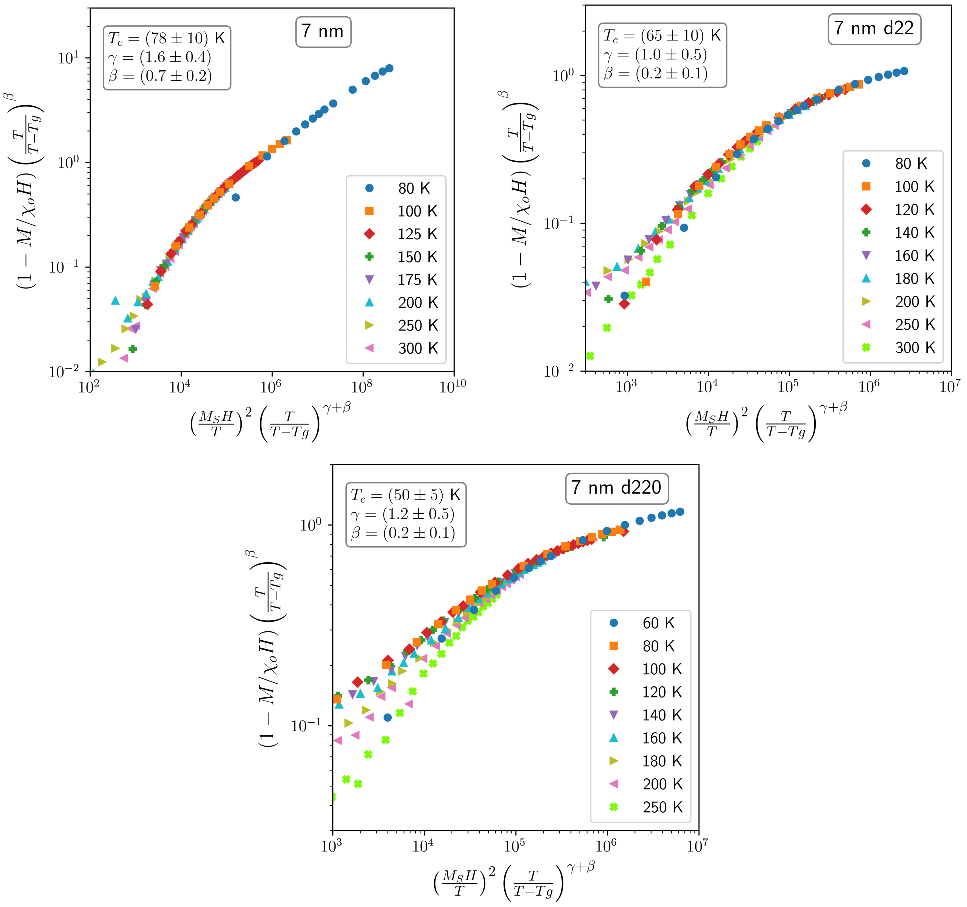

Figure 6.8: Rescaled magnetization data of the systems at different nanoparticle concentrations. For each concentration, $M(H,T)$ data collapses onto a single curve when appropriate scaling exponents, β and γ, are set.

The inverse susceptibility $1/\chi_{dc}$ vs. T was plotted according to equation 3.14 and fitted with a linear function at high temperatures, as shown in figure 6.7. The low field susceptibility was well described by equation 3.15, $\chi_{dc} = \dfrac{\eta\rho V}{3k_B}\dfrac{M_S^2(T)}{(T+T^*)}$. The fitted η and T^* are presented in table 6.3.

There is a clear decrease in both parameters with the decrease in concentration as we dilute the sample. The low field susceptibility χ_{dc} was then used to perform scaling with equation 3.27 to the samples. The collapse of the data is shown in figure 5.11.

The γ exponent does not change with the concentration, while the β exponent seems to reduce when the interaction strength decreases.

Table 6.3: Parameters obtained by fitting the data with a modified Curie-Weiss law (equation 3.15) and critical exponents extracted from the scaling analysis.

Samples	η	T^* (K)	β'	γ
7 nm powder	2.9 ± 0.2	174 ± 6	0.7 ± 0.2	1.6 ± 0.4
7 nm d22	2.5 ± 0.4	40 ± 4	0.2 ± 0.1	1.0 ± 0.5
7 nm d220	3 ± 1	40 ± 10	0.2 ± 0.1	1.2 ± 0.5

Chapter 7

Discussion

In this section we summarize and discuss our findings. In order to discern the effects from the particles' internal magnetic structure, size distribution, and interactions, the results are divided into sections based on our interpretations.

7.1 Intraparticle magnetism

For single-domain nanoparticles, the height of the energy barrier, which is described by the glass transition temperature T_g, increases with the volume of the nanoparticles, the anisotropy, and the magnetic interactions between nanoparticles. That trend was observed in our results. The smallest T_g belongs to the pure magnetoferritin particles (0% MF), which have the smallest size ($\approx$ 6 nm) and are well spaced due to being covered by a protein shell. Also, the dispersed 7 nm Fe_3O_4 samples have a relatively smaller T_g that increases as the average interparticle distance is reduced. On the other hand, the higher T_g for the cobalt-doped magnetoferritin samples with respect to the pure magnetoferritin indicates that the Co^{2+} addition to the crystal structure did increase the anisotropy.

The parameters related to the saturation magnetization and anisotropy are summarized in table 7.1. For the magnetoferritin samples, the saturation magnetization extrapolated to 0 K, (M_0), are in agreement with previous measurements of ferritin nanoparticles [79] and are close in value to the bulk magnetization of γ-Fe_2O_3 with $M_0 = 74$ emu/g, and Fe_3O_4 with $M_0 = 96$ emu/g [80]. The values obtained here are smaller than bulk as a result of the surface spin-canting effects that take place in small particles [69]. The further reduction with the doping concentration was attributed to changes in the magnetic structure due to the substitution of Co^{2+}. For the undoped magnetoferritin, $M_S(T)$ was well fitted by the normal Bloch law ($\alpha = 3/2$) and provided $b = 4 \times 10^{-5}$ $K^{-3/2}$, consistent with Fe-oxide nanoparticles [69]. However, for the doped samples, the obtained exponent was close to $\alpha = 2$.

The Bloch $T^{3/2}$ law assumes long wavelength spin-waves to be excited at low temperatures. A spin-wave is a perturbation on the magnetic ordering of the material that propagates. It can be understood as a coherent precession of the electron spins around their equilibrium direction, which influences adjacent spins through exchange interactions, causing the precession to propagate as a wave. In bulk magnetic materials, the wavelengths of spin-waves are limited only by the size of the sample. Thus, in finite-sized systems like nanoparticles, the wavelength of spin-waves is limited by the size of the particle. This creates gaps in the spin-wave low-energy spectrum that renders the Bloch $T^{3/2}$ law invalid at temperatures lower than the energy gap [81, 33, 82]. The low temperature dependence of magnetization can be described by a modified Bloch law with an effective exponent (α) that differs from the bulk value of 3/2. The energy gap of the spin-waves also appears in systems with high crystalline anisotropy. $\alpha = 2$ has been reported in the literature for bulk cobalt-ferrites (e.g. $Co_xFe_{3-x}O_4$ [70, 83]). The Co-doped samples provided $b \approx 2 \times 10^{-6}$ K^2, which is also consistent with a cobalt-ferrite composition [70]. Since there was no size difference between undoped and doped nanoparticles, these results evidence the higher intrinsic crystalline anisotropy of the Co-doped nanoparticles in agreement with our estimations.

On the other hand, for the Fe_3O_4 samples, the M_0 values are in agreement with previous measurements of Fe_3O_4 nanoparticles [84], which are also smaller than bulk values. There is a clear reduction of M_0 with the increase in particle size, which is minimum for 8.5 nm. The smaller M_0 for 8.5 nm with respect to the other sizes is attributed to differences in internal magnetic structure that were identified by Mössbauer spectroscopy and x-ray diffraction (as discussed in section 4.1). There is also a decrease in the Bloch constant and an increase in the α exponent for the 10 nm Fe_3O_4 nanoparticles that cannot be linked to a change in anisotropy. In fact, the trend reported in literature is the opposite: b tends to increase and α decreases with a reduction in anisotropy and an increase in particle size [85]. Because of the discrepancies in these results, and the differences in internal structure among the nanoparticle powder samples, we cannot link the change of the magnetic saturation to a change of volume of the nanoparticles alone. Additionally, among the Fe_3O_4 dispersions (7 nm powder, 7 nm d22, 7 nm d220) there is no observable change in the values of the Bloch constant b and the exponent α which indicates that interparticle interactions may not affect the spin-wave excitations that take place in the core of the magnetic particles.

The average anisotropy of the nanoparticles, K, was estimated using two different methods, by fitting the χ_{ac} data to the Vogel-Fulcher law (equation 3.3) and by

Table 7.1: Saturation magnetization and Anisotropy.

	Magnetoferritin		Dispersed 7 nm		Different sizes		
Sample	0% MF (6 nm)	7% Co (6 nm)	7 nm d220	7 nm d22	7 nm powder	8.5 nm powder	10 nm powder
T_g (K)	31 ± 1	161 ± 3	50	65	78 ± 2	93 ± 2	214 ± 5
$M_0(\mathrm{cm}^3/\mathrm{g})$	72 ± 3	63 ± 3	74.3 ± 0.8	72.3 ± 0.3	71.4 ± 0.1	51.4 ± 0.1	57.6 ± 0.1
b $(10^{-6}\mathrm{K}^{-\alpha})$	47 ± 6	2 ± 1	15 ± 10	13 ± 4	13 ± 1	12 ± 2	2.2 ± 0.3
α	1.47 ± 0.02	1.99 ± 0.08	1.7 ± 0.2	1.67 ± 0.05	1.66 ± 0.01	1.63 ± 0.03	1.94 ± 0.03
K $(10^4$ erg/cm$^3)$	45 ± 2	105 ± 5	36 ± 4	27 ± 1	6 ± 4	16 ± 2	2 ± 2

making use of the temperature dependencies of the coercivity, H_C, and magnetic saturation, M_S (equation 3.13). Both methods show similar trends with Co-doping, size and concentration even though the fitted K values differ. The magnetoferritin samples show an increase in H_C with cobalt concentration that does not scale with the increase in T_g. Therefore, the increase in coercivity cannot be attributed only to a change in the superparamagnetic relaxation time, suggesting that it was caused by an increase in anisotropy with the cobalt doping. Indeed, calculations suggest that K for the cobalt-doped samples was much higher than for the undoped nanoparticles, K was not proportional to the cobalt content, and was a maximum for 10% Co-doping. The increase in K values with the Co^{2+} substitution into the magnetoferritin structure agrees with the literature for $Co_xFe_{3-x}O_4$ nanoparticles of similar size [86].

The Fe_3O_4 nanoparticle powders show a totally different scenario. The K values obtained from the fit to the Vogel-Fulcher law are not a good estimate of the effective anisotropy of the nanoparticles; only the 8.5 nm sample shows a value somewhat close to the Fe_3O_4 bulk (18.7 × 10^4 erg/cm^3), when K tends to be larger than bulk and increases with the decrease of the nanoparticle size, which is a fact reported thoroughly in literature (e.g. [75] and references therein). The determination of magnetic properties of individual nanoparticles from a powder sample is difficult due to the unavoidable effects of the stronger magnetic interaction. Values extracted from equations 3.3, 3.13, and 3.9 are only valid in the limit of weak interactions. For strong interacting nanoparticle systems, the dipolar energies of the interactions may become more relevant than the anisotropy energies of individual nanoparticles, making it difficult to estimate the contributions from the anisotropy. This can be seen in the estimations of K for the dispersed 7 nm nanoparticle system. The value of K seems to increase with interparticle distance. However, since they are nanoparticles from the same batch, they have the same K. Thus, this apparent increase in K is due to the reduction of interparticle interactions. K values estimated for the dispersed sample are in agreement with reported values for Fe_3O_4 nanospheres of similar size [75].

7.2 Interparticle magnetic interaction

Interparticle interactions were present in the systems. Table 7.2 summarizes the results related to interparticle interactions. The values of the Mydosh parameter δ_f obtained from the frequency dependence of the AC-susceptibility can be used to qualitatively compare the strength of said interaction. δ_f values are typically of the order of 10^{-3} for metallic spin-glasses (e.g., 0.0050 for CuMn alloys [87]), of 10^{-2} for insulating spin-glasses (e.g., 0.05 for $ZnCr_{1.6}Ga_{0.4}O_4$ [88] and 0.021 for $Eu_{0.4}Sr_{0.6}S$ [55, 74]) and for cluster glasses (e.g. 0.06 for (Fe-Al_2O_3 granular thin films [65]). For superparamagnetic systems consisting of isolated magnetic entities, values of $\delta = 0.1$ have been obtained theoretically and measured (e.g. 0.13 for $La_{0.994}Gd_{0.006}Al_2$) [55, 89].

Our measured values go from 0.086 (weakest) to 0.016 (strongest), which are in the value range of spin clusters and insulating spin-glasses. The δ_f value depends mostly on the interparticle spacing. The largest values belong to the magnetoferritin samples whose magnetic cores are covered by ≈ 4 nm of organic cage and the dispersed samples, which are coated with oleic acid. Considerably smaller values were found for the Fe_3O_4 powder samples regardless of size, suggesting that interparticle interactions are far stronger. Incidentally, for 8.5 nm, δ_f is almost twice as large as the values for the other powders, which suggests that the reduction in the interaction strength is caused by a smaller magnetic moment of the nanoparticles due to their different internal structure.

Another place where the interparticle interactions are evidenced is in the fit to the modified Curie law (equation 3.15). In the ideal superparamagnetic case, $T^* = 0$. However, since that is not the case for our samples, it can be used to compare the strength of the interaction. The parameter T^* acts similar to the ordering temperature in the Curie-Weiss law for ferromagnetism. A quick inspection of table 7.2 reveals that T^* follows a similar trend to that of δ_f. Magnetoferritin and dispersed samples have relatively small T^*, indicating weaker interactions compared to the 7 nm nanoparticle powder. T^* is also small for the 8.5 nm nanoparticle powder, suggesting weak interparticle interactions that correlate with the small magnetic saturation observed in this system.

The parameter η included in the low-field susceptibility (equation 3.15) has no clear physical meaning. It can be interpreted as a modification to the effective volume of the magnetization. A value of $\eta > 1$ may indicate that the magnetic entity whose magnetization is blocked below T_g has a larger volume than the particle itself, suggesting agglomeration of correlated clusters of particles. However, an increase in

Table 7.2: Parameters used to compare the strength of the magnetic interactions between particles in the samples.

	Magnetoferritin		Dispersed 7 nm		Different sizes		
Sample	0% MF (6 nm)	7% Co (6 nm)	7 nm d220	7 nm d22	7 nm powder	8.5 nm powder	10 nm powder
T_g (K)	31 ± 1	161 ± 3	50 ± 8	65 ± 1	78 ± 2	93 ± 2	214 ± 5
$\delta_f(10^{-2})$	8.6 ± 0.3	5.0 ± 0.1	8.6 ± 0.4	5.5 ± 0.2	1.8 ± 0.1	3.0 ± 0.1	1.6 ± 0.2
T^*(K)	2 ± 6	66 ± 4	40 ± 10	40 ± 4	174 ± 6	0 ± 2	-
η	3.0 ± 0.3	5.0 ± 0.6	3 ± 1	2.5 ± 0.4	2.9 ± 0.2	2.0 ± 0.3	-

η can also be related to non-Langevin behaviour due to anisotropy. The obtained η is close to 3 in pure magnetoferritin and in the 7 nm Fe_3O_4 samples. η does not decrease with the average interparticle distance, as seen in the values for the different dispersions (7 nm d22 and 7 nm d220). The value of η seems to change only when internal structural changes are present, i.e. $\eta = 5$ for the cobalt-doped magnetoferritin sample and 2 for the 8.5 nm powder.

When we compared the cobalt-doped and undoped magnetoferritin, we found that all the parameters discussed here indicate stronger interparticle interaction for the cobalt-doped samples. However, the interparticle spacing does not change between samples, and the magnetization of the cobalt-doped magnetoferritin particles decreased with the dopant concentration, which should result in an equal or smaller interaction strength. This suggests that δ_f and T^* are also influenced by anisotropy and hence, the interplay between anisotropy and interparticle interactions cannot be separated by these means.

7.3 Critical behaviour

First, we must compare the $z\nu$ exponents obtained from the data collapse to the dynamic scaling ($z\nu$-scaling) with those obtained from the critical slow-down of the relaxation time ($z\nu$-CSD). For the magnetoferritin samples, it is observed that both $z\nu$ estimations agree and are close in value for the doped and pure samples and show a slight increase with dopant concentration. This suggests that the growth of the correlation length and relaxation time are not affected by the cobalt addition. The dynamic β exponent for the doped sample shows a clear increase when the system is doped, but no further dependence on the dopant concentration. Critical exponents with similar values have been reported in the literature for disordered Heisenberg antiferromagnets (e.g., $z\nu = 9 - 12$ and $\beta = 0.6 - 0.9$ for $Cd_{0.7}Mn_{0.3}Te$ [90, 91, 92] and references therein). The static exponents (β' and γ) obtained from the collapse of the pure magnetoferritin data correspond to short-range Ising and Heisenberg spin-glasses [57, 93, 94]. And since $\beta = \beta'$, we can use the hyperscaling relations

$$\alpha = 2 - 2\beta - \gamma, \qquad \nu = (2 - \alpha)/d, \qquad \text{and} \quad \delta = (\gamma + \beta)/\beta, \tag{7.1}$$

to determine other exponents as well. The exponents obtained from the hyperscaling relations are shown in table 7.4. Similar exponents were found in 3D Ising spin-glasses (e.g. $Fe_{0.5}Mn_{0.5}TiO_3$ [16]). The agreement between static and dynamic scaling is a strong argument in favor of a phase transition for the pure magnetoferritin sample.

On the other hand, $z\nu$-CSD and $z\nu$-scaling exponents obtained from the Fe_3O_4 samples show a mismatch, which correlates with the interparticle interaction strength. These discrepancies in the dynamic exponents are often found when different scaling

Table 7.3: Critical exponents. From top to bottom: $z\nu$ obtained from the critical slowing down fit, equation 3.4. $z\nu$ and β from the data collapse to equation 3.6. And β' and γ from the static scaling, equation 3.27

	Magnetoferritin		Dispersed 7 nm		Different sizes		
Sample	0% MF	7% Co (6 nm)	7 nm d220	7 nm d22	7 nm	8.5 nm	10 nm
T_g (K)	31 ± 1	161 ± 3	50 ± 8	65 ± 1	78 ± 2	93 ± 4	214 ± 5
$z\nu$-CSD	14 ± 0.3	14 ± 0.2	8.8 ± 0.1	7.7 ± 0.1	4.8 ± 0.1	7.3 ± 0.1	4 ± 2
$z\nu$-scaling	12 ± 1	14 ± 1	12 ± 5	12 ± 3	13 ± 2	15 ± 2	12 ± 5
β	0.4 ± 0.1	0.8 ± 0.1	1.0 ± 0.5	1.0 ± 0.3	0.7 ± 0.2	1 ± 0.3	0.6 ± 0.2
β'	0.4 ± 0.1	-	0.2 ± 0.1	0.2 ± 0.1	0.7 ± 0.2	0.7 ± 0.2	-
γ	4.0 ± 0.5	-	1.2 ± 0.5	1.0 ± 0.5	1.6 ± 0.4	3.8 ± 0.8	-

approaches are used, which leads to authors reporting dissimilar values [21]. Nevertheless, if we take $z\nu$ from the collapse of the real part of χ_{ac} data as accurate, then all samples have similar $z\nu \approx 13$ values, which would suggest that the growth of the correlation length and correlation time are not affected by anisotropy, concentration, and size, which seems counter-intuitive, since in the limit of non-interacting nanoparticles the correlation length is effectively zero.

On the contrary, sticking to the values of $z\nu$-CSD would mean that the correlation length and time of the systems grow slower for stronger interacting systems and hence are less sensitive to temperature changes. The β values from the Fe_3O_4 also show noticeable differences. The $\beta' \approx 0.7$ from the 7 nm powder sample is in good agreement with the value found during the dynamic scaling, which supports the idea that a phase transition takes place in this system. Using the hyperscaling relations (equation 7.1) the other critical exponents were found (see table 7.4). In regard to the 8.5 nm powder sample, the β exponents from static and dynamic scaling are close within uncertainties and therefore, similarly to the 7 nm powder, the other critical exponents can be found. However, for our diluted samples, 7 nm d22 and 7 nm

Table 7.4: Critical exponents obtained from the combination of dynamic and static scaling.

Sample	α	β	γ	δ	ν	z
0% MF	-2.8 ± 0.7	0.4 ± 0.1	4 ± 0.5	11 ± 4	1.6 ± 0.2	7.5 ± 0.8
7 nm	-1 ± 0.8	0.7 ± 0.2	1.6 ± 0.4	3 ± 2	1.0 ± 0.3	12 ± 3
8.5 nm	-3 ± 1	0.7 ± 0.2	3.8 ± 0.8	6 ± 3	1.7 ± 0.2	9 ± 1

d220, a clear discrepancy between dynamic and static exponents was found. This discrepancy suggests that, in our diluted systems, collective behaviour is suppressed because of the weaker interparticle interactions.

Finally, it is important to mention that scaling analysis can only be used as an indication of superspin freezing. Definitive proof for the existence of a superspin-glass state requires the measurement of ZFC memory effects [95, 96], but that is a topic for future work.

Chapter 8

Conclusions and suggestions for future work

The existence of collective nanoparticle freezing was successfully identified in our systems. The results of fitting the susceptibility data with the Vogel-Fulcher law, the Mydosh parameter, and the ordering temperature θ from the fit to the Curie-Weiss law, showed a dependency of the collective freezing with the nanoparticle properties (i.e. anisotropy, size, interparticle spacing). A clear increase of the glass temperature with anisotropy and interparticle interaction strength was identified. The doped magnetoferritin nanoparticle showed that changes in the internal structure of the nanoparticle influence properties that are usually attributed to the interactions (glass temperature, frequency sensitivity of the AC-susceptibility), while the interaction strength can affect our estimations of internal properties of the nanoparticles such as the anisotropy. We also extracted from our analysis critical exponents that compare well with the literature. We found that the anisotropy of the nanoparticles influence the critical exponents. Also, the dispersed samples showed inconsistencies in the critical exponents, which suggest that collective behavior is suppressed in diluted systems. The fact that critical exponents depend on internal properties of the particles puts in question the universality of the superspin-glass transitions.

One topic for future work is to test the crossover between superparamagnetic and superspin-glass that depends on the ratio of dipolar to anisotropy energies. One of the limitations of this work is that we did not have an appropriate range of interparticle interaction strength to study the crossover between single-particle and collective behaviour. An improved way of controlling the interparticle spacing can be achieved by coating the particles with silica and tuning the coat wall thickness. Another important topic for future research is to perform experiments looking for aging and memory effects. Testing those emergent phenomena in nanoparticle systems is important due to their possible application for neuromorphic and probabilistic computing.

Additionally, the interplay between anisotropy and interparticle interactions could not be resolved. A theory that uses a microscopic approach to determine the effects of anisotropy on susceptibility is required. On top of that, we did not consider the effects of the volume distribution (although the systems studied here were highly monodisperse) of the nanoparticles on the magnetization or the random distribution of the anisotropy axes within the assembly. A more detailed theoretical examination can be a topic for future work.

Bibliography

[1] E. Skoropata, R. D. Desautels, E. Falvo, P. Ceci, O. Kasyutich, J. W. Freeland, and J. van Lierop. Intra- and interparticle magnetism of cobalt-doped iron-oxide nanoparticles encapsulated in a synthetic ferritin cage. *Physical review. B*, 90(17), 2014.

[2] B. Martínez, X. Obradors, Ll Balcells, A. Rouanet, and C. Monty. Low temperature surface spin-glass transition in $\gamma - Fe_2O_3$ nanoparticles. *Physical review letters*, 80(1):181–184, 1998.

[3] Subhankar Bedanta and Wolfgang Kleemann. Supermagnetism. *Journal of physics. D, Applied physics*, 42(1):013001–013001 (28), 2009.

[4] E.C. Stoner and E.P. Wohlfarth. A mechanism of magnetic hysteresis in heterogeneous alloys. *IEEE transactions on magnetics*, 27(4):3475–3518, 1991.

[5] Michel Prévot and David Dunlop. Louis Néel: forty years of magnetism. *Physics of the earth and planetary interiors*, 126:3–6, 2001.

[6] William Fuller Brown. Thermal fluctuations of a single-domain particle. *Physical review*, 130(5):1677–1686, 1963.

[7] Günter Reiss and Andreas Hütten. Applications beyond data storage. *Nature materials*, 4(10):725–726, 2005.

[8] Pedro Tartaj, Maria P. Morales, Teresita Gonzalez-Carreño, Sabino Veintemillas-Verdaguer, and Carlos J. Serna. The iron oxides strike back: From biomedical applications to energy storage devices and photoelectrochemical water splitting. *Advanced materials (Weinheim)*, 23(44):5243–5249, 2011.

[9] J.L Dormann, R Cherkaoui, L Spinu, M Noguès, F Lucari, F D'Orazio, D Fiorani, A Garcia, E Tronc, and J.P Jolivet. From pure superparamagnetic regime to glass collective state of magnetic moments in $\gamma - Fe_2\mathrm{O}_3$ nanoparticle assemblies. *Journal of magnetism and magnetic materials*, 187(2):L139–L144, 1998.

[10] A. P. Malozemoff and B. Barbara. Physical model for static and dynamic scaling in spin glasses. *Journal of applied physics*, 57(8):3410–3412, 1985.

[11] L. Lundgren, P. Nordblad, and P. Svedlindh. Relaxation behavior of fractal-cluster spin glasses. *Physical review. B, Condensed matter*, 34(11):8164–8167, 1986.

[12] Mucio Continentino and Alexis P. Malozemoff. Dynamical susceptibility of spin glasses in the fractal cluster model. *Physical review. B, Condensed matter*, 34(1):471–474, 1986.

[13] Stephen Blundell. *Magnetism in condensed matter.* Oxford University Press, Oxford, 1 edition, 2001.

[14] Nigel Goldenfeld. *Lectures on phase transitions and the renormalization group.* CRC Press, Boca Raton, 2019.

[15] K. H. Fischer and J. A. Hertz. *Spin glasses.* Cambridge University Press, Cambridge, 1991.

[16] J. A. Mydosh. *Spin Glasses: An Experimental Introduction.* Taylor & Francis, London, 1993.

[17] M. Suzuki. Static and dynamic finite-size scaling theory based on renormalization group approach. *Progress of theoretical physics*, 58(4):1142–1150, 1977.

[18] J. Chalupa. Scaling at the critical temperature of a spin glass. *Solid state communications*, 24(6):429–431, 1977.

[19] S. Geschwind, A. T. Ogielski, G. Devlin, J. Hegarty, and P. Bridenbaugh. Activated dynamic scaling and magnetic ordering in $\mathrm{Cd}_{1-x}\mathrm{Mn}_x\mathrm{Te}$: Spin glass or random antiferromagnet? (invited). *Journal of applied physics*, 63(8):3291–3296, 1988.

[20] P. C. Hohenberg and B. I. Halperin. Theory of dynamic critical phenomena. *Reviews of modern physics*, 49(3):435–479, 1977.

[21] N. Bontemps, J. Ferre, and A. Mauger. Dynamic scaling in spin-glasses: What to scale. *Journal de physique*, 49(C-8):1063–1064, 1988.

[22] P. Beauvillain, J. P. Renard, M. Matecki, and J. J. Prejean. Critical dynamics in spin glasses: Experimental study and fractal model interpretation. *Europhysics Letters*, 2(1):23, jul 1986.

[23] Andrew T. Ogielski. Dynamics of three-dimensional Ising spin glasses in thermal equilibrium. *Physical review. B, Condensed matter*, 32(11):7384–7398, 1985.

[24] D.P.E. Dickson, N.M.K. Reid, C. Hunt, H.D. Williams, M. El-Hilo, and K. O'Grady. Determination of f_0 for fine magnetic particles. *Journal of magnetism and magnetic materials*, 125(3):345–350, 1993.

[25] William Fuller Brown. Relaxational behavior of fine magnetic particles. *Journal of Applied Physics*, 30(4):S130–S132, 1959.

[26] Cristian E. Botez and Joshua L. Morris. Ac-susceptibility investigations of superspin blocking and freezing in interacting magnetic nanoparticle ensembles. *Nanotechnology*, 27(11):115706, feb 2016.

[27] J. L. Dormann, D. Fiorani, E. Tronc, Stuart A. Rice, and I. Prigogine. Magnetic relaxation in fine-particle systems. *Advances in chemical physics, VOL 98*, 98:283–494, 1997.

[28] E. F. Kneller and F. E. Luborsky. Particle size dependence of coercivity and remanence of single-domain particles. *Journal of applied physics*, 34(3):656–658, 1963.

[29] E.P Wohlfarth. The temperature dependence of the magnetic susceptibility of spin glasses. *Physics letters. A*, 70(5):489–491, 1979.

[30] F. Wiekhorst, E. Shevchenko, H. Weller, and J. Kotzler. Anisotropic superparamagnetism of monodispersive cobalt-platinum nanocrystals. *Physical review. B*, 67(22), 2003.

[31] M. Respaud, J. Broto, H. Rakoto, A. R. Fert, L. Thomas, B. Barbara, M. Verelst, E. Snoeck, P. Lecante, A. Mosset, J. Osuna, T. Ould Ely, C. Amiens, and B. Chaudret. Surface effects on the magnetic properties of ultrafine cobalt particles. *Physical review. B, Condensed matter*, 57(5):2925–2935, 1998.

[32] Conyers Herring and Charles Kittel. On the theory of spin waves in ferromagnetic media. *Physical review*, 81(5):869–880, 1951.

[33] S. Cojocaru. Magnon gas and deviation from the Bloch law in a nanoscale Heisenberg ferromagnet. *Solid state communications*, 151(23):1780–1783, 2011.

[34] P. V. Hendriksen, S. Linderoth, and P.-A. Lindgård. Finite-size modifications of the magnetic properties of clusters. *Physical review. B, Condensed matter*, 48(10):7259–7273, 1993.

[35] R.H Kodama. Magnetic nanoparticles. *Journal of magnetism and magnetic materials*, 200(1):359–372, 1999.

[36] J.L. Tholence. On the frequency dependence of the transition temperature in spin glasses. *Solid state communications*, 35(2):113–117, 1980.

[37] S. Shtrikman and E.P. Wohlfarth. The theory of the Vogel-Fulcher law of spin glasses. *Physics Letters A*, 85(8):467–470, 1981.

[38] S. Shtrikman and E.P. Wohlfarth. Cooperative phenomena in spin glasses. *Journal of magnetism and magnetic materials*, 31:1421–1422, 1983.

[39] R.W. Chantrell and E.P. Wohlfarth. Dynamic and static properties of interacting fine ferromagnetic particles. *Journal of magnetism and magnetic materials*, 40(1):1–11, 1983.

[40] Geoffrey Cotin, Celine Kiefer, Francis Perton, Mauro Boero, Burak Ozdamar, Assil Bouzid, Guido Ori, Carlo Massobrio, Dominique Begin, Benoit Pichon, Damien Mertz, and Sylvie Begin-Colin. Evaluating the critical roles of precursor nature and water content when tailoring magnetic nanoparticles for specific applications. *ACS applied nano materials*, 1(8):4306–4316, 2018.

[41] Bruker corporation. Bruker diffrac.eva manual. 2021.

[42] A. L. Patterson. The scherrer formula for x-ray particle size determination. *Physical review*, 56(10):978–982, 1939.

[43] H. M. Rietveld. A profile refinement method for nuclear and magnetic structures. *Journal of Applied Crystallography*, 2(2):65–71, 1969.

[44] R. F. Egerton. *Physical principles of electron microscopy : an introduction to TEM, SEM, and AEM.* Springer, New York, NY, 1st ed. 2005. edition, 2005.

[45] Jun Yamasaki, Yuya Ubata, and Hidehiro Yasuda. Empirical determination of transmission attenuation curves in mass–thickness contrast tem imaging. *Ultramicroscopy*, 200:20–27, 2019.

[46] A. Thust. High-resolution transmission electron microscopy on an absolute contrast scale. *Physical review letters*, 102(22):220801–220801, 2009.

[47] Caroline Schneider, Wayne Rasband, and Kevin Eliceiri. Nih image to imagej: 25 years of image analysis. *Nature Methods*, 9, 07 2012.

[48] Riyad R. Irani. The interpretation of abnormalities in the log-normal distribution of particle size. *The Journal of Physical Chemistry*, 63(10):1603–1607, 1959.

[49] L B Kiss, J Söderlund, G A Niklasson, and C G Granqvist. New approach to the origin of lognormal size distributions of nanoparticles. *Nanotechnology*, 10(1):25, mar 1999.

[50] Philipp Gütlich, Eckhard Bill, and Alfred X Trautwein. *Mössbauer Spectroscopy and Transition Metal Chemistry: Fundamentals and Applications.* Springer Berlin / Heidelberg, Berlin, Heidelberg, 1 edition, 2011.

[51] Yutaka Yoshida, Guido Langouche, Guido Langouche, and Yutaka Yoshida. *Mössbauer Spectroscopy: Tutorial Book.* Springer Nature, Berlin, Heidelberg, 2013 edition. edition, 2012.

[52] Randall Black and F. Wellstood. *Measurements of Magnetism and Magnetic Properties of Matter*, volume 2, pages 391 – 440. 12 2006.

[53] M. McElfresh. Fundamentals magnetism and magnetic measurements featuring quantum designs magnetic property measurement system. *Quantum Design*, 1994.

[54] J.A. Mydosh. Spin glasses — recent experiments and systems. *Journal of magnetism and magnetic materials*, 7(1):237–248, 1978.

[55] J. L. Dormann, L. Bessais, and D. Fiorani. A dynamic study of small interacting particles: superparamagnetic model and spin-glass laws. *Journal of physics. C, Solid state physics*, 21(10):2015–2034, 1988.

[56] Artek R. Chalifour, Jonathon C. Davidson, Nicholas R. Anderson, Thomas M. Crawford, and Karen L. Livesey. Magnetic relaxation time for an ensemble of nanoparticles with randomly aligned easy axes: A simple expression. *Phys. Rev. B*, 104:094433, Sep 2021.

[57] A. P. (A. Peter) Young. *Spin glasses and random fields.* Directions in condensed matter physics vol. 12. World Scientific, Singapore, 1998.

[58] L. Lundgren, P. Svedlindh, and O. Beckman. Experimental indications for a critical relaxation time in spin-glasses. *Physical review. B, Condensed matter*, 26(7):3990–3993, 1982.

[59] J.L. Dormann, P. Gibart, C. Suran, J.L. Tholence, and C. Sella. Superparamagnetism and relaxation effects in granular Fe-Al_2O_3 thin films. *Journal of magnetism and magnetic materials*, 15-18(2):1121–1122, 1980.

[60] D.A. Balaev, S.V. Semenov, A.A. Dubrovskiy, S.S. Yakushkin, V.L. Kirillov, and O.N. Martyanov. Superparamagnetic blocking of an ensemble of magnetite nanoparticles upon interparticle interactions. *Journal of magnetism and magnetic materials*, 440:199–202, 2017.

[61] A.A. Krasikov, Yu. V. Knyazev, D.A. Balaev, D.A. Velikanov, S.V. Stolyar, Yu. L. Mikhlin, R.N. Yaroslavtsev, and R.S. Iskhakov. Interparticle magnetic interactions and magnetic field dependence of superparamagnetic blocking temperature in ferrihydrite nanoparticle powder systems. *Physica. B, Condensed matter*, 660:414901–, 2023.

[62] W. C. Nunes, L. M. Socolovsky, J. C. Denardin, F. Cebollada, A. L. Brandl, and M. Knobel. Role of magnetic interparticle coupling on the field dependence of the superparamagnetic relaxation time. *Physical review. B*, 72(21):212413.1–212413.4, 2005.

[63] M. Respaud. Magnetization process of noninteracting ferromagnetic cobalt nanoparticles in the superparamagnetic regime: Deviation from Langevin law. *Journal of applied physics*, 86(1):556–561, 1999.

[64] Kottaipalayam Somasundaram Sivaranjani, George Antilen Jacob, and Raphael Justin Joseyphus. Comprehensive law-of-approach-to-saturation for the determination of magnetic anisotropy in soft magnetic materials. *Physica Status Solidi B–Basic Solid State Physics*, 259(10), 2022.

[65] D. Fiorani, J. Tholence, and J. L. Dormann. Magnetic properties of small ferromagnetic particles (Fe-Al_2O_3 granular thin films): comparison with spin glass properties. *Journal of physics. C, Solid state physics*, 19(27):5495–5507, 1986.

[66] Paolo Allia and Paola Tiberto. Dynamic effects of dipolar interactions on the magnetic behavior of magnetite nanoparticles. *Journal of nanoparticle research: an interdisciplinary forum for nanoscale science and technology*, 13(12):7277–7293, 2011.

[67] R. Omari, J.J. Prejean, and J. Souletie. Critical measurements in the spin glass CuMn. *Journal de physique*, 44(9):1069–1083, 1983.

[68] Hafsa Khurshid, Paula Lampen-Kelley, Òscar Iglesias, Javier Alonso, Manh-Huong Phan, Cheng-Jun Sun, Marie-Louise Saboungi, and Hariharan Srikanth. Spin-glass-like freezing of inner and outer surface layers in hollow γ-Fe_2O_3 nanoparticles. *Scientific reports*, 5(1):15054–, 2015.

[69] G. F. Goya, T. S. Berquó, F. C. Fonseca, and M. P. Morales. Static and dynamic magnetic properties of spherical magnetite nanoparticles. *Journal of applied physics*, 94(5):3520–3528, 2003.

[70] C. Vázquez-Vázquez, M. A. López-Quintela, M. C. Buján-Núñez, and J. Rivas. Finite size and surface effects on the magnetic properties of cobalt ferrite nanoparticles. *Journal of nanoparticle research: an interdisciplinary forum for nanoscale science and technology*, 13(4):1663–1676, 2011.

[71] PDF-2 2020, ICDD.

[72] R.S. Hargrove and W. Kündig. Mössbauer measurements of magnetite below the Verwey transition. *Solid state communications*, 8(5):303–308, 1970.

[73] Andris Figueiroa Bakuzis, Luis César Branquinho, Leonardo Luiz e Castro, Marcos Tiago de Amaral e Eloi, and Ronei Miotto. Chain formation and aging process in biocompatible polydisperse ferrofluids: Experimental investigation and monte carlo simulations. *Advances in colloid and interface science*, 191-192:1–21, 2013.

[74] H. Maletta and W. Felsch. Insulating spin-glass system $Eu_xSr_{1-x}S$. *Physical review. B, Condensed matter*, 20(3):1245–1260, 1979.

[75] C. Nayek, K. Manna, A. A. Imam, A. Y. Alqasrawi, and I M. Obaidat. Size-dependent magnetic anisotropy of PEG coated Fe_3O_4 nanoparticles; comparing two magnetization methods. *IOP Conference Series: Materials Science and Engineering*, 305(1):012012, feb 2018.

[76] Juan A. Ramos-Guivar, A.C. Krohling, Elvis O. López, F. Jochen Litterst, and E.C. Passamani. Superspinglass behavior of maghemite nanoparticles dispersed in mesoporous silica. *Journal of magnetism and magnetic materials*, 485:142–150, 2019.

[77] Oren Ben Dor, Shira Yochelis, Israel Felner, and Yossi Paltiel. Unusual ZFC and FC magnetic behavior in thin Co multi-layered structure. *Journal of magnetism and magnetic materials*, 428:357–361, 2017.

[78] K Takahashi, I Mogi, S Awaji, and K Watanabe. Precise measurements of diamagnetic susceptibility of benzophenone and paraffin by using a magnetic levitation technique. *Journal of Physics: Conference Series*, 156(1):012020, mar 2009.

[79] M. Fittipaldi, C. Innocenti, P. Ceci, C. Sangregorio, L. Castelli, L. Sorace, and D. Gatteschi. Looking for quantum effects in magnetic nanoparticles using the

molecular nanomagnet approach. *Physical review. B, Condensed matter and materials physics*, 83(10), 2011.

[80] Miriam Colombo, Susana Carregal-Romero, Maria F Casula, Lucía Gutiérrez, María P Morales, Ingrid B Böhm, Johannes T Heverhagen, Davide Prosperi, and Wolfgang. J Parak. Biological applications of magnetic nanoparticles. *Chemical Society reviews*, 41(11):436–4334, 2012.

[81] P. Anil Kumar and K. Mandal. Effect of spatial confinement on spin-wave spectrum: Low temperature deviation from Bloch T3/2 law in Co nanoparticles. 2007.

[82] P.V. Hendriksen, S. Linderoth, and P.-A. Lindgård. Finite-size effects in the magnetic properties of ferromagnetic clusters. *Journal of magnetism and magnetic materials*, 104:1577–1579, 1992.

[83] R. M. Bozorth, Elizabeth F. Tilden, and Albert J. Williams. Anisotropy and magnetostriction of some ferrites. *Physical review*, 99(6):1788–1798, 1955.

[84] Nandang Mufti, Desi Sari, Anisa Fitri Muyasaroh, Yudyanto Yudyanto, Sunaryono Sunaryono, and Ahmad Taufiq. Analyses of magnetic properties and crystal size on Fe_3O_4 nanoparticle from local iron sand using PEG as soft template. *Journal of Physics: Conference Series*, 1595:012004, 07 2020.

[85] Chiranjib Nayek, Kaustuv Manna, Gourab Bhattacharjee, Pattukkannu Murugavel, and Ihab Obaidat. Investigating size- and temperature-dependent coercivity and saturation magnetization in PEG coated Fe_3O_4 nanoparticles. *Magnetochemistry*, 3(2):19–, 2017.

[86] Adriele Aparecida de Almeida, Fernando Fabris, Gustavo Soares da Silva, Kleber Roberto Pirota, Marcelo Knobel, and Diego Muraca. Control of anisotropy and magnetic hyperthermia effect by addition of cobalt on magnetite nanoparticles. *ACS applied materials interfaces*, 17(9):13083–13093, 2025.

[87] C. A. M. Mulder, A. J. van Duyneveldt, and J. A. Mydosh. Susceptibility of the CuMn spin-glass: Frequency and field dependences. *Physical review. B, Condensed matter*, 23(3):1384–1396, 1981.

[88] D. Fiorani, S. Viticoli, J. L. Dormann, J. L. Tholence, and A. P. Murani. Spin-glass behavior in an antiferromagnetic frustrated spinel: $ZnCr_{1.6}Ga_{0.4}O_4$. *Physical review. B, Condensed matter*, 30(5):2776–2786, 1984.

[89] Jean-Louis Tholence. Recent experiments about the spin-glass transition. *Physica A*, 126(1):157–164, 1984.

[90] B. Leclercq, C. Rigaux, A. Mycielski, and M. Menant. *Physical review. B, Condensed matter*, (10):6169–6172.

[91] Y. Zhou, C. Rigaux, A. Mycielski, M. Menant, and N. Bontemps. Dynamics of the spin-glass freezing in semimagnetic semiconductors. *Physical review. B, Condensed matter*, 40(11):8111–8114, 1989.

[92] S. Geschwind, David A. Huse, and G. E. Devlin. New approach to critical dynamic scaling in random magnets. *Physical review. B, Condensed matter*, 41(7):4854–4857, 1990.

[93] S. Geschwind, David A. Huse, and G. E. Devlin. Improved form of static scaling for the nonlinear magnetization in spin glasses. *Physical review. B, Condensed matter*, 41(4):2650–2652, 1990.

[94] K. Gunnarsson, P. Svedlindh, P. Nordblad, L. Lundgren, H. Aruga, and A. Ito. Static scaling in a short-range ising spin glass. *Physical review. B, Condensed matter*, 43(10):8199–8203, 1991.

[95] M. Sasaki, P. E. Jönsson, H. Takayama, and H. Mamiya. Aging and memory effects in superparamagnets and superspin glasses. *Physical review. B, Condensed matter and materials physics*, 71(10):104405.1–104405.9, 2005.

[96] Masatsugu Suzuki, Sharbani I. Fullem, Itsuko S. Suzuki, Lingyan Wang, and Chuan Jian Zhong. Observation of superspin-glass behavior in Fe_3O_4 nanoparticles. *Physical review. B, Condensed matter and materials physics*, 79(2), 2009.